Cooling Rate Variations Within The Group-iva Iron Meteorites.

Citation

MOREN, ARTHUR EUGENE. *Cooling Rate Variations Within The Group-Iva Iron Meteorites*. 1978, https://preserve.lehigh.edu/lehigh-scholarship/graduate-publications-theses-dissertations/theses-dissertations/cooling-rate.

INFORMATION TO USERS

This material was produced from a microfilm copy of the original document. While the most advanced technological means to photograph and reproduce this document have been used, the quality is heavily dependent upon the quality of the original submitted.

The following explanation of techniques is provided to help you understand markings or patterns which may appear on this reproduction.

1. The sign or "target" for pages apparently lacking from the document photographed is "Missing Page(s)". If it was possible to obtain the missing page(s) or section, they are spliced into the film along with adjacent pages. This may have necessitated cutting thru an image and duplicating adjacent pages to insure you complete continuity.
2. When an image on the film is obliterated with a large round black mark, it is an indication that the photographer suspected that the copy may have moved during exposure and thus cause a blurred image. You will find a good image of the page in the adjacent frame.
3. When a map, drawing or chart, etc., was part of the material being photographed the photographer followed a definite method in "sectioning" the material. It is customary to begin photoing at the upper left hand corner of a large sheet and to continue photoing from left to right in equal sections with a small overlap. If necessary, sectioning is continued again — beginning below the first row and continuing on until complete.
4. The majority of users indicate that the textual content is of greatest value, however, a somewhat higher quality reproduction could be made from "photographs" if essential to the understanding of the dissertation. Silver prints of "photographs" may be ordered at additional charge by writing the Order Department, giving the catalog number, title, author and specific pages you wish reproduced.
5. PLEASE NOTE: Some pages may have indistinct print. Filmed as received.

University Microfilms International
300 North Zeeb Road
Ann Arbor, Michigan 48106 USA
St. John's Road, Tyler's Green
High Wycombe, Bucks, England HP10 8HR

7815823

MOREN, ARTHUR EUGENE
COOLING RATE VARIATIONS WITHIN THE GROUP-IVA
IRON METEORITES.

LEHIGH UNIVERSITY, PH.D., 1978

University
Microfilms
International 300 N. ZEEB ROAD, ANN ARBOR, MI 48106

COOLING RATE VARIATIONS WITHIN THE GROUP IVA IRON METEORITES

by

Arthur E. Moren

A Dissertation
Presented to the Graduate Committee
of Lehigh University
in Candidacy for the Degree of
Doctor of Philosophy
in
Department of Physics

Lehigh University

1978

CERTIFICATE OF APPROVAL

Approved and recommended for acceptance as a dissertation in partial fulfillment of the requirements for the degree of Doctor of Philosophy.

1/30/78
(date)

Joseph I Goldstein
Professor in Charge

Accepted 1/30/78
(date)

Special Committee directing
the doctoral work of Mr. Moren

Chairman

Joseph I Goldstein

Charles B. Sclar

Robert T. Folk

ACKNOWLEDGEMENTS

Sincere appreciation is expressed to my advisor, Professor J. I. Goldstein, for his guidance and encouragement throughout the course of this research. I hope his continued efforts to get me to think like an engineer and not like a physicist bore fruit. Particular thanks go to Mr. D. Bush and Mr. A. Romig for their technical assistance and advice with the practical aspects of the experimentation.

I am particularly grateful to my parents for their continued support and encouragement throughout my academic career.

Appreciation is extended to the National Science Foundation for their financial support of this study.

TABLE OF CONTENTS

LIST OF FIGURES

LIST OF TABLES

ABSTRACT

Cooling rates have been determined for twelve group IVA iron meteorites (fine-octahedrites) using a phase growth model based on the ternary system Fe-Ni-P. The phase growth model simulates non-isothermal diffusion controlled precipitate growth, corresponding to the growth of kamacite (α-phase) in a taenite (γ-phase) matrix. It incorporates methods for determining phase growth velocity and interface concentrations that conserve the total mass in the system.

Output from the simulation is used to create a family of cooling rate curves on plots of central taenite nickel vs. taenite half width for each meteorite. In this analysis measured taenite half widths and central taenite nickel values are compared to simulated results in order to uniquely define a meteorite's cooling rate (CR).

Twelve group IVA iron meteorites were analyzed in this study: in increasing bulk Ni content,

(1) La Grange (CR 100-300°C/Myr) (2) Signal Mountain (CR 65°C/Myr) (3) Gibeon (CR 35°C/Myr) (4) Harriman (CR 10-30°C/Myr) (5) Para de Minas (CR

25°C/Myr) (6) Muonionalusta (CR 25°C/Myr) (7) Charlotte (CR 25°C/Myr) (8) Mantos Blancos (CR 4°C/Myr) (9) Hill City (CR 6°C/Myr) (10) New Westville (CR 3°C/Myr) (11) Chinautla (CR 6°C/Myr) (12) Duchesne (CR 4°C/Myr).

The results show a variation in CR across the group IVA iron meteorites with the cooling rate inversely correlated with nickel content. The variation in cooling rates (greater than a factor of 10) argues against a core model and favors a radial distribution of these meteorites in an asteroidal sized parent body with a radius of 100 - 150 km.

INTRODUCTION

Meteorites are the fragmentary remnants of extraterrestrial bodies that have broken up and then impacted with the earth. Their very existence raises numerous questions, most of which can be divided into two main categories. One incorporates the astronomical interpretation of the relationship between meteorite falls and the orbits of meteoroids and minor planets within our solar system. The other concerns itself with the physical and chemical properties of the meteorites and what can be inferred about parent body numbers, sizes and formation.[1] The research to be described falls into the latter category.

The approximately 1700 recognized meteorites are unequally divided into four broad sections depending on appearance and composition. The sections are: chondrites, achondrites, stony-irons, and irons. The iron meteorites, which are of interest here, are primarily iron-nickel alloys that are grouped by a structural and/or a chemical classification. The structural classification is based on the size of the kamacite (bcc α - phase) precipitate band width in a taenite (fcc γ - phase) matrix. The chemical classification groups iron meteorites of similar composition based on an analysis of Ni, Ga, Ge, and Ir.[2-10]

It has been proposed that iron meteorites in a given chemical group are genetically related, and that each chemical group represents a unique parent body.[11,12,13] In addition, there are different proposed processes for iron meteorite formation within the parent body. The two most widely held views of the final process are fractional crystallization during freezing, presumably in cores,[14] and metal pods or aggregates at various depths that have undergone various stages of partial melting.[15]

In determining which process probably produced the resultant meteorites detailed study of the physical and chemical properties of the meteorites is essential. Parameters having a direct bearing on a meteorite's development can indicate which process took place. Such parameters are temperature, pressure, bulk composition, minor and trace element abundances, and cooling rates.

Cooling rates are good indicators for genetic relationships among meteorites. Meteorites that formed in the core of a single parent body would have similar cooling rates. Widely varying cooling rates would imply different parent bodies or a single parent body with the meteorites having formed at various depths of burial, not in a core.

Nearly all previous attempts to determine cooling rates for the iron meteorites have involved mathematical models of the growth of kamacite (bcc α - phase) based on the binary Fe-Ni system.[13,16,17,18] The transformation followed the path $\gamma \rightarrow \alpha + \gamma$. Phase dimensions and concentration values generated through the model were compared to those measured using an electron microprobe in order to determine a unique cooling rate.

These models are restricted in that they are binary models of a multi-element system. The most influential third element is phosphorus.[13,19,20] Small amounts of P produce significant changes in the temperature range of the $\gamma \rightarrow \alpha + \gamma$ transformation.[19,21,22] Phosphorus also shifts Ni solubility limits in the α and γ phases[23] and increases the rate of Ni diffusion in both α and γ.[24]

The purpose of this research is to redetermine the cooling rates of one iron meteorite group, the chemical group IVA, by applying a model that incorporates phosphorus effects.

There are three major stages which were used in determining the cooling rates. First is the development of a numerical model based on the ternary system Fe-Ni-P. Second is the application of the model to simulate kamacite growth. Third is the experimental analysis of selected meteorites, the results of which are compared to the model simulations in order to determine a unique cooling rate for an individual meteorite.

IRON METEORITE CLASSIFICATION SCHEMES

Iron meteorites have been classified by a variety of parameters. These include such properties as structure, mineralogy, trace element content, cooling rates and others. This chapter discusses the chemical and structural classification schemes. The kamacite growth simulations which have been used to obtain meteorite cooling rates will be described along with the shortcomings of each technique. Finally, arguments for the inclusion of a third element, phosphorus, in the simulations will be presented.

2.1 CHEMICAL CLASSIFICATION

In 1951, Goldberg et al.[2] measured trace elements in 45 iron meteorites and found that the gallium levels fell roughly into three well separated regions: Region I 45-100 ppm, Region II 17-22 ppm, Region III 1.7-2.5 ppm. Later, Lovering et al.[3] in an analysis of 88 irons further resolved Region I into two distinct groups: Group I 80-100 ppm Ga, Group II 40-65 ppm Ga. In addition they quantized the irons into germanium groups corresponding to those for Ga. Since that time the most extensive and systematic work in this area has been carried out by Wasson and co-workers who have also included the element iridium.[4-10,25] To date 16 groups have been resolved with a minimum of five members constituting a group. Due to the discrete clustering of these groups, Wasson prefers to call them genetic groups. This is probably correct in that the individual group members exhibit the same chemistry and structure and probably formed in the same regions of the solar system, perhaps having the same parent body. Of the 16 total groups, four pairs constitute composite groups in that they are extensions of each other and form continuous series on log (element 1) vs. log (element 2) plots. Figure 1 shows the 12 group clusters on a plot of log Ge vs. log Ni.[26] These additional groups are distinguished by the addition of a letter to the group number, i.e. group IIA, group IIB, etc. The related, composite groups are labeled with both letters, i.e. group IIAB. Of the 16 resolved groups it is the Ga-Ge group IVA which is of interest here. This group contains 36 members, 34 being fine octahedrites.[9] The chemical parameters of the group IVA are: 7.4-9.4 wt%Ni, 1.6-2.4 ppm Ga, .09-.14 ppm Ge, and 0.4-4 ppm Ir.[11]

Figures 2-4 are log-log plots of Ga vs. Ni, Ge vs.

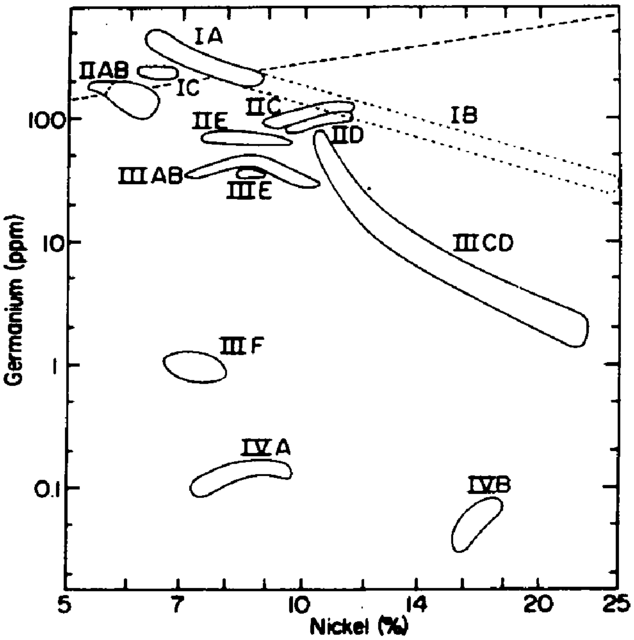

Figure 1. Logarithmic plot of Ge vs. Ni for iron meteorites.

Ni, and Ir vs. Ni for the group IVA fine octahedrites. Due to the tight trace element clusters and similar structural features it is generally held that the members of the group IVA underwent similar thermal histories in closely related environments. In addition to trace element variations, the group IVA exhibits a roughly linear relationship between log-P and log-Ni as shown in Figure 5, an important property to be discussed later. Schaudy et al.[9] had originally proposed that there might be two subgroups within the Group IVA due to the compositionla hiatus shown in Figure 4. Arguments against subgroups for the Group IVA were put forth by Scott and Wasson[26] upon an analysis of band width measurements. They also pointed out that chemical trends on one side of the gap in the log Ir vs. log Ni plot of Figure 4 match extrapolations from the other. They favor a single parent body for the group IVA. There remains the question of how the group IVA members were formed within a single parent body. It is generally accepted that a group IVA parent body was asteroidal in size[9], maximum radius several hundred km. Schaudy et al.[9] point out that there is evidence for two possible origins of the IVA's within the parent body:

1. a raisin bread model; with variable sized metal

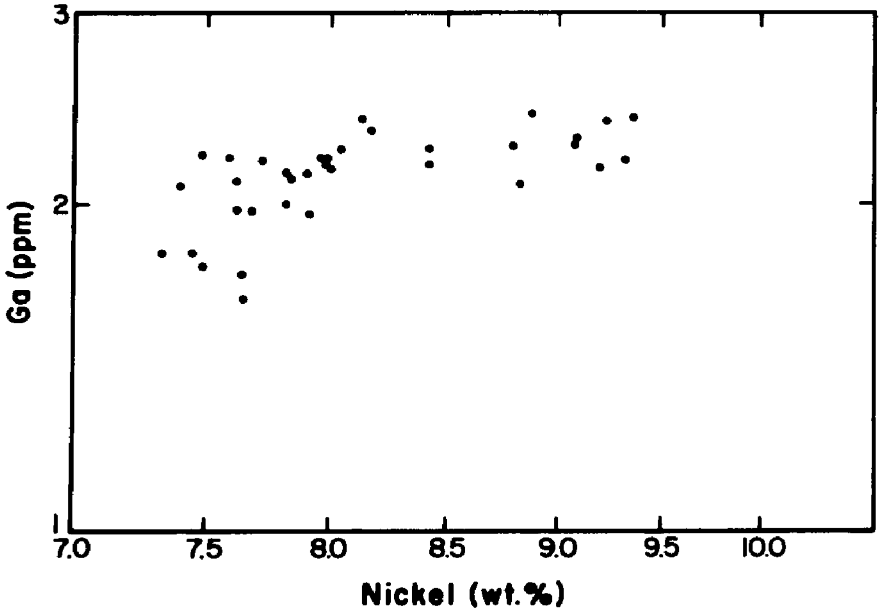

Figure 2. Logarithmic plot of Ga vs. Ni for the group IVA.

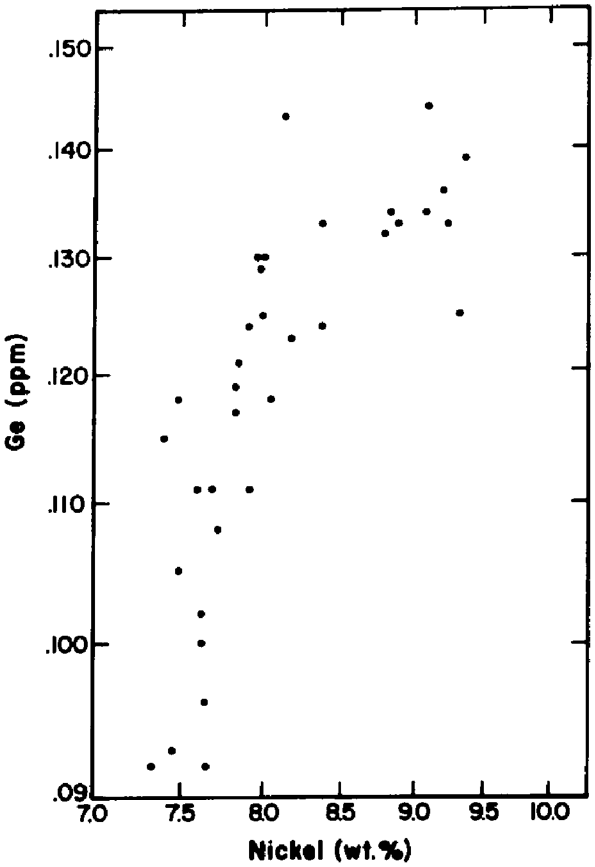

Figure 3. Logarithmic plot of Ge vs. Ni for the group IVA.

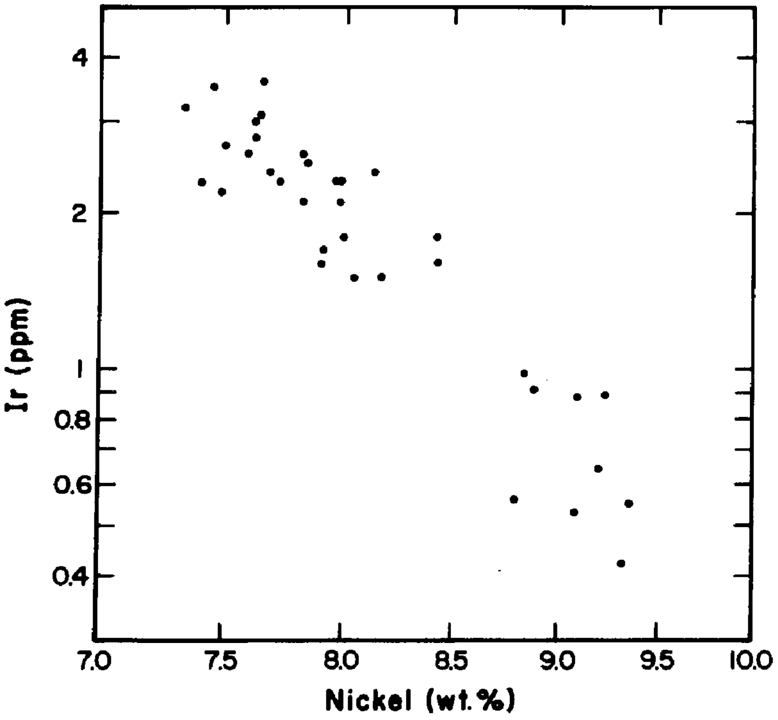

Figure 4. Logarithmic plot of Ir vs. Ni for the group IVA.

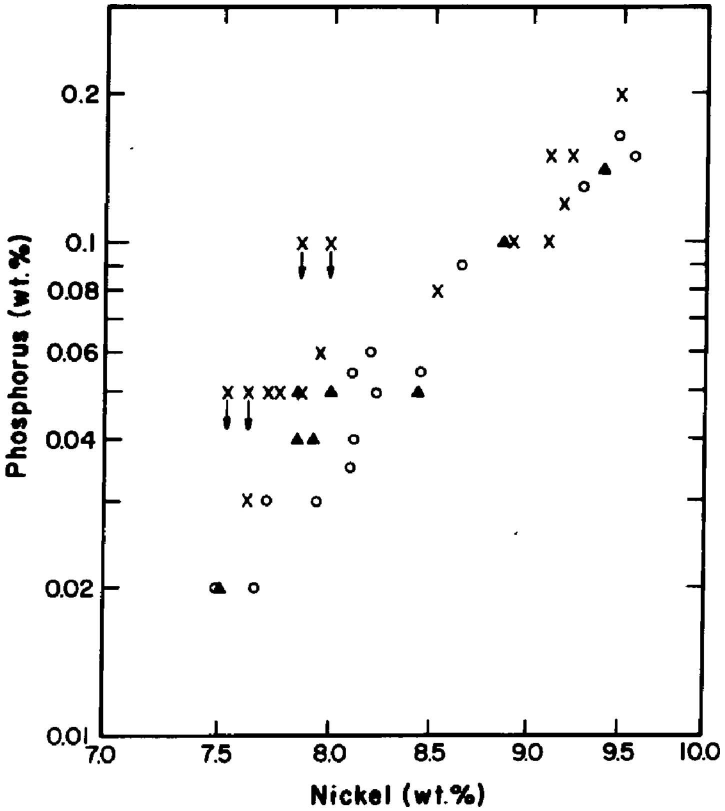

Figure 5. Logarithmic plot of P vs. Ni for the group IVA. Data is from Buchwald.[11] O represent paired Ni and P values. ▲ represent independently determined Ni and P values. X represent average Ni and P values or upper limits on P.

pods or raisins distributed throughout the asteroid

2. a core model; with the metal core being some fraction of the astroid radius.

These two possible origins will be discussed at length in a later chapter. It is a necessary condition, however, that the appropriate fractionalization model be able to produce the measured trace element distributions and the observed structural features.

The group IVA is just one of 12 independent chemical groups. The IVA members exhibit a slight variation in trace element content, and possess similar structural features. At this point there is nothing unique about the group IVA with respect to the other chemical groups.

2.2 STRUCTURAL CLASSIFICATION

The oldest classification scheme for iron meteorites is based on the structure which is visible when a polished surface is etched in an acid solution. The nucleation and growth of the kamacite (α) phase in a taenite (γ) matrix produces the octahedral or Widmanstatten structure observed in a majority of iron meteorites. The size and shape of these kamacite crystals have provided the basis for the structural classifications. There have been numerous structural schemes with various limits to kamacite band thickness.[3,11,27,28,29] The structural scheme of Buchwald,[11] Table I, closely coincides with the chemical groups proposed by Wasson[4-10,25] as seen in Table II.[11]

The fine octahedrites have kamacite bandwidths of 0.2-0.5 mm and are distributed across two chemical groups, IVA and IIIC. The vast majority of the fine octahedrites reside in the group IVA. The structural classification brings out the first unique characteristic of the group IVA fine octahedrite members. As shown in Table III,[30] which is a structural classification scheme similar to that of Table I, there is a general trend for the kamacite band width to decrease with increasing bulk nickel content. This is to be expected from growth calculations based on the Fe-Ni binary phase diagram as the $\gamma/\alpha + \gamma$ phase boundary drops to lower temperature as Ni increases. The group IVA fine octahedrites do not follow this trend. Instead they have constant to increasing kamacite band widths with increasing bulk nickel content as seen in Figure 6. This band width-Ni trend will be discussed in greater detail when growth simulations and cooling rates are presented.

TABLE I

STRUCTURAL CLASSIFICATION OF IRON METEORITES

Structural Class	Symbol	Band width, mm
Hexahedrites	H	-
Coarest Octahedrites	Ogg	>3.3
Coarse Octahedrites	Og	1.3-3.3
Medium Octahedrites	Om	0.5-1.3
Fine Octahedrites	Of	0.2-0.5
Finest Octahedrites	Off	<0.2, continuous
Plessitic Octahedrites	Opl	<0.2, spindles
Ataxites	D	

TABLE II

COMPARISON OF STRUCTURAL AND CHEMICAL CLASSES

H	IIA	Of	IVA, IIIC
Ogg	IIB	Off	IIID
Og	I, IIIE	Opl	IIC
Om	IIIA, IIIB, IID	D	IVB

TABLE III

DIVISION OF IRON METEORITES BY STRUCTURE

Structural Class	Symbol	Band width Variation,mm	Ni content, wt% Range	Median
Hexahedrites	H	>50	4.0-6.0	5.5
Hexa-octahedrites	Og-H	3-50	5.4-6.8	6.1
Coarse-octahedrites	Og	1.5-3	6.2-8.6	6.9
Medium-octahedrites	Om	0.5-1.5	7.0-12.0	8.3
Fine-octahedrites	Of	0.2-0.5	7.4-13.4	8.3
Finest-octahedrites	Off	<0.2	13.0-18.0	15.5
Ataxites	D	<0.1	10.0-30	16.3
Plessitic-octahedrites	Off-D	<0.2	9.6-18.2	10.0

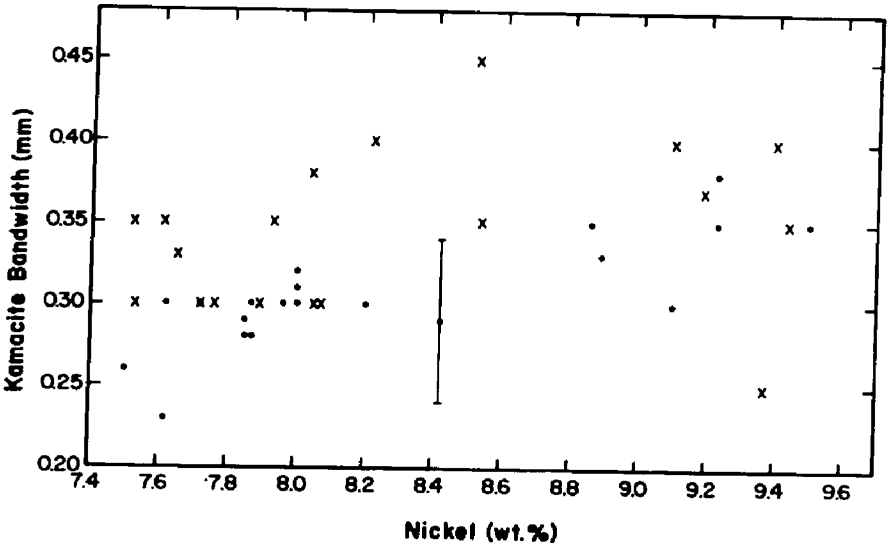

Figure 6. Kamacite band width vs. Ni for the group IVA. Bulk nickel numbers are from Buchwald.[11] ● represent band widths measured by Buchwald. X represent band widths measure by Goldstein.[28]

The fine octahedrites are basically iron-nickel alloys with minor amounts of P, Co, S, C and other trace elements.[11,30] The Widmanstatten structure is easily seen in polished and etched sections. The observed structures are basically kamacite, taenite, plessite, possibly phosphides, and troilite inclusions. Some of these features can be observed in Figures 7-8 which are photographs of polished and etched low and high nickel IVA octahedrites respectively. Kamacite, α-iron with up to approximately 7.5wt% nickel, is a bcc structure that grows preferentially along the octahedral planes of the fcc-taenite parent phase. The kamacite is fairly homogeneous except near the kamacite/taenite interface where there is nickel depletion.[30,31] The parent taenite phase usually remains as sheets or lamellae between the kamacite crystals or as borders around large plessite regions. The taenite displays marked Ni concentration gradients with the Ni content increasing as the taenite/kamacite interface is approached. Figure 9 shows a typical Ni concentration profile measured by an electron microprobe. Plessite is a mixture of fine grained kamacite and taenite. It results from a breakdown of the unequilibrated residual taenite during the late stages of primary cooling.[11,32]

Figure 7. Surface structure for the low Ni, low P group IVA meteorite Signal Mountain.

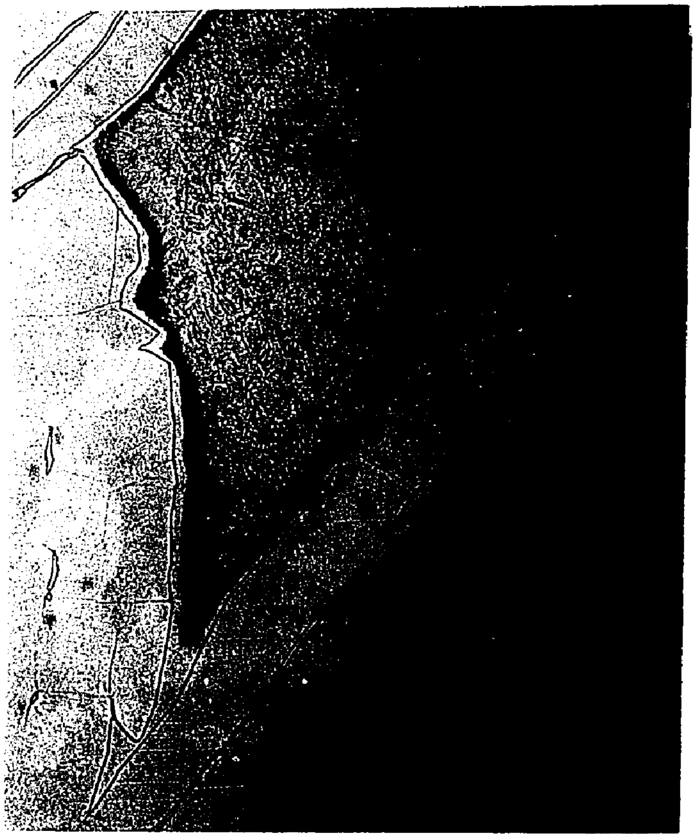

Figure 8. Surface structure for the high Ni, high P group IVA meteorite Duchesne.

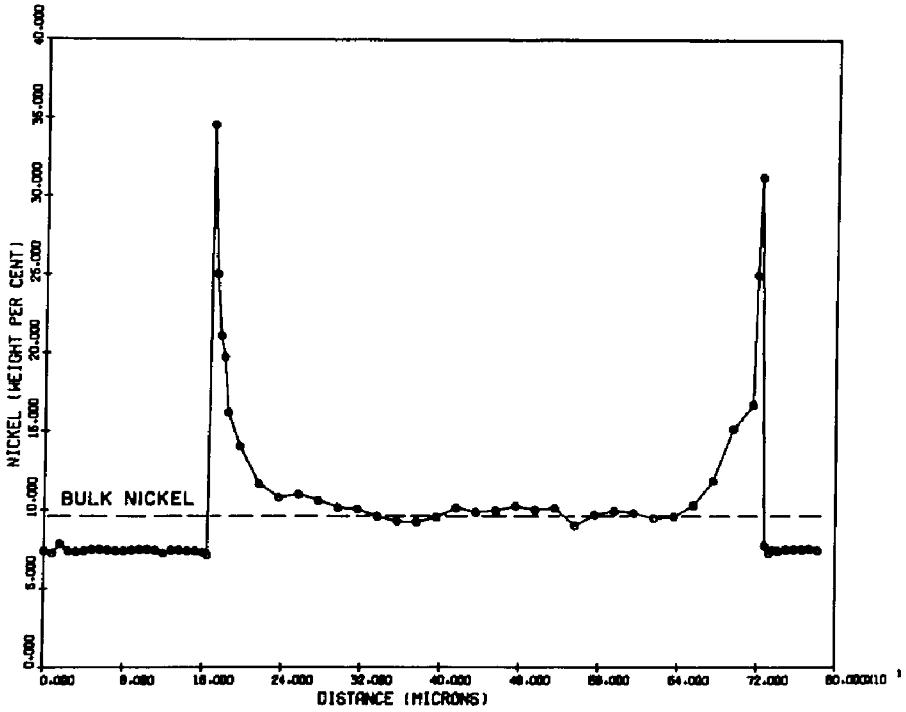

Figure 9. M-shaped Ni profile across a taenite region.

Basically the Group IVA members are fine octahedrites, displaying the Widmanstatten structure on polished and etched surfaces. The group IVA fine octahedrites, however, do not follow the usual trend of decreasing kamacite band width with increasing nickel content. The simulation of kamacite growth and cooling rate studies are the subject of the next section.

2.3 KAMACITE GROWTH SIMULATION AND COOLING RATE STUDIES

The development of the Widmanstatten structure is typically described as a non-isothermal, one-dimensional, diffusion controlled precipitate growth reaction.[16,18] Qualitative descriptions of this growth process will be found in Wood,[18,33] Goldstein and Ogilvie,[16] and more recently in Buchwald,[11] and will not be discussed here. Quantitative simulations of kamacite growth have been performed by a number of researchers in order to determine meteorite cooling rates. The salient aspects of the major methods will be described along with previous results on the IVA's.

CENTRAL TAENITE NICKEL VS. TAENITE HALFWIDTH

This method was first described by Wood[18] and applied to iron meteorites. Although his process involves the simulation of kamacite growth, Wood was only concerned with the M shaped Ni concentration profiles in the residual taenite. Wood generated a series of M shaped profiles by only varying the distance between kamacite nucleation sites. When central taenite nickel was plotted vs. log taenite half width for the series of M shaped profiles a single cooling rate curve (CRC) was generated. Wood created a family of these cooling rate curves for an individual meteorite by varying the cooling rate and/or the nucleation temperature. Using an electron microprobe Wood measured several M shaped profiles for an individual meteorite, corrected the taenite width due to band orientation and plotted the resulting central taenite nickel-log taenite half width pairs on his family of cooling rate curves. From the resultant plot he was able to determine a unique cooling rate for a given meteorite and in some cases the amount of undercooling. The most appealing feature of this method of analysis is that the nucleation temperature has very little effect on the cooling rate analysis when the taenite half widths are less than ∿10μm. Thus, undercooling was not a problem in the analysis.

Some serious deficiencies of this analysis arise from the numerical technique used: (1) at high temperatures where the greatest growth occurs the grid spacings are the coarsest. This leads to inaccuracies in measuring the total mass in the system and can cause improper shifting of the α/γ interface. (2) Diffusion of Ni in α, $\tilde{D}_\alpha$, is assumed to be ∞, when in effect it is not. (3) The addition of grid points was accomplished using linear interpolation. The original points, however, fall on a curve that is roughly in the form of an error function. Each of these features contributes to erroneous mass values in a given phase. The subsequent shift of the α/γ interface to insure mass balance was not, therefore, completely correct. In addition, various areas selected for microprobe analysis often produced asymmetrical gradients in taenite. This situation is contrary to an implicit assumption in his analysis of a closed system.

TAENITE - GRADIENT MATCHING

In this technique nickel concentration profiles measured in taenite by using an electron microprobe are matched by computer simulated profiles. Goldstein and Ogilvie[16] first used this technique to determine cooling rates, pressure effects and nucleation temperatures. In a later study, Goldstein and Short[17] performed a similar analysis but used the newer Fe-Ni binary phase diagram.[34] In addition, $\tilde{D}_\alpha$ was taken from Borg and Lai[35] and not assumed to be ∞. The effects of impingement were included. This method also requires symmetric profiles in taenite to satisfy the initial assumption of a closed system. The technique is best applied to meteorites that cooled slowly and produced flatter, more precisely measured concentration gradients. The results of this technique for the group IVA members is shown in Table IV.

KAMACITE PLATE THICKNESS

Short and Goldstein[36] generated a family of cooling rate curves on semilog plots of kamacite plate thickness vs. bulk nickel content. The simulation assumed a consistent 110°C undercooling and no impingement. Since bulk nickel contents and band widths are known for a large number of meteorites, this provided a rapid means of determining cooling rates. This method works best for iron meteorites displaying a well defined Widmanstatten structure and is more accurate than the gradient matching technique when the taenite exhibits steep concentration gradients. Goldstein and Short[37] analyzed 193 iron meteorites using this technique, 20 belonging to the group IVA. The results are shown in Figure 10. An interesting result of this study shows that certain chemical groups display little variation in cool-

TABLE IV

COOLING RATES FOR FIVE GROUP IVA IRON METEORITES-TAENITE GRADIENT MATCHING

Meteorite	Bulk Ni (wt%)	Cooling Rate (°C/million years)	Precision (%)
Huizopa	7.81	40	±25
Gibeon	7.96	20	±25
Bristol	8.3	20	±15
Altonah	8.8	20	±30
Duchesne	10.0	9	±25

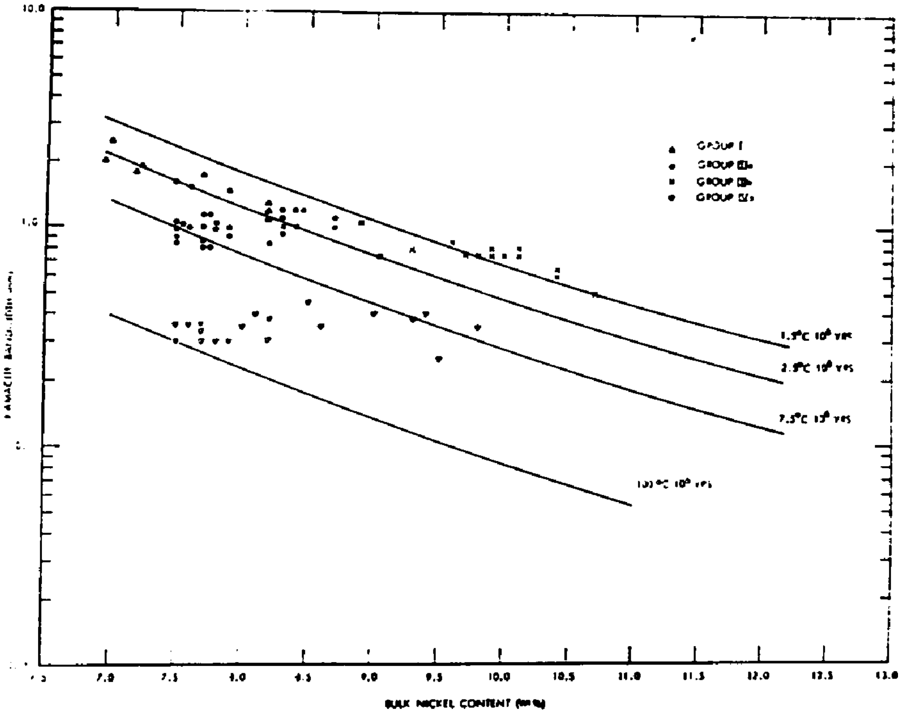

Figure 10. Variation of kamacite band width as a function of Ni content for the groups I, IIIa, IIIb, and IVa.

ing rates (see Figure 10) i.e. groups I, IIIB while other groups display a large variation in cooling rates, i.e. groups IIIA, IVA. The imperfect correlation of kamacite plate thickness with nickel content, as shown in Figures 6 and 10 for the IVA's, has been discussed by Massalski,[38] Short and Anderson,[39] and Reed.[40]. It is most likely due to cooling rate variations.

INTERFACE VALUE TECHNIQUE

In a microprobe analysis of a number of iron meteorites, Reed[40] noted that there was a definite correlation between kamacite and taenite interface Ni concentrations, and that the observed compositional trends were due primarily to cooling rate variations. He did not, however, show the numerical correspondence between interface compositions and cooling rates. Using cooling rates calculated from the gradient matching technique, Short and Goldstein[36] derived a numerical relationship between the cooling rate and the maximum Ni concentration measured in taenite at the taenite/kamacite interface using an electron microprobe. This numerical relationship is a function of the operational parameters of the microprobe and must be re-derived for each microprobe and new set of operational parameters.

KAMACITE PROFILE MATCHING

Willis[13] pointed out the possibility of verifying cooling rates by matching a measured Ni concentration profile in kamacite with a simulated profile. The initial cooling rate, however, was determined using the Wood method discussed earlier.[18] In each of the techniques described several group IVA members were analyzed. The results are compared in Table V.

It is obvious that previous methods seem to indicate a spread in the range of cooling rates for the group IVA iron meteorites. The cooling rate spread is intimately linked with the observed kamacite plate thickness variations discussed earlier. A significant range of cooling rates is the most logical explanation for the observed trend in kamacite plate thickness. A fast cooling rate for the low nickel group IVA members and a slow cooling rate for the high nickel end members will produce the observed relationship between kamacite plate thickness and bulk nickel content.

Schaudy et al.[9] suggested simultaneous nucleation as a possible explanation. This implies greater undercooling for the low nickel group IVA members and less undercooling for the high nickel members. Schaudy et al.[9] performed no simulations to substantiate this conjec-

TABLE V

PREVIOUS COOLING RATE STUDIES AND RESULTS

Meteorite	Researcher	Bulk Ni (wt%)	Cooling Rate (°C/10^6 yr.)
Yanhuitlan	GS-K*	7.5	80
Jamestown	GS-K	7.5	90
Social Circle	GS-K	7.5	70
Western Arkansas	GS-K	7.7	65
Maria Elena	GS-K	7.7	70
La Grange	GS-K	7.7	70
Huizopa	GS-K	7.8	65
	GS-G#	7.81	40
Bishop Canyon	GS-K	7.9	65
Putnam County	GS-K	7.9	60
Gibeon	GS-K	8.0	50
	GS-G	7.96	20
	Wi+	7.68	25
Charlotte	GS-K	8.1	18
Harriman	Wi	7.96	20
Para de Minas	GS-K	8.1	25
	Wi	7.99	30
Bristol	GS-K	8.2	50
	GS-G	8.3	20
	W±	8.0	10
Seneca Township	GS-K	8.5	12
Altonah	GS-K	8.6	18
	GS-G	8.8	20
Boogaldi	GS-K	9.0	10
Mantos Blancos	Wi	8.88	15
Hill City	GS-K	9.3	10
	Wi	9.09	25
New Westville	GS-K	9.4	7
	Wi	9.36	15
Duchesne	GS-K	9.5	12
	GS-G	10	9
	W	9	10
Chinautla	GS-K	9.5	8

*Goldstein and Short[37] - kamacite band width method

#Goldstein and Short[17] - taenite gradient matching

+Willis[13] - Wood method (see below)

±Wood[18] - Cooling rate curve analysis

ture. It will be shown in a later chapter that simultaneous nucleation will not produce the observed structural trend in the group IVA. No investigator who has studied or simulated kamacite growth has observed this feature of simultaneous nucleation. Short and Goldstein[36] and Goldstein and Short[37] used a consistent undercooling of ∿ 110°C in their simulations based on the more exacting profile matching technique of Goldstein and Ogilvie[16] and Goldstein and Short.[17] Wood[18] shows consistent undercooling of 80-120°C for the wide range of iron meteorites he investigated. He finds ∿ 120°C undercooling for the group IVA meteorite Bristol, bulk nickel 8.15wt%, which is in the middle of the bulk nickel spread for the group IVA.

These cooling rate determinations were in general based on simulations that utilized an Fe-Ni binary phase diagram and only binary interdiffusion coefficients $\tilde{D}_\alpha$ and $\tilde{D}_\gamma$, some simulations assuming $\tilde{D}_\alpha$ to be infinite. It is important to note here that the addition of minor elements to the system can have a marked effect upon the equilibrium phase diagram and the diffusion coefficients. Therefore, the next step is to discuss the relative importance of including minor alloying elements.

2.4 MINOR ELEMENTS

The minor elements contained in iron meteorites are phosphorus, sulphur, carbon, and cobalt. Each of these may be present in quantities up to a few percent and can cause new features in the microstructure of an iron meteorite.[30] The only element that has received serious attention in the nucleation and growth of the kamacite phase is phosphorus,[22,30,31,40,41] the other three having less drastic effects. Phosphorus will be the only minor element discussed.

An extensive investigation of phosphorus effects was carried out by Goldstein and Doan[19] based on the newly determined Fe-Ni-P phase diagram.[23] The significant features that pertain to the group IVA iron meteorites are:

1. The group IVA iron meteorites follow the reaction path $\gamma \rightarrow \alpha + \gamma$ in cooling from $\sim 700^{o}C$ to $300^{o}C$ as can be seen in Figure 11 which is a vertical section of the ternary phase diagram for a fixed 8.5wt% nickel.
2. The equilibrium nucleation temperature of kamacite with the addition of phosphorus is

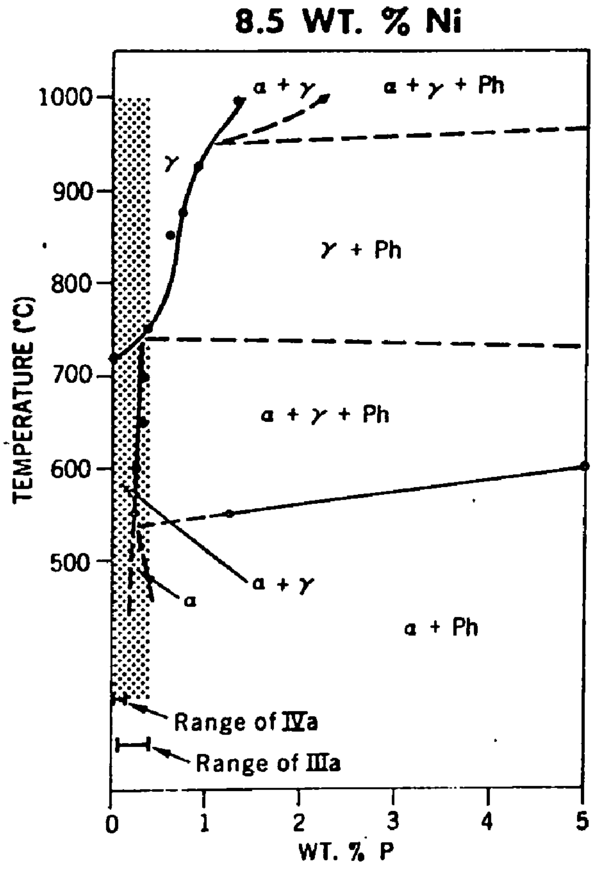

Figure 11. Vertical section of the Fe-Ni-P phase diagram at 8.5 wt.% Ni.

within ±30° of that for the binary Fe-Ni system for alloys having bulk compositions equivalent to the group IVA.

3. It still appears that undercooling of 30-100°C is necessary for the homogeneous nucleation of kamacite.
4. Over the temperature range 700°C-300°C phosphorus increases Ni solubility in α and decreases Ni solubility in γ.

In addition to shifting Ni solubilities, phosphorus produces an effect on the diffusion of nickel in both the kamacite and taenite phases. In a study on ternary diffusion Heyward and Goldstein[24] showed that the addition of P increases the major coefficients. More detail on P effects will be given in the next chapter.

2.5 SUMMARY

The group IVA iron meteorites contain 7.4-9.4wt% Ni, 1.6-2.4ppm Ga, 0.09-.14ppm Ge, 0.4-4ppm Ir, .02-.18wt% P, and are one of sixteen resolved chemical groups. The group IVA irons are predominantly fine octahedrites with kamacite band widths between 0.2-0.5mm. The band width distribution within the group goes contrary to the general trend for iron meteorites. Normally band widths decreases with increasing bulk nickel content, but the group IVA bandwidths tend to increase or remain constant with increasing nickel content. The most logical explanation for this trend is that the low nickel group IVA members cooled more rapidly than the high nickel members.

The group IVA iron meteorites contain small amounts of phosphorus. It has been shown that minor additions of phosphorus significantly change nickel solubilities in the α (increases solubility) and γ (decreases solubility) phases over the temperature range 700-300°C. Finally, phosphorus in small amounts increases the major diffusion coefficients for both nickel and phosphorus in both the α and γ phases.

In order to adequately simulate the homogeneous nucleation and growth of kamacite in taenite it is necessary to base the simulation on the ternary system Fe-Ni-P. The next chapter describes the development of this ternary model.

TERNARY MODEL FOR DIFFUSION CONTROLLED PHASE GROWTH

3.1 BACKGROUND

There are numerous analytical solutions available in the literature for the problem of diffusion controlled phase growth in binary systems.[42] Kirkaldy[43,44] and Coates[45,46] have developed analytical solutions for the problem of ternary diffusion controlled phase growth. These solutions, however, are limited to isothermal growth and are based on an assumption of an infinite matrix. The problem of overlapping diffusion fields due to neighboring precipitates, called impingement, is not treated. Since the growth of kamacite, which produces the Widmanstatten structure, is non-isothermal and involves in some cases marked impingement, a new numerical model that incorporates these effects was developed.

Ternary based numerical models that simulate diffusion controlled precipitate growth are a recent development. Most of the initial programs have been developed at Lehigh University. Isothermal growth of the γ phase in the system Fe-Ni-Co was simulated by Moren et al.[47] This simulation incorporated impingement effects. Quite good agreement was found between experiment and simulation for both the resultant precipitate size and the final tie line defining the interface concentrations.[48] Ternary modeling for non-isothermal diffusion controlled precipitate growth has also been applied to the growth of plate phosphides in hexahedrites based on the Fe-Ni-P system.[49,50]

The applicability of the modeling technique was demonstrated by Randich.[49] He experimentally heat treated a 2.1wt%P, 4.1wt%Ni, 93.8wt%Fe alloy, cooling it from 900°C to 685°C at the linear rate of 5×10^{-4} °C sec. This same process was simulated numerically. There was excellent agreement between the experimentally measured concentration profiles and the profiles resulting from the simulation.

3.2 MATHEMATICAL FORMULATION

In this section the governing differential equations will be developed and the assumptions accompanying this development will be discussed. Similar treatments have been given elsewhere.[43,44,47,50]

Diffusion in multicomponent systems may be described by the modified form of Onsager's extension of Fick's first law.[51] For a three element system where we define element 1 = phosphorus, element 2 = nickel, element 3 = iron.

(1) $$J_i = -\sum_{k=1}^{3} D'_{ik} \nabla C_k$$

where J_i is the flux of the i^{th} element, D'_{ik} is the diffusion coefficient, and C_k are the concentration values. Since the volume changes between the two phases are negligible,[16] and assuming conservation of lattice sites

(2) $$\sum_{i=1}^{3} J_i = 0$$

The units used are such that

(3) $$\sum_{i=1}^{3} C_i = \text{constant}$$

Therefore

(4) $$\sum_{i=1}^{3} \nabla C_i = 0$$

Expanding and rearranging eqn. (4) gives

(5) $$\nabla C_3 = - \nabla C_1 - \nabla C_2$$

Expanding eqn. (1), inserting eqn. (5) and combining terms gives:

(6) $$\begin{aligned} J_1 &= - (D'_{11} - D'_{13}) \nabla C_1 - (D'_{12} - D'_{13}) \nabla C_2 \\ J_2 &= - (D'_{21} - D'_{23}) \nabla C_1 - (D'_{22} - D'_{23}) \nabla C_2 \\ J_3 &= - (D'_{31} - D'_{33}) \nabla C_1 - (D'_{32} - D'_{33}) \nabla C_2 \end{aligned}$$

Letting $D_{ik} = D'_{ik} - D'_{i3}$, $k \neq 3$, eqn. (6) becomes

$$(7) \quad \begin{aligned} J_1 &= - D_{11} \nabla C_1 - D_{12} \nabla C_2 \\ J_2 &= - D_{21} \nabla C_1 - D_{22} \nabla C_2 \\ J_3 &= - D_{31} \nabla C_1 - D_{32} \nabla C_2 \end{aligned}$$

Using eqn. (2) and knowing that $\nabla C_1 \neq 0$ and $\nabla C_2 \neq 0$, it follows from eqn. (7) that

$$(8) \qquad \sum_{i=1}^{3} D_{ik} = 0$$

Therefore, writing J_3 is a redundancy. One is left with

$$(9) \qquad J_i = - \sum_{k=1}^{2} D_{ik} \nabla C_k$$

Combining eqn. (9) with the continuity equation

(10) $\quad \text{div } J_i + \frac{\partial C_i}{\partial t} = 0$, one obtains along a cartesian set of axes

$$(11) \quad \begin{aligned} \frac{\partial C_1}{\partial t} &= \nabla D_{11} \nabla C_1 + D_{11} \nabla^2 C_1 + \nabla D_{12} \nabla C_2 + D_{12} \nabla^2 C_2 \\ \frac{\partial C_2}{\partial t} &= \nabla D_{21} \nabla C_1 + D_{21} \nabla^2 C_1 + \nabla D_{22} \nabla C_2 + D_{22} \nabla^2 C_2 \end{aligned}$$

It is assumed that

(12) $$\nabla D_{ik} = 0$$

One now has

(13) $$\frac{\partial C_1}{\partial t} = D_{11}\,\nabla^2 C_1 + D_{12}\nabla^2 C_2$$
$$\frac{\partial C_2}{\partial t} = D_{21}\,\nabla^2 C_1 + D_{22}\nabla^2 C_2$$

These are the governing differential equations for diffusion controlled precipitate growth in a ternary system. To simulate a non-isothermal process that can exhibit severe impingement of diffusion fields it becomes necessary to solve equations (13) numerically. Any such numerical technique requires both space increments, Δx, and time increments, Δt. Figure 12 is a schematic of the space-composition grid for the numerical model. In this case the precipitate phase, α, is growing into the matrix phase, γ. The composition profiles are qualitative and are only for illustration. The position $x=0$, $(i=2)$, represents the center of the α precipitate. The position $x = \xi$, $(i=R)$, represents the location of the α/γ interface. The position

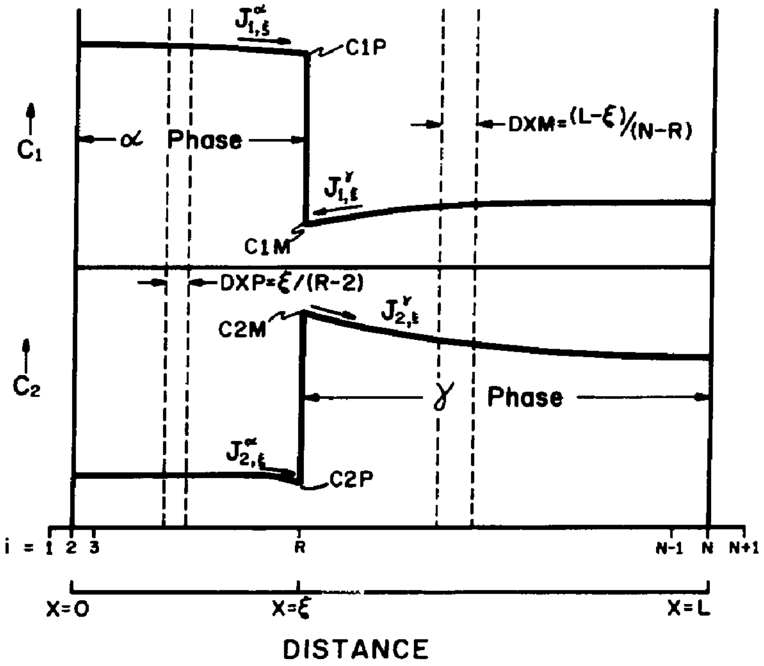

Figure 12. Schematic of the space-composition grid for the numerical model.

$x = L$, $(i=N)$, represents the center of the γ matrix. The interface compositions of elements 1 and 2 in the precipitate are designated C1P and C2P respectively. The corresponding matrix interface compositions are C1M and C2M. The precipitate and matrix grid spacings are designated DXP and DXM respectively. The points $i = 1$ and $i = N + 1$ are fictitious and are used to define the boundary conditions at $x = 0$ and $x = L$. The fluxes of element 1 evaluated at the interface, $x = \xi$, in the α precipitate and the γ matrix are $J^{\alpha}_{1,\xi}$ and $J^{\gamma}_{1,\xi}$ respectively. The corresponding fluxes for element 2 are $J^{\alpha}_{2,\xi}$, $J^{\gamma}_{2,\xi}$.

In the numerical approximation employed the interface, $x = \xi$, is always designated by the point $i = R$. Consequently as the precipitate grows the precipitate grid spacings, DXP, expand and the matrix grid spacings, DXM, contract. This expansion and contraction is a consequence of utilizing the Murray-Landis variable grid space transformation.[52,53] The transformation is used to define the time rate of change of the concentration of elements 1 and 2 at any internal position i of the space grid.

$$\frac{dC_1}{dt} = \frac{\partial C_1}{\partial x_i}\frac{dx_i}{dt} + \frac{\partial C_1}{\partial t}$$

(14)

$$\frac{dC_2}{dt} = \frac{\partial C_2}{\partial x_i}\frac{dx_i}{dt} + \frac{\partial C_2}{\partial t}$$

$\frac{\partial C_1}{\partial x_i}$ and $\frac{\partial C_2}{\partial x_i}$ are the compositional gradients of elements 1 and 2 at the internal position x_i. $\frac{dx_i}{dt}$ is the travel rate of the internal position x_i. $\frac{\partial C_1}{\partial t}$ and $\frac{\partial C_2}{\partial t}$ are the diffusion contributions given in equation (13).

Inserting eqn. (13) into eqn. (14) gives along the x-cartesian coordinate

$$\frac{dC_1}{dt} = \frac{\partial C_1}{\partial x_i}\frac{dx_i}{dt} + D_{11}\frac{\partial^2 C_1}{\partial x^2} + D_{12}\frac{\partial^2 C_2}{\partial x^2}$$

(15)

$$\frac{dC_2}{dt} = \frac{\partial C_2}{\partial x_i}\frac{dx_i}{dt} + D_{21}\frac{\partial^2 C_1}{\partial x^2} + D_{22}\frac{\partial^2 C_2}{\partial x^2}$$

It should be noted at this point that the pair of equations in (15) apply separately in each phase since obviously the D's vary according to the phase present as well as $\frac{dx_i}{dt}$ having separate forms in the precipitate (kamacite) and the matrix (taenite). The final form of the differential equation that is to be approximated numerically will only be developed for element 1 in the precipitate.

With the precipitate and matrix centers fixed, the greatest rate of internal grid point movement occurs at the interface. That is, $\frac{dx_i}{dt}$ = max at $x_i = \xi$, $\frac{dx_i}{dt} = 0$ at $x_i = 0$, $x_i = L$

The rate of movement of an internal point, $\frac{dx_i}{dt}$, is related to the rate of movement of the interface $\frac{d\xi}{dt}$.[53] In the precipitate:

$$(16) \qquad \frac{dx_i}{dt} = \frac{x_i}{\xi}\frac{d\xi}{dt}$$

In the matrix:

$$(17) \qquad \frac{dx_i}{dt} = \left(\frac{L - x_i}{L - \xi}\right)\frac{d\xi}{dt}$$

Inserting eqn. (16) into eqn. (15) gives

$$(18) \qquad \frac{dC_1}{dt} = \frac{x_i}{\xi}\frac{\partial C_1}{\partial x_i}\frac{d\xi}{dt} + D_{11}\frac{\partial^2 C_1}{\partial x^2} + D_{12}\frac{\partial^2 C_2}{\partial x^2}$$

This is the expression to be numerically approximated.

So far the major assumption in developing the governing differential equations are:

1. Ternary diffusion coefficients are not strongly

concentration dependent. $\frac{\partial D}{\partial x} = 0$.

2. The planar interface movement is normal to the interface.
3. There is local equilibrium at the interface with the concentrations specified by a unique tie line across the two phase, $\alpha + \gamma$, region.

BOUNDARY CONDITIONS

Referring to Figure 12 the boundary conditions involve the positions $x = 0$, $x = \xi$, and $x = L$. At $x = 0$ and $x = L$, $\frac{\partial C_1}{\partial x} = \frac{\partial C_2}{\partial x} = 0$. There is no mass flow across these boundaries. This particular boundary condition is satisfied by making use of the two fictitious points at $i = 1$ and $i = N + 1$ and setting

$$\begin{aligned} &C_1\ (1) = C_1\ (3) \quad \text{for } x = 0 \\ &C_2\ (1) = C_2\ (3) \\ &\qquad\qquad\qquad \text{and} \\ &C_1\ (N+1) = C_1\ (N-1) \quad \text{for } x = L \\ &C_2\ (N+1) = C_2\ (N-1) \end{aligned} \tag{19}$$

At $x = \xi$, the interface position, the concentration values for elements 1 and 2 are specified by a unique tie line across the two phase α and γ region. The tie line choice is determined through mass conservation.

There are two basic methods of determining interface concentrations through mass balance. The first technique involves mass balances at the α/γ interface for elements 1 and 2. The equations are

$$(20)\quad \begin{aligned} (C1P - C1M)\frac{d\xi_1}{dt} &= -\left[J_{1,\xi}^{\gamma} - J_{1,\xi}^{\alpha}\right] \\ (C2P - C2M)\frac{d\xi_2}{dt} &= -\left[J_{2,\xi}^{\gamma} - J_{2,\xi}^{\alpha}\right] \end{aligned}$$

where the interface concentration terms and the fluxes are shown in Figure 12. $\frac{d\xi_1}{dt}$ and $\frac{d\xi_2}{dt}$ are the rates of interface movement for elements 1 and 2 respectively. Since there is only one physical interface it must be true that

$$(21)\quad \frac{d\xi_1}{dt} = \frac{d\xi_2}{dt} = \frac{d\xi}{dt}$$

Substitution of the above into eqn.(20) yields a coupled set of equations that can be simultaneously satisfied by a unique tie line that relates the interface concentrations one to the other. The tie line satisfying the requirements of eqn. (20) is not necessarily the one through the bulk composition (the equilibrium tie line) as the system may not be in equilibrium. Shifting the tie line produces a change in the interface concentration terms and in the flux expressions at the interface. Depending upon the direction of the tie line shift, the individual growth rates calculated using eqn. (20) can either increase or decrease and can be either positive (precipitate grows) or negative (precipitate shrinks). This technique does not apply for two special cases. First, phosphorus is a much faster diffusing element than nickel.[24] Consequently the phosphorus concentration profiles are essentially flat in each phase. There are no discernible fluxes at the interface (Note Figure 12) and, therefore, calculations of $J_{1,\xi}^{\alpha}$ and $J_{1,\xi}^{\gamma}$ are meaningless. Secondly, when there are severe compositional gradients (usually involving Ni) at the interface, as occur at large undercoolings or at low temperatures, the numerical approximation for the fluxes becomes inaccurate. The system can gain or lose significant mass. To overcome these deficiencies another method of mass balance is employed.

The second method of determining interface concentrations and satisfying equation (21) involves a calculation based on total system mass conservation rather than mass conservation just at the interface. In the one dimensional formulation being used this means that the area under the curves in Figure 12 must remain constant as the precipitate grows.

The conservation of total mass links the interface concentrations of elements 1 and 2 with the position of the interface. The difference between the newly calculated interface position and the old interface position divided by the time increment, $\Delta\xi/\Delta t$, is the rate of interface movement.

The interface mass balance is used when there are fluxes present and the compositional gradients are gradual. The total system mass conservation technique is used when phosphorus has flat profiles or the compositional gradients at the interface are severe.

NUMERICAL APPROXIMATION

The Crank-Nicholson finite difference technique is used to numerically approximate the governing differential equations such as that given by equation (18). In a space-time grid (n = time step, i = space point) the expansions are carried out about the point i, n + 1/2 with the linkage shown in Figure 13. The Crank-Nicholson method has no theoretical bounds on the stability criterion ratio $D\Delta t/\Delta x^2$ where D is the diffusion coefficient, Δt is the time increment, and Δx is the space increment. Normally a restriction of $D\Delta t/\Delta x^2$

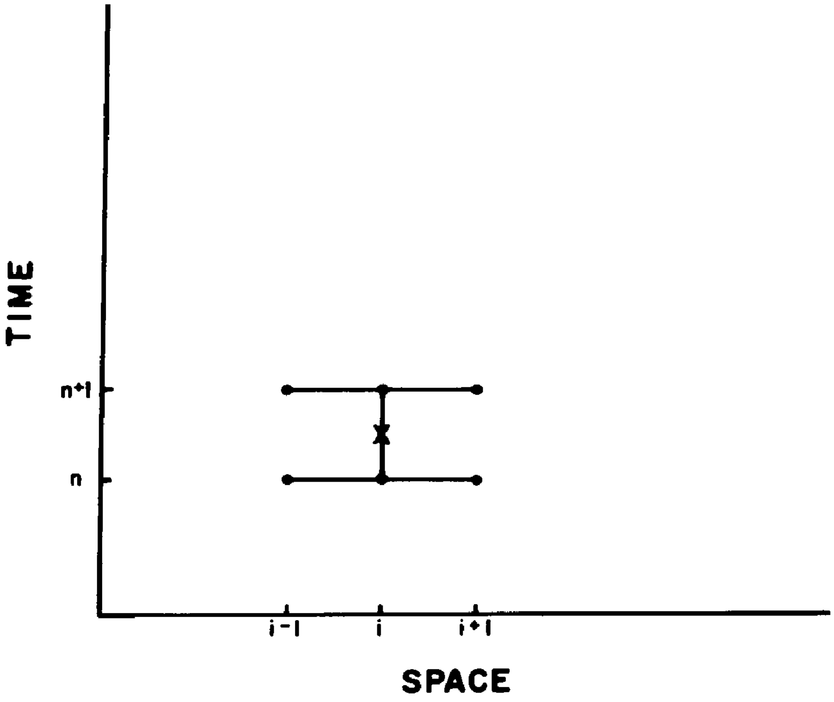

Figure 13. Linkage for the Crank-Nicholson finite difference approximation.

$\leq$ 0.5 is required for stability in the more common numerical approximation schemes (i.e. the forward finite difference technique).

In addition, the Crank-Nicholson has the added feature of being second order correct in the $\frac{\partial C}{\partial t}$ term and fourth order correct in the $\frac{\partial^2 C}{\partial x^2}$ term.

The implicit Crank-Nicholson requires more mathematical operations, but has increased accuracy and the capability of providing stable solutions for the large values of $D\Delta t/\Delta x^2$ necessary to cover the large time spans required by slow cooling.

The numerical approximations are obtained by performing Taylor expansions about appropriate points and combining pairs of expansions. The resultant numerical approximations are shown below. All of the derivatives are evaluated at time n+1/2, space point i, as shown in Figure 13.

$$(22) \qquad \left.\frac{dC}{dt}\right)_i^{n+\frac{1}{2}} \cong \frac{C_i^{n+1}-C_i^{\,n}}{\Delta t}$$

$$(23) \qquad \left.\frac{\partial C}{\partial x}\right)_i^{n+\frac{1}{2}} \cong \frac{1}{2}\left[\frac{C_{i+1}^{n+1}-C_{i-1}^{n+1}}{2\Delta x}+\frac{C_{i+1}^{n}-C_{i-1}^{\,n}}{2\Delta x}\right]$$

$$(24)\quad \left.\frac{\partial^2 C}{\partial x^2}\right)_i^{n+\frac{1}{2}} \cong \frac{1}{2}\left[\frac{C_{i-1}^{n+1} - 2C_i^{n+1} + C_{i+1}^{n+1}}{\Delta x^2} + \frac{C_{i-1}^{n} - 2C_i^{n} + C_{i+1}^{n}}{\Delta x^2}\right]$$

The subscripts refer to the spatial position and the superscripts refer to the time step. It has been assumed that Δx at time step n+1 equals Δx at time step n.

From Figure 12, in the precipitate

$$(25)\qquad x_i = (i - 2)\ \mathrm{DXP} \qquad \text{and}$$

in the matrix

$$(26)\qquad x_i = L - (N - i)\ \mathrm{DXM}$$

Working with element one in the precipitate the substitution of eqns. (22), (23), (24) and (25) into eqn. (21) becomes after shifting and collecting terms:

$$C1_{i-1}^{n+1}\left[\left(\frac{i-2}{4\xi}\right)\frac{d\xi}{dt} - \frac{\mathrm{D11P}}{2\,\mathrm{DXP}^2}\right] + C1_{i}^{n+1}$$

$$\left[\frac{1}{\Delta t} + \frac{\mathrm{D11P}}{\mathrm{DXP}^2}\right] + C1_{i+1}^{n+1}\left[-\left(\frac{i-2}{4\xi}\right)\frac{d\xi}{dt} - \frac{\mathrm{D11P}}{2\,\mathrm{DXP}^2}\right] +$$

$$C2_{i-1}^{n+1}\left[-\frac{\mathrm{D12P}}{2\,\mathrm{DXP}^2}\right] + C2_{i}^{n+1}\left[\frac{\mathrm{D12P}}{\mathrm{DXP}^2}\right] +$$

$$\begin{aligned} C_{2\,i+1}^{\,n+1} \left[- \frac{D12P}{2\,DXP^2} \right] = {} & C_{1\,i-1}^{\,n} \left[- \left(\frac{i-2}{4\xi} \right) \frac{d\xi}{dt} + \frac{D11P}{2\,DXP^2} \right] + C_{1\,i}^{\,n} \left[\frac{1}{\Delta t} - \frac{D11P}{DXP^2} \right] + C_{1\,i+1}^{\,n} \\ & \left[\left(\frac{i-2}{4\xi} \right) \frac{d\xi}{dt} + \frac{D11P}{2DXP^2} \right] + C_{2\,i-1}^{\,n} \left[+ \frac{D12P}{2\,DXP^2} \right] \\ & + C_{2\,i}^{\,n} \left[- \frac{D12P}{DXP^2} \right] + C_{2\,i+1}^{\,n+1} \left[+ \frac{D12P}{2\,DXP^2} \right] \end{aligned} \tag{27}$$

The analogous expression for element two in the precipitate as obtained by reversing the elemental subscripts on the C and D terms, i.e. $C_1 \Rightarrow C_2$, $D12P \Rightarrow D21P$ etc. In addition, there are two corresponding expressions in the matrix. The only unknown quantities in eqn. (27) and its companion expression for element two are the C's at time step n+1. These two expressions are in the form of a bi-tridiagonal matrix:

$$\begin{aligned} & a_i^{(1)} C_{1\,i-1}^{\,n+1} + a_i^{(2)} C_{2\,i-1}^{\,n+1} + b_i^{(1)} C_{1\,i}^{\,n+1} + \\ & b_i^{(2)} C_{2\,i}^{\,n+1} + c_i^{(1)} C_{1\,i+1}^{\,n+1} + c_i^{(2)} C_{2\,i+1}^{\,n+1} = d_i^{(1)} \end{aligned} \tag{28a}$$

$$\begin{aligned} & a_i^{(3)} C_{1\,i-1}^{\,n+1} + a_i^{(4)} C_{2\,i-1}^{\,n+1} + b_i^{(3)} C_{1\,i}^{\,n+1} + \\ & b_i^{(4)} C_{2\,i}^{\,n+1} + c_i^{(3)} C_{1\,i+1}^{\,n+1} + c_i^{(4)} C_{2\,i+1}^{\,n+1} = d_i^{(2)} \end{aligned} \tag{28b}$$

The coefficients a_i, b_i, c_i and d_i are defined as follows for application to the precipitate phase.

$$a_i^{(1)} = \left[\left(\frac{i-2}{4\xi}\right)\frac{d\xi}{dt} - \frac{D11P}{2\,DXP^2}\right] \qquad a_i^{(2)} = \left[-\frac{D12P}{2\,DXP^2}\right]$$

$$a_i^{(3)} = \left[-\frac{D21P}{2\,DXP^2}\right] \qquad a_i^{(4)} = \left[\left(\frac{i-2}{4\xi}\right)\frac{d\xi}{dt} - \frac{D22P}{2\,DXP^2}\right]$$

$$b_i^{(1)} = \left[\frac{1}{\Delta t} + \frac{D11P}{DXP^2}\right] \qquad b_i^{(2)} = \left[\frac{D12P}{DXP^2}\right]$$

$$b_i^{(3)} = \left[\frac{D21P}{DXP^2}\right] \qquad b_i^{(4)} = \left[\frac{1}{\Delta t} + \frac{D22P}{DXP^2}\right]$$

$$c_i^{(1)} = \left[-\left(\frac{i-2}{4\xi}\right)\frac{d\xi}{dt} - \frac{D11P}{2\,DXP^2}\right] \qquad c_i^{(2)} = \left[-\frac{D12P}{2\,DXP^2}\right]$$

$$c_i^{(3)} = \left[-\frac{D21P}{2\,DXP^2}\right] \qquad c_i^{(4)} = \left[-\left(\frac{i-2}{4\xi}\right)\frac{d\xi}{dt} - \frac{D22P}{2\,DXP^2}\right]$$

$$d_i^{(1)} = -\,a_i^{(1)}\,C_{1\,i-1}^{\,n} - a_i^{(2)}\,C_{2\,i-1}^{\,n} + \left[\frac{1}{\Delta t} - \frac{D11P}{DXP^2}\right] C_{1\,i}^{\,n}$$

$$-\,b_i^{(2)}\,C_{2\,i}^{\,n} - c_i^{(1)}\,C_{1\,i+1}^{\,n} - c_i^{(2)}\,C_{2\,i+1}^{\,n}$$

$$d_i^{(2)} = -\,a_i^{(3)}\,C_{1\,i-1}^{\,n} - a_i^{(4)}\,C_{2\,i-1}^{\,n} - b_i^{(3)}\,C_{1\,i}^{\,n}$$

$$+\left[\frac{1}{\Delta t} - \frac{D22P}{DXP^2}\right] C_{2\,i}^{\,n} - c_i^{(3)}\,C_{1\,i+1}^{\,n} - c_i^{(4)}\,C_{2\,i+1}^{\,n}$$

There is a corresponding pair of equations in the bi-tridiagonal matrix form for the γ phase. Each matrix is solved separately using a standard algorithm.[54] The algorithm is listed in Appendix I.

As seen in Appendix I a necessary condition for using this algorithm for $1 \leq i \leq R$ is that the $a_1^{(m)} = c_R^{(m)} = 0$, $1 \leq m \leq 4$, for the precipitate phase and for $R \leq i \leq N$, $a_R^{(m)} = c_N^{(m)} = 0$, $1 \leq m \leq 4$, for the matrix phase. These conditions are satisfied by applying the previously discussed boundary conditions (note Figure 12) at $x = 0$, $x = L$ where $\frac{\partial C_1}{\partial x} = \frac{\partial C_2}{\partial x} = 0$, and at $x = \xi$ where $C_1 = C1P$, $C_2 = C2P$ for the precipitate, $C_1 = C1M$, $C_2 = C2M$ for the matrix. In the case of $x = 0$, $\frac{\partial C_1}{\partial x} = \frac{\partial C_2}{\partial x} = 0$, one makes use of the imaginary point $i = 1$ and sets $C_1\big)_1^{n+1} = C_1\big)_3^{n+1}$ and $C_2\big)_1^{n+1} = C_2\big)_3^{n+1}$ whereby the $a_1^{(1,2,3,4)}$ can be set $= 0$ and the $c_1^{(1,2,3,4)}$ coefficients are modified accordingly. At $x = \xi, C_1\big)_R^{n+1} = C1P$ and $C_2\big)_R^{n+1} = C2P$. These are known quantities, determined through mass balance and the equilibrium phase diagram. They can be shifted to the right side of the equation and included in the $d_R^{(1)}$, $d_R^{(2)}$ terms. A similar technique is applied in the matrix phase.

The algorithm applied to both phases yields a new set of concentration values, $C_{1\,i}^{\;n+1}$ and $C_{2\,i}^{\;n+1}$ for the new time step n+1. In solving the algorithm for each phase the coefficients of all the $C_{1\,i}^{\,n+1}$ and $C_{2\,i}^{\,n+1}$ terms, i.e. $a_i^{(1,2,3,4)}$, $b_i^{(1,2,3,4)}$, $c_i^{(1,2,3,4)}$, as well as the $d_i^{(1,2)}$ expressions must be known quantities. Some method must have been established to obtain the diffusion coefficients and the interface concentration values for any temperature T. These quantities are fixed internal parameters. They are the same for any growth simulation problem. They are the subject of the next section.

3.3 FIXED INTERNAL PARAMETERS

PHASE DIAGRAM

In order to determine the interface concentrations, C1P, C2P for the precipitate, C1M, C2M for the matrix it is necessary to know the equilibrium phase diagram as a function of temperature. Also, a method of determining tie lines at any given temperature is essential to selecting the unique interface compositions that satisfy mass balance. First, the equilibrium phase diagram for the two phase, $\alpha + \gamma$, region of the Fe-Ni-P system is determined. Figure 14 is a qualitative $\alpha + \gamma$ two phase field that lists the nomenclature to be used. In the three letter names the first letter A or G is for the

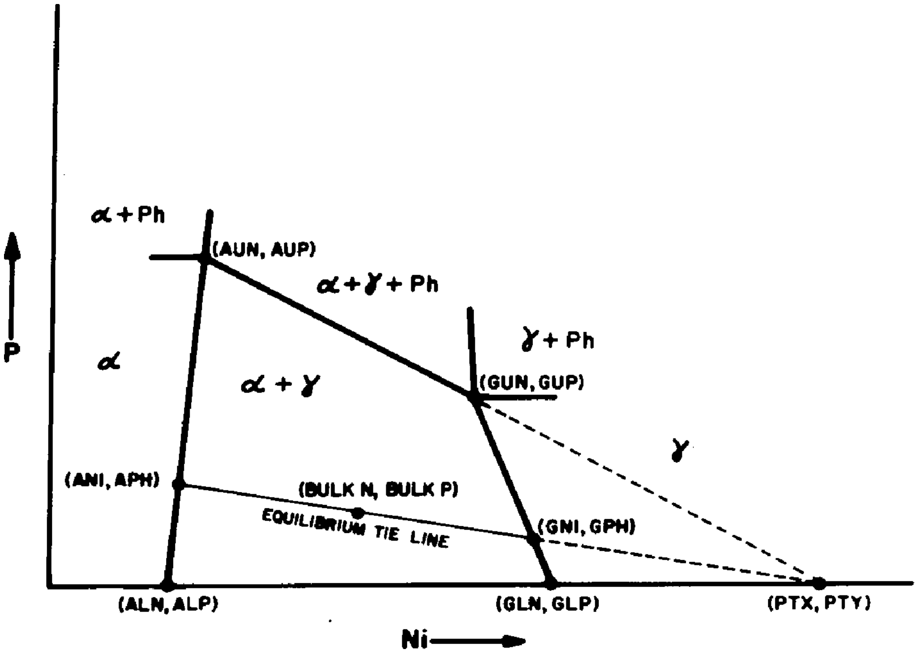

Figure 14. Qualitative α + γ two phase field in the ternary system Fe-Ni-P.

Alpha or Gamma phase, the second letter U or L is for an Upper or Lower point, and the third letter N or P is for the element Nickel or Phosphorus. The two phase field is bounded by four points forming four straight sides, none of which are parallel. ALN, ALP and GLN, GLP form the Fe-Ni binary diagram. Therefore, ALP = GLP = 0. The interior boundary points for nickel and phosphorus on the α phase side are AUN, AUP. The interior boundary points for nickel and phosphorus on the γ phase side are GUN, GUP. The bulk content of an alloy in the two phase field is designated by BULKN, BULKP as shown. The tie line across the α phase field intersects the $\alpha/\alpha+\gamma$ boundary at a point that determines a pair of α interface concentrations ANI, APH where in the course of the simulation C1P = APH, C2P = ANI. The corresponding γ phase interface concentrations are GNI, GPH where again C1M = GPH and C2M = GNI. The six non-zero concentration terms defining the two phase region must be known for any temperature from 750°C to ∿ 200°C.

ALN, AUN

The currently accepted Fe-Ni binary phase diagram over the temperature range 900-500°C is from Goldstein and Ogilvie.[34] In order to obtain an analytical expression relating the binary Ni solubility in the α-phase, ALN, to temperature the experimental data of Goldstein and Ogilvie[34] was plotted over the temperature range 750-500°C. There is a peak in the Ni solubility in α that occurs between 500-400°C with the Ni solubility decreasing below this range.[34] A trial curve, defining the α/α+γ phase boundary from 750-300°C, was drawn through the experimental data having a peak Ni solubility (< 7.5wt%) between 500-400°C. Selected data points were used in obtaining a least squares polynomial fit. A parallel procedure was used in determining the Ni solubility of the point defining the α corner of the tie triangle defining the three phase field, α + γ + Ph, namely AUN. The experimental data from Doan and Goldstein[23] was used over the temperature range 750-550°C. The presence of phosphorus increases the Ni solubility over that of the pure Fe-Ni binary. As temperature decreases the phosphorus solubility in α decreases and one would expect the Ni solubility of the point AUN to parallel that of the binary point ALN and converge on it at low temperatures. Again a trial curve was drawn through the experimental data having a Ni solubility peak (<8.0wt% Ni) between 500-400°C and converging on the binary solubility limits as temperature is decreased. Willis and Wasson[55] suggested a means of improving the Ni solubility in α curves by matching simulated Ni concentration profiles in kamacite with experimentally measured ones. The procedure to accomplish this is as follows. The completed simulation model is used to generate CR curves according to the Wood method discussed earlier and a tentative cooling rate is determined. Using phase dimensions measured from the meteorites as input to the simulation model a Ni concentration profile is generated. A corresponding Ni concentration profile in kamacite is measured on the meteorite using an electron microprobe and the two profiles are compared. The phase diagram is then modified to produce a simulated profile more closely approximating the measured one. The ALN and AUN Ni solubility curves in kamacite (α) determined using this procedure are shown in Figure 15 along with the experimental data. The simulated and measured Ni concentration profiles in kamacite are shown in Figure 16 and Figure 17 for a low and high Ni member of the Group IVA respectively. The functional relationship of ALN and AUN with temperature and the coefficient terms are given in Table VI.

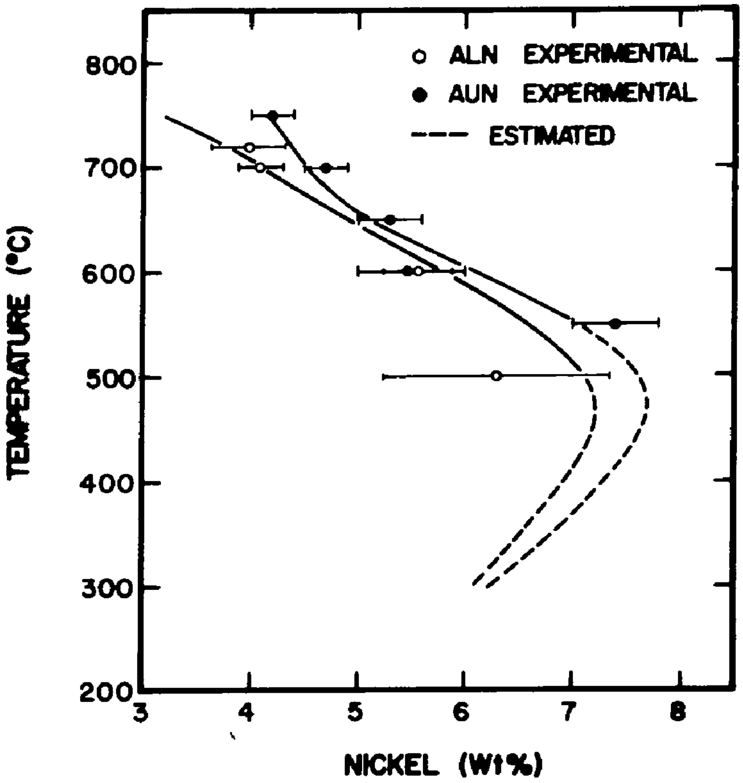

Figure 15. Nickel solubility limits for ALN and AUN, α-phase.

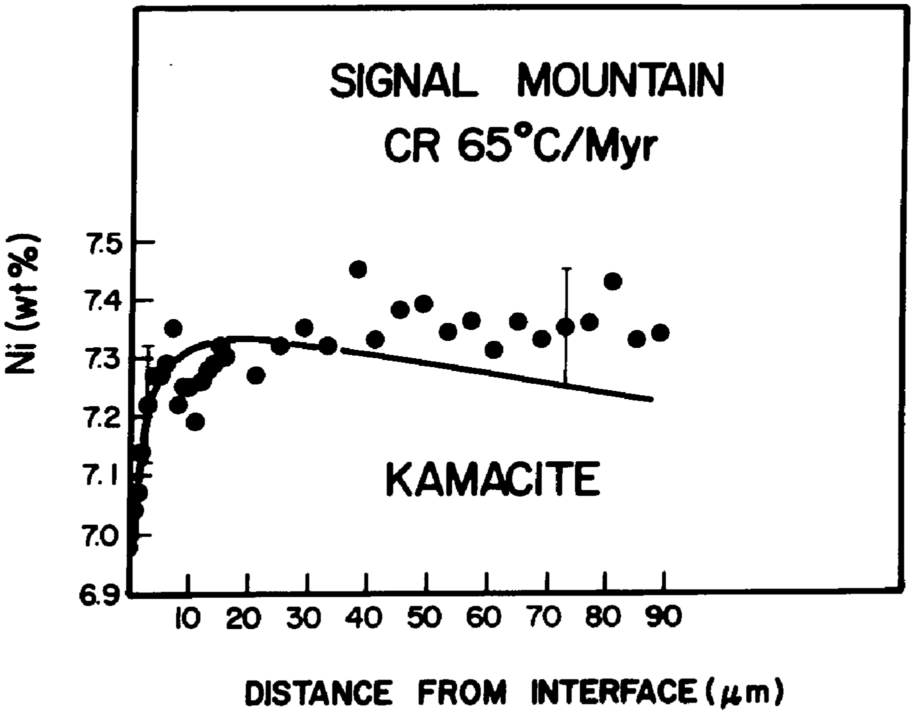

Figure 16. Measured and simulated nickel profiles in kamacite for the low nickel, low phosphorus IVA meteorite Signal Mountain.

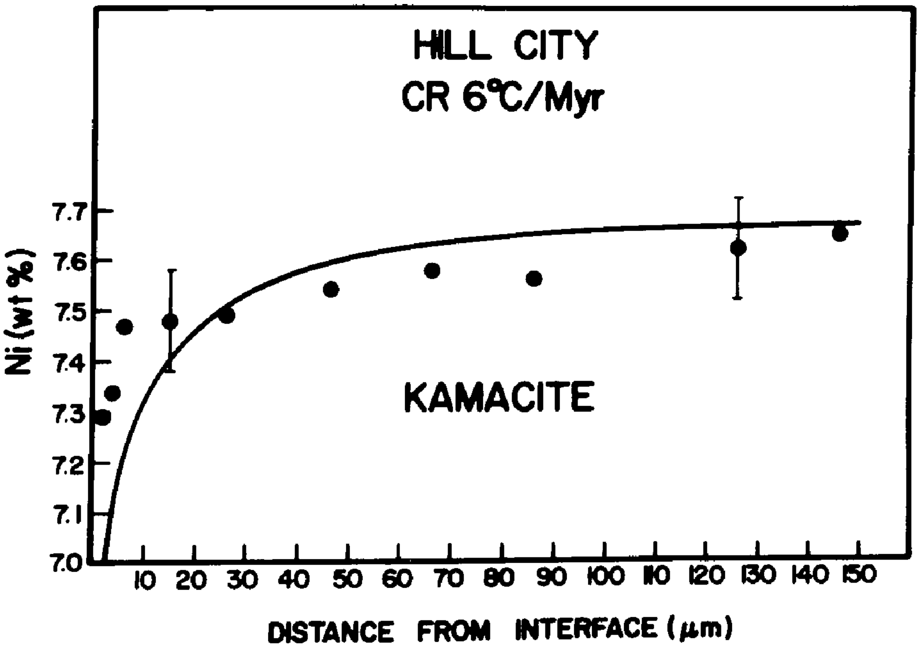

Figure 17. Measured and simulated nickel profiles in kamacite for the high nickel, high phosphorus IVA meteorite Hill City.

GLN, GUN

In order to obtain an analytical expression relating the binary Ni solubility in the γ phase, GLN, to temperature the experimental data of Goldstein and Ogilvie[34] were plotted over the temperature range 750-500°C. Extrapolations to temperatures <500°C were taken from their extended diagram.[56] A trial curve, defining the binary $\alpha+\gamma/\gamma$ phase boundary from 750-300°C, was drawn through the experimental data. Selected points were used in obtaining a least squares polynomial fit. A parallel procedure was used in determining the Ni solubility of the point defining the corner of the tie triangle defining the three phase field $\gamma + \alpha +$ Ph, namely GUN. The experimental data from Doan and Goldstein[23] was used over the temperature range 750-550°C. The presence of phosphorus decreases the Ni solubility in comparison to the Fe-Ni binary. As temperature decreases the phosphorus solubility in γ decreases (and is much less than that in α) and one would expect the Ni solubility of the point GUN to parallel that of the binary point GLN and converge on it at low temperatures. A trial curve was drawn through the experimental data paralleling the GLN curve and converging with it at $\sim$ 350°C. Again, selected points were used in obtaining a least squares polynomial fit. The GLN and GUN Ni solubility curves in taenite (γ) are shown in Figure 18 along with the experimental data. The functional relationship of GLN and GUN with temperature and the coefficient terms are given in Table VI.

AUP, GUP

The method of writing AUP and GUP as functions of temperature has been discussed by Roy S. Clarke, Jr. in his PhD. dissertation.[57] For dilute concentrations a linear relationship exists when one plots the log of phosphorus solubility vs. $1/T \times 10^4$, with temperature in K.

The experimental values for AUP are from the ternary work of Doan and Goldstein.[23] The AUP least square first order curve fit and input data are shown in Figure 19. The experimental data for GUP from Doan and Goldstein[23] was fit with a linear expression for log (GUP) vs. $1/T \times 10^4$ (K^{-1}). The experimental data and first order curve fit are shown in Figure 20. The functional relationship of AUP and GUP with temperature and the coefficient terms are given in Table VI.

The six concentration terms defining the $\alpha + \gamma$ phase field have been determined as functions of tem-

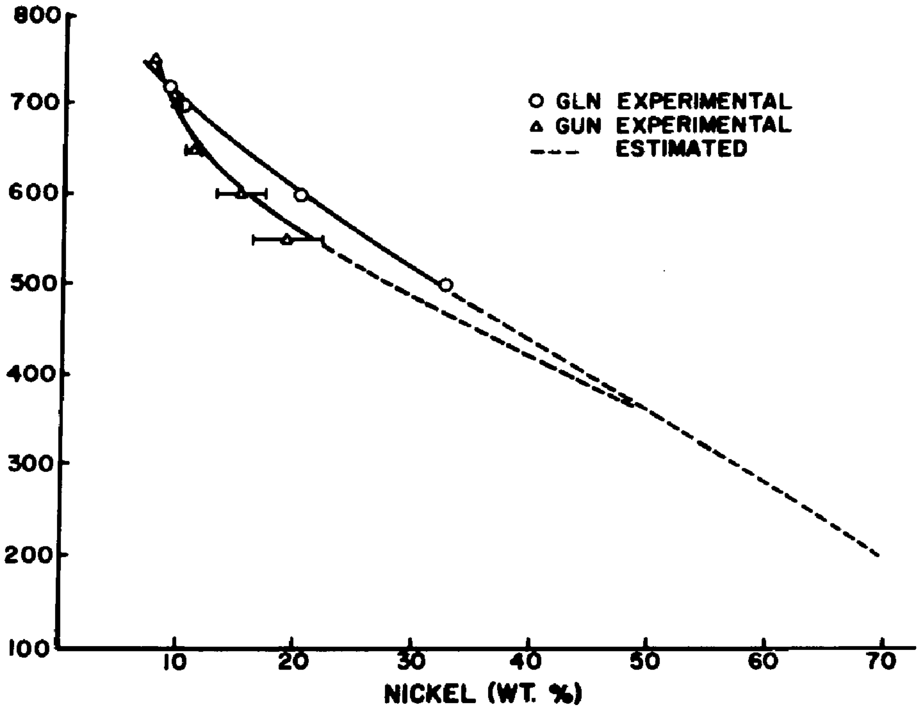

Figure 18. Nickel solubility limits for GLN, GUN, γ-phase.

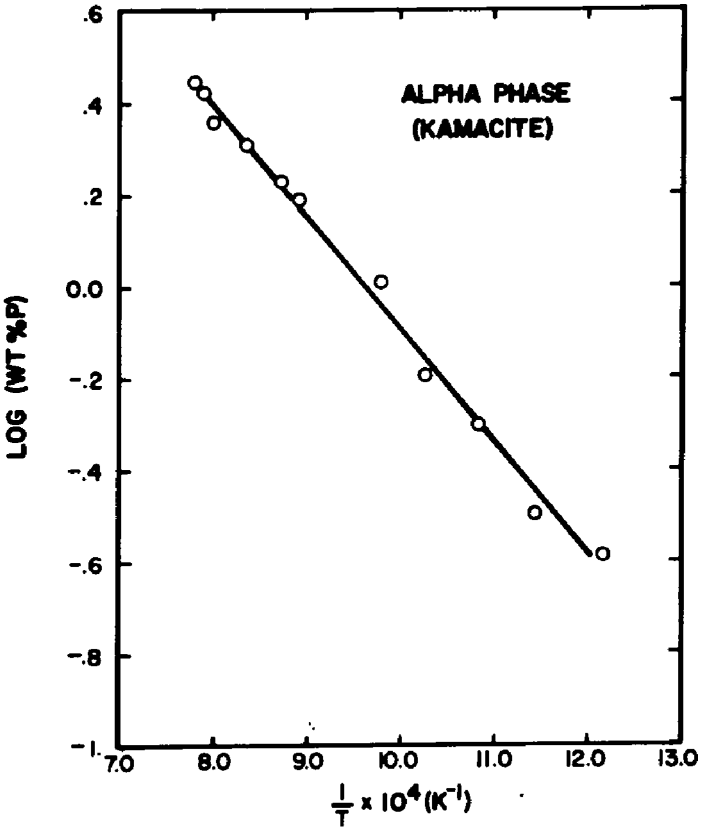

Figure 19. Phosphorus solubility limits in the α- phase, AUP.

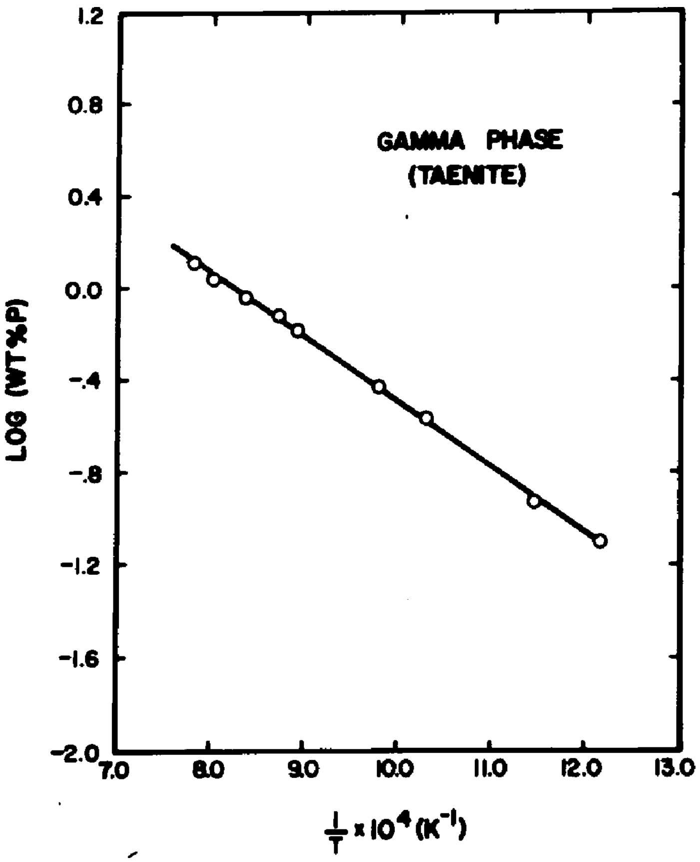

Figure 20. Phosphorus solubility limits in the γ- phase, GUP

TABLE VI

TEMPERATURE FUNCTIONALITY OF THE α+γ PHASE FIELD BOUNDARY POINTS

Type 1 $Y = A_0 + A_1X + A_2X^2 + A_3X^3 + \ldots$ $X = T$ (°C)

Type 2 $Y = 10^{(A_0 + A_1Z)}$ $Z = T$ [illegible])

The number in ( ) is the power of 10

	ALN (wt%) Type 1	AUN (wt%) Type 1	GUN (wt%) Type 1	GLN (wt%) Type 1	AUP (wt%) Type 2	GUP (wt%) Type 2
A_0	-.136348444223(03)	-.236465672048(03)	.299602015752(03)	.870008267851(02)	.234635454123(01)	.228990468176(01)
A_1	.190396491125(01)	.317351353294(01)	-.214167080045(01)	-.557387112139(-01)	-.243898491533(00)	-.278945452730(00)
A_2	-.104883184203(-01)	-.170579014544(-01)	.807823159776(-02)	-.186576410658(-03)		
A_3	.302199820440(-04)	.479563178074(-04)	-.162265826695(-04)	.156978120566(-06)		
A_4	-.476157970697(-07)	-.738603561984(-07)	.159362284383(-07)			
A_5	.387672154062(-10)	.588944400330(-10)	-.601224360572(-11)			
A_6	-.127629473134(-13)	-.190026558899(-13)				

perature. However, it is necessary to ensure that these boundary points define a valid phase diagram. Referring to Figure 21, a dashed line is drawn connecting (AUN, AUP) to (GLN, O). In order to have a valid phase diagram the point (GUN, GUP) must always be above the dashed line and to the upper right as shown by point 1. If (GUN, GUP) falls below the dashed line, point 2, it would create an invalid phase field because there now exists a range of Ni solubilities on the $\alpha/\alpha+\gamma$ boundary that can never be connected by a tie line. This region is shaded in Figure 21. According to this test the analytical expressions given in Table VI relating each of the concentration terms with temperature define a valid two phase field.

With the two phase field specified a method of defining tie lines across this region is necessary. The following technique was used. The tie lines must meet the following criteria. (Refer to Figure 14)

1. No two tie lines across the two phase region may intersect.
2. The boundary along the nickel axis between points (ALN, ALP) and (GLN, GLP) constitute a tie line.
3. The $\alpha + \gamma + PH/\alpha + \gamma$ boundary constitutes

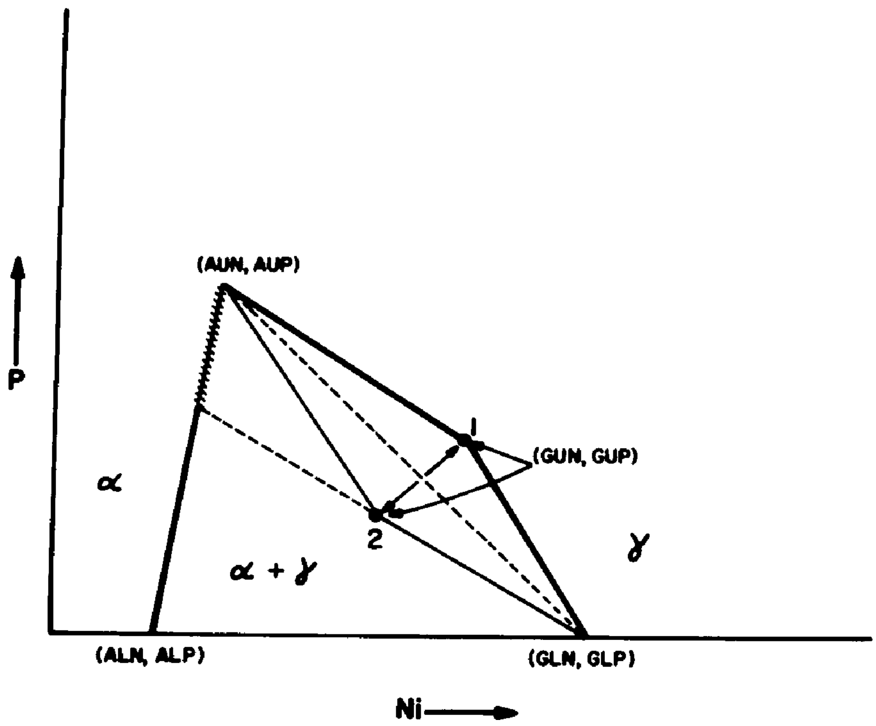

Figure 21. Schematic test for a valid two phase, α + γ, field.

another valid tie line.

The fastest and easiest method of generating possible tie lines lies in rotating a vector with origin at (PTX, O) of Figure 14 from a horizontal position (vector tip at (ALN, ALP)) through an angle such that the maximum rotation puts the vector end at (AUN, AUP). One of the infinite number of tie lines is shown in Figure 14 through the bulk composition specified by the point (BULKN, BULKP). The interface compositions for any valid tie line are specified by (ANI, APH) on the α phase side and (GNI, GPH) on the γ phase side. If the phase diagram is defined for a given temperature, three of the interface concentrations can be specified in terms of the fourth. The choice here has been to specify GPH, ANI, APH in terms of GNI except where the $\alpha + \gamma/\gamma$ boundary is vertical. A vertical boundary occurs in two regions: (Note Figure 18) 1. At a unique temperature between 720 and 730°C. 2. For T < 350°C.

The numerical model is constructed to handle the vertical $\alpha + \gamma/\gamma$ boundary situations, but the tie line analysis to be discussed only applies to a non-vertical $\alpha + \gamma/\gamma$ phase boundary. The functional relationships between the interface concentration terms will now be developed. We seek

$$\begin{aligned} \mathrm{GPH} &= \mathrm{F1\ (GNI)} \\ \mathrm{ANI} &= \mathrm{F2\ (GNI)} \\ \mathrm{APH} &= \mathrm{F3\ (GNI)} \end{aligned} \tag{29}$$

The terminology and geometry of Figure 14 will be used. Define:

$$\begin{aligned} \mathrm{SLOPE} &= \mathrm{(AUP-GUP)/(AUN-GUN)} & & \\ \mathrm{SLOPEA} &= \mathrm{(AUP-ALP)/(AUN-ALN)} & \mathrm{ALP} &= 0.0 \\ \mathrm{SLOPEG} &= \mathrm{(GUP-GLP)/(GUN-GLN)} & \mathrm{GLP} &= 0.0 \end{aligned} \tag{30}$$

Locate the point (PTX, PTY); PTY = 0.0

From Figure 14

$$\mathrm{(GUP-PTY)/(GUN-PTX)} = \mathrm{SLOPE} \tag{31}$$

rearranging

$$\mathrm{PTX} = \mathrm{GUN} - \mathrm{GUP/SLOPE} \tag{32}$$

Now determine F1 (GNI) where GPH = F1 (GNI). Again from Figure 14.

$$\mathrm{(GPH-GLP)/(GNI-GLN)} = \mathrm{SLOPEG} \tag{33}$$

$$\mathrm{GPH} = \mathrm{SLOPEG} * \mathrm{GNI} - \mathrm{SLOPEG} * \mathrm{GLN} \tag{34}$$

By constructing slopes, equating equal expressions, and performing careful algebra one can show that

$$\mathrm{ANI} = \frac{\mathrm{SLOPEA} * \mathrm{(GNI-PTX)} * \mathrm{ALN} - \mathrm{GPH} * \mathrm{PTX}}{\mathrm{SLOPEA} * \mathrm{(GNI-PTX)} - \mathrm{GPH}} \tag{35}$$

and

$$\mathrm{APH} = \mathrm{SLOPEA} * \mathrm{ANI} - \mathrm{SLOPEA} * \mathrm{ALN} \tag{36}$$

Thus, three of the interface concentrations can be written in terms of the fourth.

DIFFUSION COEFFICIENTS

In a ternary two phase system there are eight diffusion coefficients necessary for computer simulations. There are four major coefficients and four cross coefficients. The major coefficients will be treated first. The terminology used is as follows:

$D_{11}(\alpha) \equiv$ D11P : major coefficient of phosphorus in α

$D_{11}(\gamma) \equiv$ D11M : major coefficient of phosphorus in γ

$D_{22}(\alpha) \equiv$ D22P : major coefficient of nickel in α

$D_{22}(\gamma) \equiv$ D22M : major coefficient of nickel in γ

MAJOR PHOSPHORUS COEFFICIENTS

The ternary coefficient D11P is only slightly affected by the presence of Ni and varies by about 20% over a span of 1 at % P.[24] D11P increases with P. Due to the minor amounts of phosphorus in the Group IVA iron meteorites it is reasonable to define D11P as a function of temperature only, using the standard formulation, D11P = D1P*EXP (- Q/RT). Table VII shows some of the diffusion data from Heyward and Goldstein[24] and Gruzin and Minal[58] along with the concentration of the solute elements. This data is plotted in Figure 22. The ex-

TABLE VII

BINARY AND TERNARY PHOSPHORUS DIFFUSION COEFFICIENTS IN ALPHA (KAMACITE)

T	$\frac{1\text{x}10^4}{T}$	Concentrations		D11P[24]	$\tilde{D}_P(\alpha)$[58]
($^\circ$C)	(K^{-1})	P (at%)	Ni (at%)	(cm^2/sec)	(cm^2/sec)
1100	7.28	2.32	0.44	$1.31\text{x}10^{-8}$	$.309\text{x}10^{-8}$
1000	7.86	2.30	0.41	$3.27\text{x}10^{-9}$	$.962\text{x}10^{-9}$
900	8.53	2.34	0.69	$4.79\text{x}10^{-10}$	$2.5\text{x}10^{-10}$

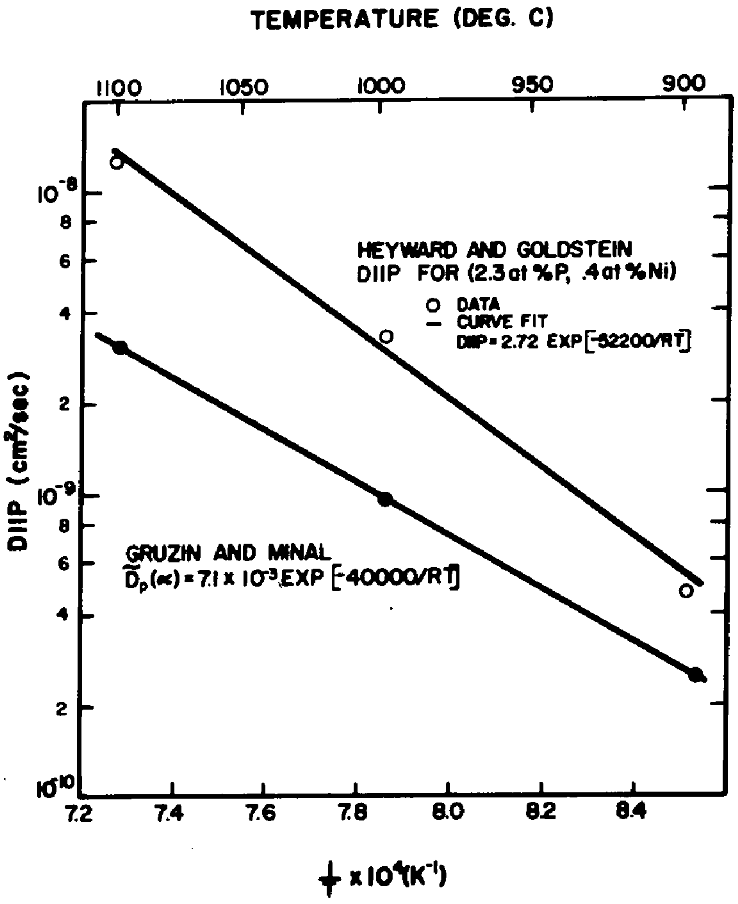

Figure 22. Temperature functionality of the major diffusion coefficient of phosphorus in the α-phase, D11P.

pression used for D11P is taken from Heyward and Goldstein.[24]

(37) $$D11P = 2.72 \ \mathrm{EXP}\ (- 52200/RT)$$

The coefficient D11M shows a slight increase with both nickel and phosphorus.[24] The increases are small enough that a temperature dependence alone is sufficient to specify D11M. Table VIII is constructed from data given by Heyward and Goldstein[24] and includes binary values from Gruzin and Minal[58] for comparison. This data is plotted in Figure 23 with selected points labeled. Heyward - Goldstein[24] curve fit points 1, 2, 3, 6 to get D11M = .51 EXP (- 55000/RT). However, if one drops point 6 and computes slopes between pairs of points as given in Table IX it is apparent points 1, 2, 3 lie nearly on the same line, and points 4 and 5 produce a closely parallel line. Disregarding data point 6 the relationship chosen for D11M is

(38) $$D11M = 9 \times 10^{-2} \ \mathrm{EXP}\ (- 50200/RT)$$

The major coefficient of nickel in the γ phase, D22M, was determined by combining binary and ternary results. The functional form for D22M is expressed as

(39) $$D22M = f1(C_p)\ f2(C_{Ni})\ f3(1/T)$$

TABLE VIII

BINARY AND TERNARY PHOSPHORUS DIFFUSION COEFFICIENTS IN GAMMA (TAENITE)

Point on Figure 23	T (^oC)	$\frac{1x10^4}{T}$ (K^{-1})	Concentrations		D11M[24] (cm^2/sec)	$\tilde{D}_P(\gamma)$[58] (cm^2/sec)
			P(wt%)	Ni(wt%)		
1	1200	6.79	.25	11.63	$3.28x10^{-9}$	$3.28x10^{-9}$
2	1100	7.28	.24	12.78	$9.4x10^{-10}$	$11x10^{-10}$
3	1000	7.86	.24	12.98	$2.21x10^{-10}$	$3.14x10^{-10}$
6	900	8.53	.24	12.35	$2.65x10^{-11}$	$7.19x10^{-11}$
4	1100	7.28	.28	4.94	$5.9x10^{-10}$	--
5	1000	7.86	.27	5.92	$1.45x10^{-10}$	--

TABLE IX

Q AND D_0 VALUES FOR POINT PAIRS ON FIGURE 23

Point Pairs	Q (Calories)	D_0 (cm^2/sec)
1-2	50276	$9.5x10^{-2}$
2-3	50218	$9.3x10^{-2}$
1-3	50249	$9.4x10^{-2}$
4-5	48740	$3.4x10^{-2}$

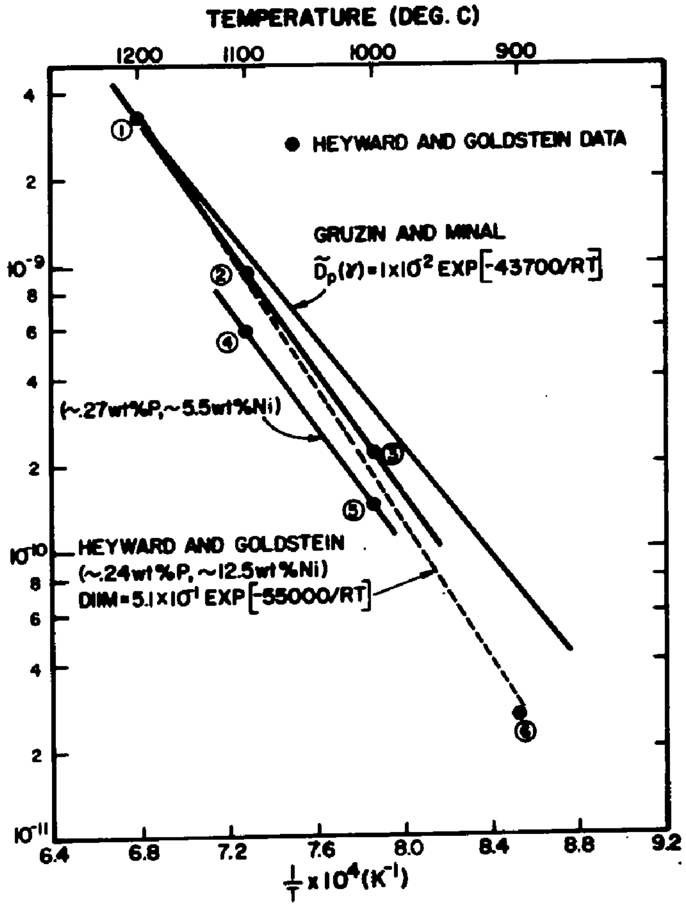

Figure 23. Temperature functionality of the major diffusion coefficient of phosphorus in the γ-phase, D22M, for various phosphorus and nickel concentrations.

For the binary case Goldstein et al.[59] determined

$$(40) \quad \tilde{D}_\gamma = \text{EXP} \quad 1.15 + 0.0519 \ (C_{Ni} \text{ at } \%) \ *$$

$$\text{EXP} \quad - \frac{(76400 - 11.6 \ (C_{Ni} \text{ at } \%))}{RT}$$

for $C_{Ni} \leq \sim 50\%$ at %. To eliminate C_{Ni} from the temperature term a value of $C_{Ni} = 20.0$wt% was used (19.21 at %) in order to more closely fit $\tilde{D}_\gamma$ to the original data. $\tilde{D}_\gamma$ is taken to be the f2 (C_{Ni}) f3 (1/T) expression, i.e. D22M = f1 (C_P) $\tilde{D}_\gamma$.

To find f1 (C_P) the ternary diffusion data from Heyward and Goldstein[24] for 1100°C was plotted and iso-diffusion contours were drawn. For selected nickel concentrations (7.0, 10.0, 15.0wt%) corresponding paired values of C_P (wt%) and D22M were picked from the iso-diffusion curves. These values are listed in Table X. In order for D22M to revert to $\tilde{D}_\gamma$ when $C_P = 0$ a fit of the form $1 + BC_P + B_1 \ C_P^2 + \ldots$ was tried.

$$(41) \qquad f1 \ (C_P) = D22M / \ f2(C_{Ni}) \ f3(1/T)$$

$$(42) \qquad 1 + BC_P + B_1 \ C_P^2 + \ldots = D22M / \ f2(C_{Ni}) \ f3(1/T)$$

$$(43) \qquad BC_P + B_1 \ C_P^2 + \ldots = (D22M / \ f2(C_{Ni}) \ f3(1/T) \ ) - 1$$

TABLE X

D22M VALUES VS. PHOSPHORUS CONCENTRATION AT 1100°C FOR FIXED NICKEL CONCENTRATIONS

Ni Concentration C_{Ni} (wt%)	P Concentration C_P (wt%)	$D22M_2 \times 10^{+12}$ (cm^2/sec)
7.0	0.0	3.33
7.0	0.247	8.2
7.0	0.485	14.0
7.0	0.696	22.5
7.0	1.043	30.8
7.0	1.098	40.4
7.0	1.173	50.0
10.0	0.0	3.87
10.0	0.114	8.2
10.0	0.340	14.0
10.0	0.554	22.5
10.0	0.900	30.8
10.0	0.952	40.4
10.0	1.032	50.0
15.0	0.0	4.97
15.0	0.042	8.2
15.0	0.253	14.0
15.0	0.471	22.5
15.0	0.817	30.8
15.0	0.869	40.4
15.0	0.948	50.0

The values of $(D22M/\ f2\ (C_{Ni})\ f3\ (1/T)\ ) - 1$ for the selected nickel concentrations of 7.0, 10.0 and 15.0wt% are listed in Table XI, and upon visual inspection were fit with a first order polynomial having the intercept forced through the point (0,0). The linear fit gave a slope of $.930039393373 \times 10^{1}$.

The entire D22M expression used is given by

$$(44) \qquad D22M = f1\ (C_P)\ f2\ (C_{Ni})\ f3\ (1/T) \quad \text{where}$$

$$f1\ (C_P) = 1.0 + (.930039393373 \times 10^{1})\ (C_P\ (wt\%))$$

$$f2\ (C_{Ni}) = EXP\left[1.15 + 0.0519\ (C_{Ni}\ (at\%))\right]$$

$$f3\ (1/T) = EXP\left[-\ 76177/RT\right]$$

The coefficient of nickel in the kamacite phase, $\tilde{D}_\alpha$, has been a subject of controversy among researchers who have simulated kamacite growth. The central issue involves the choice of binary diffusion coefficients in the α phase for the ferromagnetic region ($T<750^{\circ}C$). The diffusion coefficients of nickel in α were determined by Hirano et al.[60] and by Borg and Lai.[35] Figure 24 displays all the pertinent data from Hirano et al.[60] and Borg and Lai.[35] The temperature region covers the γ phase, α phase-paramagnetic and α phase-ferromagnetic. The data of Hirano et al.[60] was measured over the entire

TABLE XI

INTERMEDIATE VALUES USED TO DETERMINE THE FUNCTIONAL DEPENDENCE OF D22M ON PHOSPHORUS CONTENT

Ni Concentration C_{Ni} (wt%)	P Concentration C_P (wt%)	D22M/f2(C_{Ni})f3(1/T)-1
7	0.0	0.0
7	0.247	1.46
7	0.485	3.20
7	0.696	5.75
7	1.043	8.24
7	1.098	11.12
7	1.173	14.00
10	0.0	0.
10	0.114	1.12
10	0.340	2.62
10	0.554	4.81
10	0.900	6.96
10	0.952	9.44
10	1.032	11.92
15	0.0	0.0
15	0.042	0.65
15	0.253	1.82
15	0.471	3.53
15	0.817	5.20
15	0.869	7.13
15	0.943	9.07

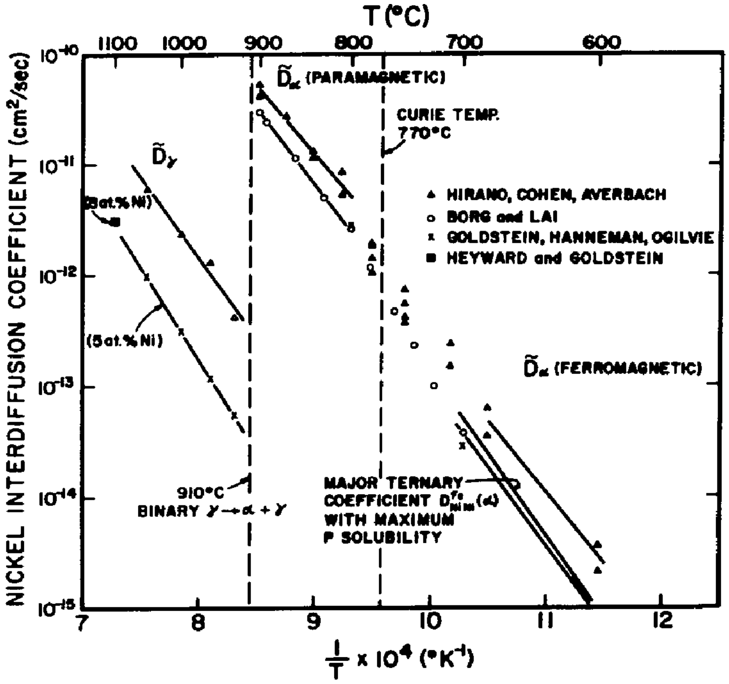

Figure 24. Temperature functionality of the major diffusion coefficients of nickel in the α and γ phases for various investigators.

temperature range while that of Borg and Lai[35] was measured over the α phase-paramagnetic with one value in the α-phase-ferromagnetic temperature range. As observed in Figure 24, the diffusion coefficients of Borg and Lai[35] are smaller than those of Hirano et al.[60] at all temperatures. Goldstein et al.[59] also determined nickel diffusion coefficients in the α phase at 800°C and 700°C. These values are shown by the X's in Figure 24. There is excellent agreement between these data and the data of Borg and Lai[35] in the α phase. Since Hirano et al.[60] and Borg and Lai[35] both agree on the magnitude of the shift in activation energy (2.7 kcal for Hirano et al.,[60] 2.4 kcal for Borg and Lai[35]) from $\tilde{D}_{\alpha}$ ferromagnetic to $\tilde{D}_{\alpha}$ paramagnetic, the lack of low temperature data by Borg and Lai[35] is not important.

It can be shown that the diffusion coefficients determined by Hirano et al.[60] are too large. The γ phase nickel diffusion coefficients from Hirano et al.[60] are significantly higher than those of Goldstein et al.[59] Ni = 5 at%), Figure 24. Heyward and Goldstein[24] have also calculated some binary coefficients and the value for 0% P, 8% Ni at 1100°C is shown in Figure 24. This value agrees with the previous binary results of Goldstein et al.[59] Clearly the diffusion coefficients determined by Hirano et al.[60] are higher than the more recent diffusion work in both the α and γ phases. Hirano et al.[60] did, however, make measurements at low temperatures, within the ferromagnetic range at 600 and 680°C where kamacite growth occurs. However, Hirano et al.[60] used the surface decrease technique for their radioactive Ni^{63} tracer work at 710°C and below. This technique was calibrated empirically with their data at 750 and 840°C obtained by another diffusion technique. Since the Hirano et al.[60] data at 750 and 840°C, as well as other temperatures in both the α and γ phase fields, lie above the Goldstein et al.[59] data, it is not surprising that the Hirano et al.[60] data within the ferromagnetic range also lie above that of Borg and Lai.[35]

The binary diffusivities of Borg and Lai[35] are the best experimental values available for calculation purposes. In the ferromagnetic range:

$$\tilde{D}_\alpha = 10.5 \text{ EXP } (-64{,}300/RT) \text{ cm}^2\text{/sec} \qquad (45)$$

where R is the gas constant (1.987 kcal/K) and T is the diffusion temperature in K.

The effect of P on $\tilde{D}_\alpha$ in the kamacite phase can

TABLE XII

INTERMEDIATE VALUES USED TO DETERMINE THE FUNCTIONAL DEPENDENCE OF D22P ON PHOSPHORUS CONTENT

P Concentration C_P (wt%)	D22Px10^9 (cm^2/sec)	D22P/$\tilde{D}_{Ni}(\alpha)$ -1
0.00	1.38	0.00
0.52	2.5	0.81
0.85	3.5	1.54
1.12	4.5	2.26
1.41	5.5	2.99
1.74	6.9	4.00
1.92	8.0	4.80

be determined using the ternary diffusion data of Heyward and Goldstein.[24] The 1100°C data of Heyward and Goldstein[24] shows that increasing the P content will increase $\tilde{D}_{\alpha}$ while increasing the Ni content will have little influence on the value of $\tilde{D}_{\alpha}$. Since the only isotherm that gives $\tilde{D}_{\alpha}$ values for various P contents is at 1100°C, it is assumed that the $\tilde{D}_{\alpha}$ dependence on P is similar at lower temperatures. From the data of Heyward and Goldstein[24] iso-diffusion contours for D22P are drawn. At a constant 5wt% nickel pairs of phosphorus concentration and diffusion coefficient values are determined. These are shown in Table XII.

The functional dependence of D22P on C_P is assumed to be of the form

$$1 + A_1 C_P + A_2 C_P^2 + \ldots \tag{46}$$

$$D22P = 1 + A_1 C_P + A_2 C_P^2 + \ldots \quad \tilde{D}_{\alpha} \tag{47}$$

$$A_1 C_P + A_2 C_P^2 + \ldots = D22P/\tilde{D}_{\alpha} - 1.0 \tag{48}$$

The expression on the right side was fit using a second order least squares polynomial. This data is listed in Table XII.

The final functional form for D22P is

$$(49)\ D22P = \left[1 + A_1\ C_P + A_2\ C_P^2\right]\left[D_o\ EXP\ (-Q/RT)\right] \text{ where}$$

$A_1 = .126654069436 \times 10^1$

$A_2 = .623119052731 \times 10^0$

$D_o = 10.5$

$Q = 64300.$

CROSS COEFFICIENTS

According to the analysis of Heyward and Goldstein[24] the cross coefficients D12P, D12M, D21P, D21M are very small in comparison to the major coefficients. D12P is $\leq$ 5% of the major coefficient D11P and D12M is $\leq$ 0.25% of the major coefficient D11M.

D21P and D21M are smaller than the experimental error and could not be measured. The cross coefficients, being negligible, were set equal to zero.

SUMMARY

The numerical model has been developed using the Crank-Nicholson finite difference technique. It incorporates the Murray-Landis variable grid space transformation.[52,53] The $\alpha + \gamma$ phase diagram has been defined and a means of generating tie lines across this region has been developed. The major coefficients for nickel and phosphorus diffusion in both the α and γ phases have been determined. The next step is to apply this model to the Group IVA iron meteorites.

APPLICATION TO THE GROUP IVA IRON METEORITES

This chapter covers three broad topics:

1. Reasons for simulating kamacite growth for the group IVA iron meteorites.
2. A sample simulation for the group IVA including input parameters, program flow charting, and profile development.
3. Application of the model and the influence of input parameters on the simulation output.

4.1 CHOICE OF THE GROUP IVA

There are two overriding reasons for applying the simulations to the group IVA iron meteorites. First: although the group IVA's contain phosphorus which affects nucleation temperatures, nickel solubilities and diffusion coefficients, the amount of phosphorus present is small enough to allow the phase transition to follow the path $\gamma \rightarrow \alpha + \gamma \rightarrow \alpha + \gamma + \text{Ph}$ (Phosphide). The majority of the precipitate growth occurs with the bulk composition in the two phase $\alpha + \gamma$ region. Hence, any simulation will parallel the earlier binary models and yet include the third element effects. At some point during the simulation the phase transition $\alpha + \gamma \rightarrow \alpha + \gamma + Ph$ occurs and the nucleation and growth of a phosphide should take place. This model is not designed to simulate the growth of both kamacite and phosphide in a γ matrix. The following procedure is used when the system has entered the three phase field. For the IVA iron meteorites the $\alpha + \gamma \rightarrow \alpha + \gamma + Ph$ transition occurs at relatively low temperatures. Due to the low phosphorus content, phosphides are not widely found in this chemical group. The simulation, therefore, continues to conserve Ni mass and uses the $\alpha + \gamma$, $\alpha + \gamma + Ph$ boundary as the applicable tie line defining the interface concentrations. Tie line shifting ceases at this point. With Ni conserved in this fashion phosphorus begins to lose mass, ostensibly to a nucleating phosphide. Because there is no means of controlling the phosphorus mass flow once the transition $\alpha + \gamma \rightarrow \alpha + \gamma + Ph$ has occurred the definitive nature of this simulation model is based solely on the resultant Ni concentration profile. Second: previous binary modeling has produced conflicting results in cooling rate variations within the group IVA iron meteorites. A majority of the results, however, indicate a significant cooling rate variation. (See Table V) In addition, the models developed to explain elemental distributions for the group IVA also conflict in the range of cooling rates necessary to produce the observed elemental distribution patterns. The implications of these models will be discussed in more detail in a later chapter.

4.2 SIMULATION FOR THE GROUP IVA

The computer simulation of kamacite growth based on the previously described numerical approximation is programmed in Fortran and designed to run on the CDC 6400 computer system at Lehigh University. Detailed program listings, input formats and operational procedures in using the simulation program are on file in the Department of Metallurgy and Materials Engineering, Lehigh University, and will not be presented here. The variable input parameters necessary to perform a simulation for a given meteorite will now be described.

The input parameters for a growth simulation include: (1) The bulk nickel and bulk phosphorus contents for a given meteorite in wt% (BULKN, BULKP of Figure 14). (2) A nucleation temperature in ^{o}C. (3) A cooling rate in ^{o}C/Myr. (4) A nucleus size in cm (E). (5) A field length in cm (L). (6) The number of precipitate grid points (R). (7) The total number of grid points (N). The parameters E, L, R, and N are shown in Figure 12. For nearly all simulations involving the group IVA the values of E, R, and N are fixed quantities. In generating output information for a specific meteorite, i.e. kamacite growth simulations, the parameters that are varied are the cooling rate, the field length, and perhaps the nucleation temperature. From meteorite to meteorite the bulk nickel and bulk phosphorus contents also change.

The sequential steps in performing a simulation are shown in Figure 25 which is a broad generalization of the computer program in a flowchart format. The variable input parameters are read in on cards. All indicators, counters, and initial conditions are set. In order to start a simulation it is necessary to establish initial profiles for phosphorus and nickel. The initial profiles should conform to the following criteria:

1. Both the initial profiles should conserve the original mass of the system, BULKP * L for phosphorus, and BULKN * L for nickel.
2. The interface concentrations should be de-

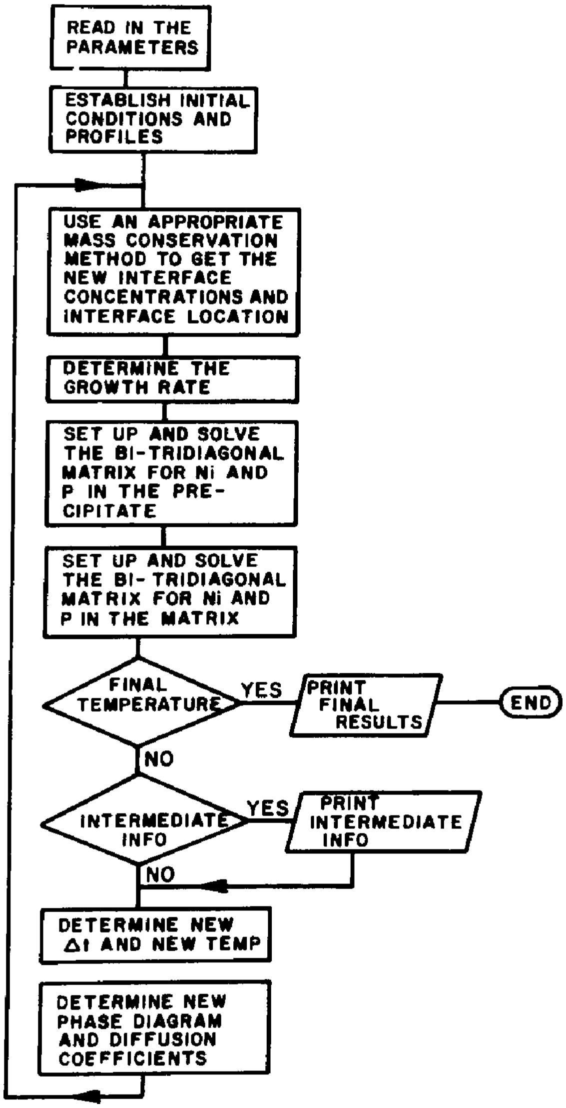

Figure 25. Flow chart schematic of the simulation model.

fined by a tie line across the α + γ phase field.

3. The initial nucleus size should be small for all nucleation temperatures since at no point is this particular system in total equilibrium.
4. The initial profiles should be established so that the numerical approximation technique is capable of handling a wide range of undercooling values.

To meet these requirements the initial profiles are established in the following manner. (Refer to Figure 14) For an individual simulation the total masses to be conserved are known, as given in No. 1 above. The initial nucleus size is assigned, normally 0.1 μm. It is reasonable to expect the phosphorus and nickel concentration profiles to be flat in the nucleating precipitate due to its small size. In addition, the time step, Δt, is set up so that the faster diffusing element, phosphorus, has enough time per time step to equilibrate in the γ matrix, i.e. the phosphorus profile is flat in both the α and γ phases. A short subroutine in the simulation model determines the appropriate and unique tie line across the α and γ region so that the phosphorus profiles are flat and the total initial phosphorus mass is conserved. This tie line also defines the nickel interface concentrations, ANI and GNI. The nickel concentration profile in α is flat, at the ANI level. The nickel interface concentration value on the γ side is GNI. The remainder of the matrix grid points are assigned the bulk nickel value, BULKN. Nickel diffuses so much slower than phosphorus that the large Δt value assigned to force a flat phosphorus profile in γ is not sufficient to cause appreciable nickel diffusion in the γ phase. Although nickel mass conservation is not a criteria for selecting the initial tie line, nickel mass is closely conserved. The maximum deviation from total nickel mass conservation occurs for high Ni, high P group IVA members with very large undercooling values. The maximum mass change is $\sim$ 1.2% under the worst circumstances.

As discussed in the mathematical development section there are two general techniques that can be used to conserve system mass. First, flux balances at the matrix-precipitate interfaces. Second, total system mass conservation through a conservation of the total areas under the profiles. The simulation model relies primarily on the second technique for two reasons: 1. The phosphorus profiles in both α and γ are flat due to the initial time increment selected. 2. Steep nickel gradients in γ at low temperatures cause unnecessary mass errors through the numerical approximation of the nickel gradient at the α/γ interface.

Two different mathematical expressions are used to calculate the area under the concentration curve depending on whether the profile in a phase is flat or has gradients.

The decision that a phosphorus or nickel profile in a given phase is flat is based on an evaluation of the stability ratio, $\frac{D\Delta t}{\Delta x^2}$, for that element. The value of the ratio $\frac{D\Delta t}{\Delta x^2}$ is related to an expression for the diffusion distance over a time period, t, namely, $x \sim \sqrt{Dt}$. Logically, if the diffusion distance, x, is larger than the respective phase dimensions then the profile will be flat.

Once the proper area conservation technique is determined it is used to calculate the new interface concentrations and the new interface position. Knowing the old and new interface position and the time increment, Δt, the interface growth rate is calculated.

The coefficients for all the bi-tridiagonal matrix elements are established and the new concentration values are determined by solving the bi-tridiagonal matrices using the algorithm listed in Appendix I. If this newly generated profile is at the lowest temperature desired the program operation is terminated and the final profile information is printed. At selected points during a simulation the current profiles are printed out. After several safety checks a new Δt is established that may be a maximum of 10% higher than the previous Δt value. Once Δt is established the new, lower, temperature is calculated. The phase diagram and the diffusion coefficients are redetermined from the new temperature and concentration profiles. The program then loops back to the procedures for determining the proper mass balance technique and the entire sequence is repeated. Normal termination of the simulation occurs when the final temperature is reached.

At certain points during a simulation complete information on the current concentration profiles is printed out. This enables one to closely follow the systematic growth of the α precipitate. Figure 26 a-e shows P and Ni concentration profiles and the corresponding isotherms for three temperatures during a kamacite growth simulation. This simulation is for a meteorite having bulk Ni 7.84wt%, bulk P 0.04wt%, cooling rate 65°C/Myr, initial nucleus size .1 μm, field length 400 μm, and a nucleation temperature of 731°C (no undercooling). After a temperature decrease of -15°C the α/γ interface has moved 63 μm. Since the temperature is still high and the precipitate small, both P and Ni have flat profile in kamacite. Phosphorus being a faster diffusing element also has a flat profile in taenite while nickel exhibits a slight gradient. Because the system is not in equilibrium, the tie line designating the interface concentrations does not go through the bulk composition. This is shown by the tie line at 715°C in Figure 26a where the solid circle represents the bulk composition. After ∿ 130°C of cooling (T = 600°C) the interface has moved 330 μ or approximately 87% of the total growth distance. For any simulation, the vast majority of the precipitate growth occurs in the first 150°C of cooling. At T = 600°C the phosphorus profile is still flat in both kamacite and taenite. The level of phosphorus in each phase has decreased as seen in Figures 26 b, d and shown by the 600°C tie line in Figure 26a. Nickel diffusion is

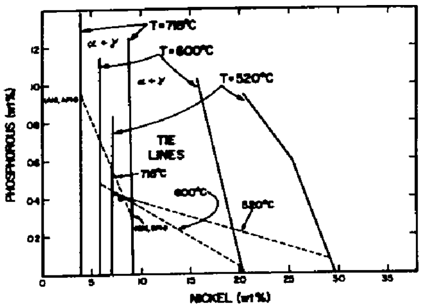

Figure 26. (a) α + γ phase field and interface tie lines for three temperatures during a simulation.

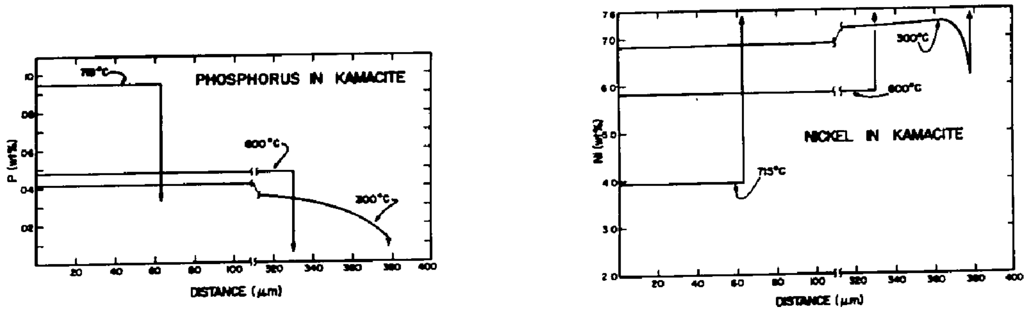

Figure 26. (b) Phosphorus concentration profiles in kamacite (α) for three temperatures. (c) Nickel concentration profiles in kamacite (α) for three temperatures.

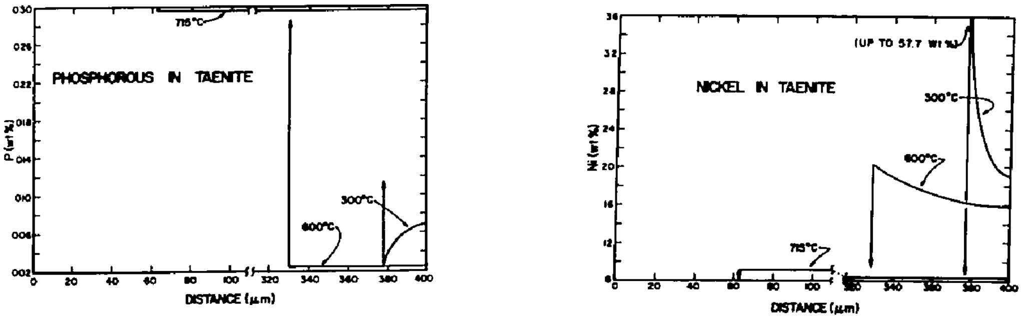

Figure 26. (d) Phosphorus concentration profiles in taenite (γ) for three temperatures.
(e) Nickel concentration profiles in taenite (γ) for three temperatures.

more sluggish and a slight gradient has developed in kamacite. The nickel level in kamacite has increased due to an increase in the interface nickel concentration shown in both Figures 2a and 2c. Nickel diffusion in taenite is the slowest and although the interface concentration is rapidly increasing a highly discernible gradient is developing as shown in Figure 26e. Again, the 600°C tie line does not go through the bulk composition because the system is not in equilibrium. By the time the simulation temperature reaches 300°C several significant changes have occurred. In this particular simulation the tie line defining the interface concentrations became coincident with the $\alpha + \gamma/\alpha + \gamma + Ph$ boundary at $\sim$ 384°C. During the cooling to this temperature the Ni solubility in kamacite has peaked as seen in Figure 15. The nickel solubility in taenite continued to increase considerably as shown by the GLN, GUN curves of Figure 18. This phase diagram shift has caused a general decrease in the phosphorus content at the kamacite interface, but has produced a tie line rotation so that the phosphorus content at the taenite interface has increased. This is shown by the 520°C isotherm and tie line in Figure 26a. APH has continued to decrease, but GPH has increased because of a tie line rotation. The residual effects of this phase diagram expansion and tie line shift and rotation prior to T = 384°C can be seen in the phosphorus kamacite and taenite profiles at T = 300°C, Figures 26b, d. The phosphorus profile in kamacite at T = 300°C is everywhere lower than the profile at T = 600°C. In taenite, however, the phosphorus profile displays a higher concentration with the maximum at the taenite center.

Below T = 384°C, the system is in the $\alpha + \gamma + Ph$ region. The simulation procedure for this situation has already been described. The $\alpha + \gamma/\alpha + \gamma + Ph$ boundary becomes the applicable tie line and the α/γ interface is shifted to allow for nickel conservation. The system now closely parallels a binary system with an inflexible tie line at every temperature. The phosphorus interface concentrations both decrease with decreasing temperature and at such low temperature gradients develop near the α/γ interface in both phases. For this particular simulation, phosphorus has lost $\sim$ 8% of its original mass at T = 300°C.

As shown in Figure 15, the nickel solubility in α increases until $\sim$ 470°C and decreases below that temperature. The initial increase is reflected in the higher Ni level in kamacite at T = 300°C of Figure 26c. The decrease in Ni solubility below T ∿ 470°C is shown by the depletion region near the α/γ interface in the T = 300°C kamacite Ni profile, Figure 26c, from ∿ 365-378μm. This depletion is a well recognized feature of octahedrites and has been taken as evidence that the Ni solubility in α peaks in the range 400-500°C. The nickel concentration at the taenite interface continues to increase so that at T = 300°C, GNI = 57.7wt% nickel. Diffusion is so sluggish that very severe compositional gradients are observed, Figure 26e. Nickel mass, however, is conserved at T = 300°C. In this simulation the total Ni mass change is <.04%. Since only the Ni mass is conserved the cooling rate analysis utilizes only the Ni profile simulation information.

4.3 APPLICATION OF THE SIMULATION MODEL

In order to determine the cooling rates of individual meteorites in the group IVA the results of the simulation model are applied in two ways. Primarily a modification of the Wood method is used as described earlier where cooling rate curves are generated on plots of central taenite nickel vs. log-taenite half width. This method is used because of its general insensitivity to undercooling for taenite half widths $\leq$ 10μm. This insensitivity to undercooling varies from meteorite to meteorite. The degree of undercooling and region of insensitivity will be shown for each meteorite analyzed in the chapter on results. The modified Wood method of analysis produces a cooling rate and the degree of undercooling provided the experimental data is sufficient and adequate.

In the second application of the simulation model a comparison is made between a measured and a simulated nickel profile for the taenite phase. The cooling rate and undercooling are determined using the modified Wood method while the field length, L, is measured from the actual meteorite sample. A comparison is then made between the simulated and measured residual taenite thickness and also between the simulated and measured Ni concentration profile in taenite. This procedure allows one to confirm the results of the modified Wood method. In order to properly apply the modified Wood method and the taenite gradient matching technique it is necessary to understand the effect of parametric changes upon the analyses, i.e. changes in the cooling rate, the degree of undercooling and the field length. For a given meteorite the bulk nickel and phosphorus are fixed. Cooling rate curves for the modified Wood method are generated by selecting a cooling rate and nucleation temperature (initially using no undercooling) and running several simulations using different field length values. A cooling rate curve, such as that shown in Figure 27 by the solid line, is constructed by plotting the simulated central taenite nickel content vs. log taenite half width. Shown in Figure 27 is a 20°C/Myr cooling rate curve. For a given cooling rate and nucleation temperature an increase in the field length causes an increase in the taenite halfwidth and a decrease in the central taenite nickel. A slower cooling rate shifts the curve to the upper right while faster cooling has the opposite effect. By varying both the field length and the amount of undercooling for a given cooling rate, a family of curves are generated for various undercoolings as shown in Figure 27 for undercoolings of 120, 150 and 160°C. As the undercooling is increased it becomes necessary to choose smaller taenite halfwidths before the effect of undercooling disappears. Strictly speaking, undercooling always displays an effect regardless of the size of the residual taenite halfwidths.

In applying the taenite nickel profile matching

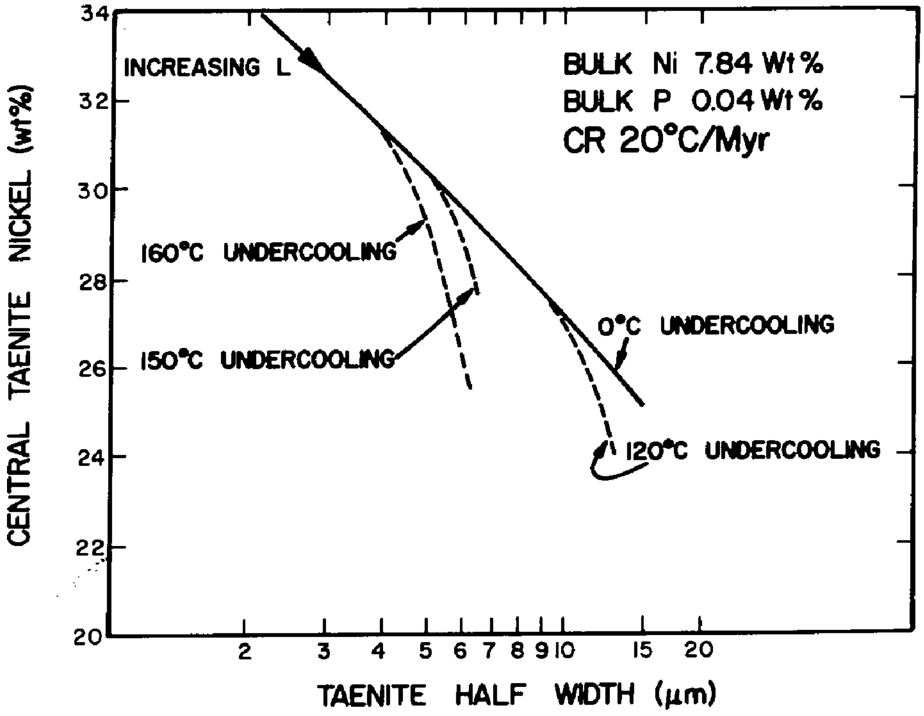

Figure 27. Cooling rate curve with various undercoolings using the modified Wood method.

technique one must be confident that a match between simulation and experiment is unique. For a fixed field length measured from a meteorite sample, it is possible to produce the same residual taenite-half-width by a trade off between cooling rate and under-cooling. This is seen in Figure 28 where taenite halfwidths are plotted vs. cooling rates for a fixed field length and for various undercoolings. For a field length of 360μm, a cooling rate of 50°C/Myr with no undercooling will result in a taenite halfwidth of ∿ 15μm. However, a cooling rate of 15°C with 140°C undercooling will also result in a taenite halfwidth of ∿ 15μm for the same 360μm field length. The taenite nickel profiles for these two cases are, however, remarkably different as is shown in Figure 29. The 50°C/Myr, no undercooling simulation produces a central taenite nickel value of ∿ 22wt% Ni while the 15°C/Myr, 140°C undercooling simulation produces a central taenite nickel value of ∿ 16.6wt% Ni. Such large concentration differences are clearly distinguished by electron microprobe techniques. A match between simulated and measured taenite-half widths and concentration profiles is therefore unique.

Using both techniques it is possible to determine

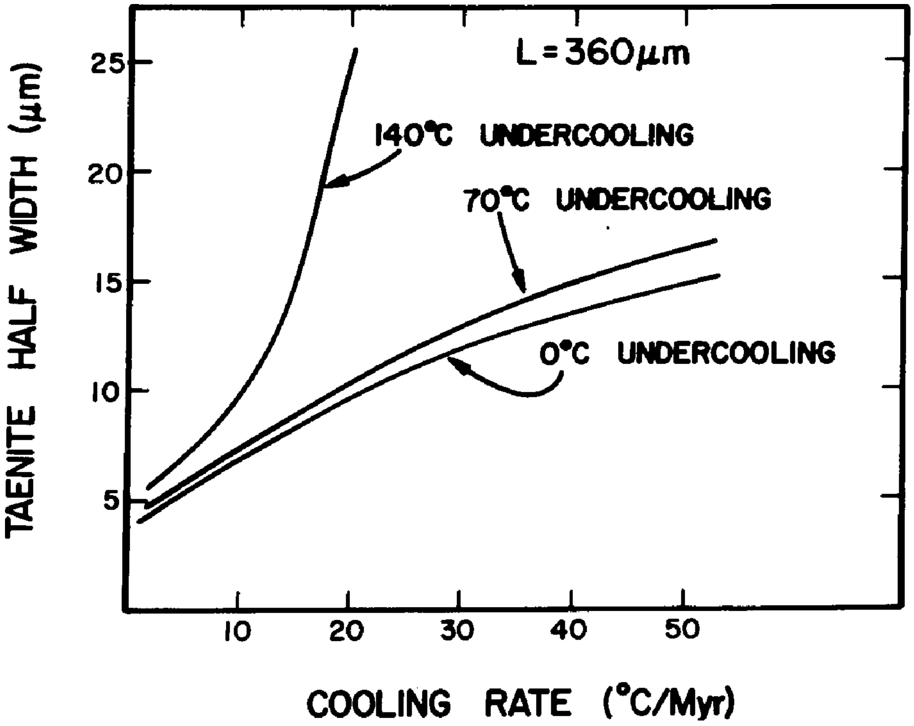

Figure 28. Family of undercooling curves on a plot of taenite half width vs. cooling rate for a fixed field length value.

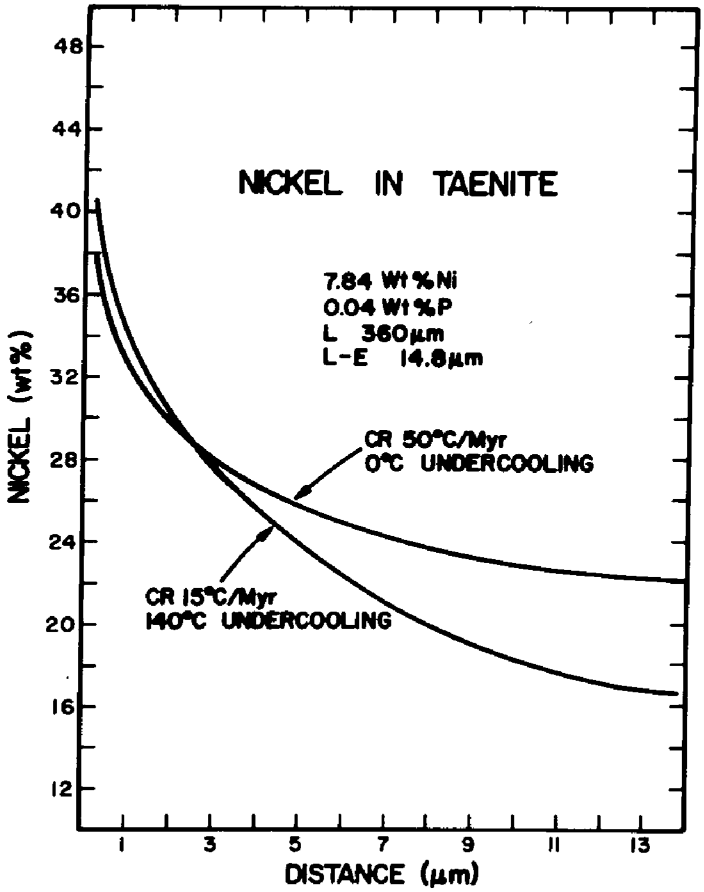

Figure 29. Comparison of taenite nickel curves for cooling rate--undercooling pairs that produce the same taenite half width from the same field length.

a unique cooling rate for a given meteorite and the amount of undercooling necessary to produce the observed taenite-half width and nickel concentration profile in taenite.

EXPERIMENTAL PROCEDURE

This chapter describes the experimental procedure followed in order to obtain measurements of: (1) central taenite nickel and taenite half widths for use in the modified Wood method, (2) nickel concentration profiles in taenite for the profile matching technique. Uncertainty in the measurements is deferred to the Discussion chapter.

The meteorites analyzed in this research are from the Smithsonian Institution, United States National Museum and are listed in Table XIII along with the USNM identification number. Also included in Table XIII are the bulk nickel and phosphorus compositions used as input to the simulation model. Selected bulk nickel and phosphorus values were obtained from the literature for each meteorite. Particular attention was paid to studies such as Moore et al.[61] where both bulk nickel and phosphorus were measured on the same sample. For meteorites where the bulk phosphorus contents are not well established, values were taken from the linear variation of log wt%P vs. log wt%Ni for the IVA irons as shown in Figure 5.

TABLE XIII

GROUP IVA IRON METEORITES ANALYZED

Meteorite	USNM #	Compositions Ni (wt%)	 P (wt%)
La Grange	2870	7.71[Δ]	0.03[Δ]
Signal Mountain	611	7.84[+]	0.04[o]
Gibeon*	--	7.93[o]	0.035[α]
Harriman*	--	7.96[+]	0.045[α]
Para de Minas	1510	8.19[Δ]	0.06[Δ]
Muonionalusta	424	8.42[+]	0.05[o]
Charlotte	991	8.44[Δ]	0.055[Δ]
Mantos Blancos*	--	8.83[±]	0.10[±]
Hill City	1436	9.20[o]	0.12[o,α]
New Westville*	--	9.40[o]	0.14[o]
Chinautla	742	9.48[Δ]	0.165[Δ]
Duchesne	2181	9.58[Δ]	0.15[Δ]

[*] Experimental data from Willis[13]

[Δ] Moore et al.[61]

[+] Schandy et al.[9]

[α] This study, see text

[o] Buchwald[11]

[±] Fletcher [62]

A large number of IVA irons were originally examined. Certain samples were rejected because they had no suitable areas for analysis. The eight meteorites analyzed in this research were chosen because they displayed well defined kamacite bands with suitable taenite ribbons. (Refer to Figures 7 and 8) In addition, these meteorites cover a majority of the range in nickel and phosphorus contents from the low Ni, low P to the high Ni, high P (compare Table XIII with the range in Figure 5). The spread in bulk nickel and phosphorus contents of the eight meteorites insures that any possible variation in cooling rate within the group IVA will be detected. This is particularly true if a relationship exists between cooling rate and bulk nickel content as originally proposed by Goldstein and Short.[37]

For orientation purposes two adjoining surfaces were polished. The surfaces were at right angles to each other. The two surface preparation was done using standard metallographic techniques with polishing through 1μ diamond. The surfaces were moderately etched in a 1% Nital solution and the adjoining edge areas photographed. From the photograph composits suitable kamacite and taenite plate orientations were determined. In some instances, however, it was necessary to recut a sample in order to obtain a proper orientation of kamacite and taenite bands. The optimum orientation is one where the kamacite and taenite plates are normal to the largest polished surface. Measurements with the plates normal to the surface correspond to the model simulation development where planar interface growth is assumed.

The approximate deviation from normal surface intersection for the meteorites analyzed is shown in Table XIV. The deviations are generally $<15^{\circ}$. Recutting to improve orientations with $<15^{\circ}$ deviations was unwarranted due to the small corrections that were necessary. To correct the bandwidths for these slight mis-orientations a multiplication factor equal to the cosine of the angle of deviation was used.

Once a surface was obtained with satisfactory plate orientations suitable areas for analysis were marked using a TUKON tester with either Knoop or diamond pyramid identations. Photographs were taken of the marked areas to facilitate sample orientation during the microprobe analysis. The samples were repolished using 1μ diamond and given a brief hand buff using .06μm alumina. The samples were cleaned ultrasonically

TABLE XIV

SAMPLE ORIENTATION

Meteorite	Deviation Angle (deg.)
La Grange	11
Signal Mountain	14
Para de Minas	1
Muonionalusta	9
Charlotte	11
Hill City	1
Chinautla	15
Duchesne	14, 4

and given a very light etch in a 1% Nital solution. The samples were then placed in a vacuum evaporator overnight and carbon coated just prior to analysis on the electron microprobe.

In selecting suitable areas for analysis the following criteria were employed. The area should be free of inclusions. When possible the taenite ribbon should be sandwiched between equally thick kamacite plates as shown in Figure 8. Finally, the taenite/kamacite boundary should be smooth and regular as seen in Figure 30a rather than jagged or undulating as seen in Figure 30b. These criteria are demanded by the assumptions in the simulation model development, namely (1) that the system is three element, two phase, (2) that the diffusion be one dimensional and (3) that the system be closed, $\frac{\partial C}{\partial x} = 0$, $x = 0, L$.

Concentration values were determined using an ARL electron microprobe. The operating potential was 20kv with a .05μa sample current and a 45 sec count time. The influence of these operating parameters on the analytical sensitivity and the detectability limits will be presented in the Discussion chapter.

The iron and nickel calibration standards were the same ones used by Goldstein et al.[59] The chemical

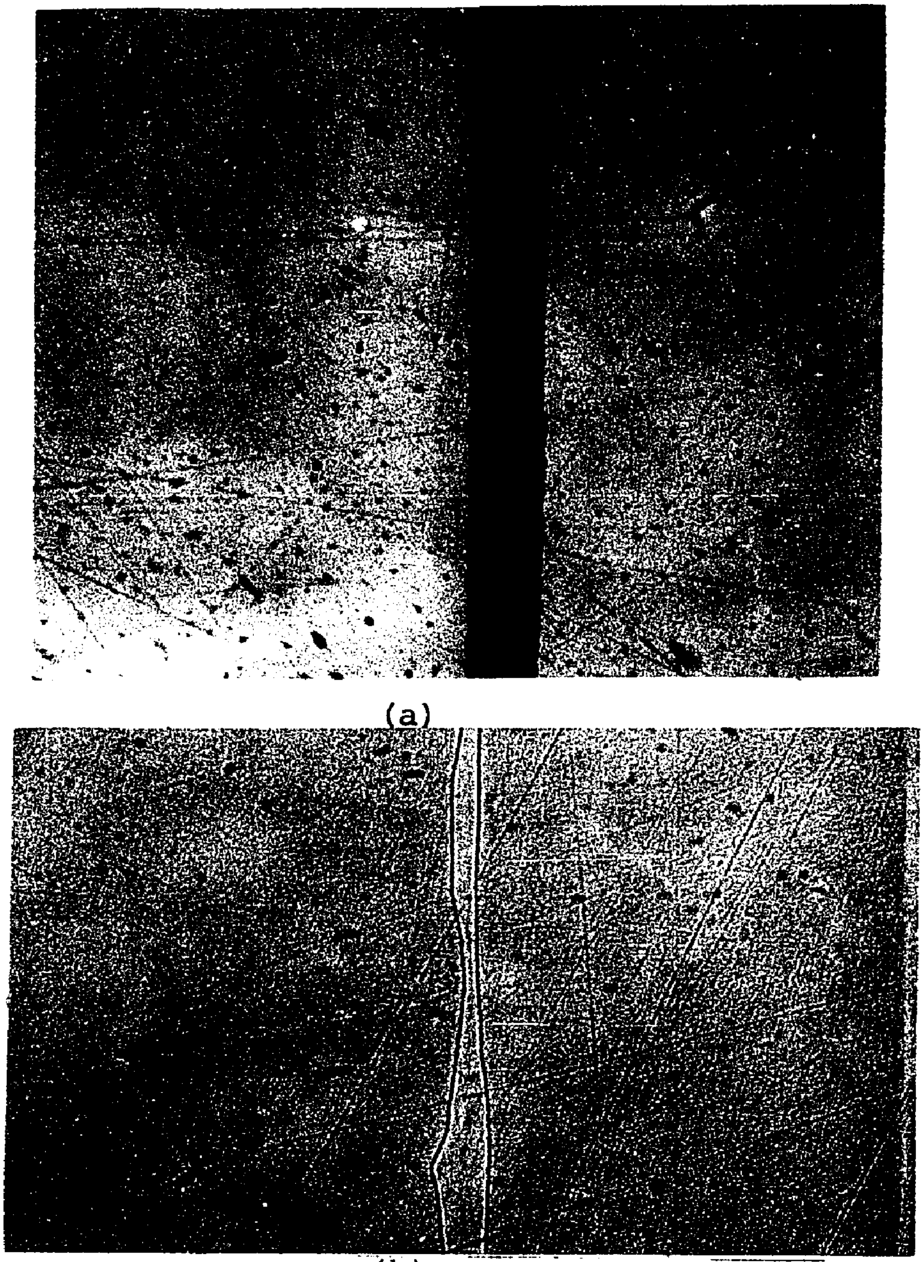

(a)

(b)

Figure 30. (a) Suitable taenite ribbon.
(b) Unsuitable taenite ribbon.
Magnification ∿ 1000X.

analyses of the iron, nickel and Fe-Ni alloys are given in Table XV. Alloy 5 was used predominately as the nickel standard as it most closely approximated the nickel concentrations in the taenite centers. Pure iron was used as the iron standard. Schreibersite, $(Fe,Ni)_3P$, from the iron meteorites Canyon Diablo and Lombard was used as a phosphorus standard. Phosphorus was taken to be stoichiometric at 15.5wt%.

A Tracor Northern minicomputer with Tracor Northern software is interfaced with the ARL electron microprobe. This system was used to obtain x-ray data and perform the conversions to concentrations in wt% for Fe, Ni, and P.

An on-line correction program[63] based on the ZAF correction program of Colby[64] converted the x-ray intensity data measured by the electron microprobe into concentrations in wt%. The program corrects for the fluorescence, absorption, and the atomic number effect. These corrections are discussed at length by several authors, for example Goldstein et al.[65] The measured x-ray intensity ratio is given by

TABLE XV

CHEMICAL ANALYSIS OF ALLOY STANDARDS

Alloy	Nickel (wt%)
Fe	<0.004
1	5.17 ± 0.02
2	10.34 ± 0.02
3	15.17 ± 0.03
4	19.40 ± 0.07
5	25.18 ± 0.05
6	35.32 ± 0.10
7	50.19 ± 0.30
DL-1	75.75
DL-2	90.47
Ni	99.999+

$$(50) \qquad k_A = \frac{I_A}{I_{[A]}} = \frac{C_A}{C_{[A]}} \; \frac{Z_A \, A_A \, F_A}{Z_{[A]} \, A_{[A]} \, F_{[A]}}$$

where the subscript A represents the unknown and the bracketed A is the standard. I is the characteristic x-ray intensity, C is the composition, and Z, A, and F are the atomic number effect, the absorption and fluorescence corrections respectively. k_A is called the k ratio and is defined to be $I_A/I_{[A]}$. In the microprobe analysis k_A is measured, $C_{[A]}$ is known and the terms in the bracket are calculated. However these terms are a function of the unknown C_A. Several iterations of equation (50) are necessary to obtain C_A.

Iron and nickel were always measured and on occasion phosphorus. Phosphorus data was not very meaningful as the simulation model was designed to conserve Ni once the transition $\alpha + \gamma \rightarrow \alpha + \gamma + Ph$ had taken place.

Several measurements were taken at the center of each taenite ribbon. (Refer to Figure 30a) The electron beam was displayed electronically (always <20μm from the normal incidence position). Concentration profiles under 40μm in length were measured by beam displacement. This technique permitted small step sizes to be taken near the α/γ interfaces. For longer profiles, >40μm, a stepping motor was used that displaced the sample in incremental steps. Occasionally the two techniques of beam displacement and sample displacement were combined.

In order to determine the taenite half width the analyzed areas were optically photographed at high magnification, normally at ∿ 1000x. The magnification was calibrated by photographing a Bauch and Lomb stage micrometer at several magnifications. A straight edge with 50 div/inch was used to compare taenite thicknesses with the stage micrometer. The taenite half widths were then corrected for orientation (Table XIV).

Plots of central taenite nickel vs. taenite half width were then constructed for each meteorite. The Wood method was also used by Willis,[13] and Willis and Wasson.[55] They also measured central taenite nickel vs. taenite half width on several IVA iron meteorites. Two meteorites studied by Willis and Wasson[55] were also investigated here. There is excellent agreement of central taenite nickel vs. taenite half width data for the two studies. Figure 31 displays the results for the meteorite Para de Minas.

The experimental results including taenite profile matching are presented in the next chapter.

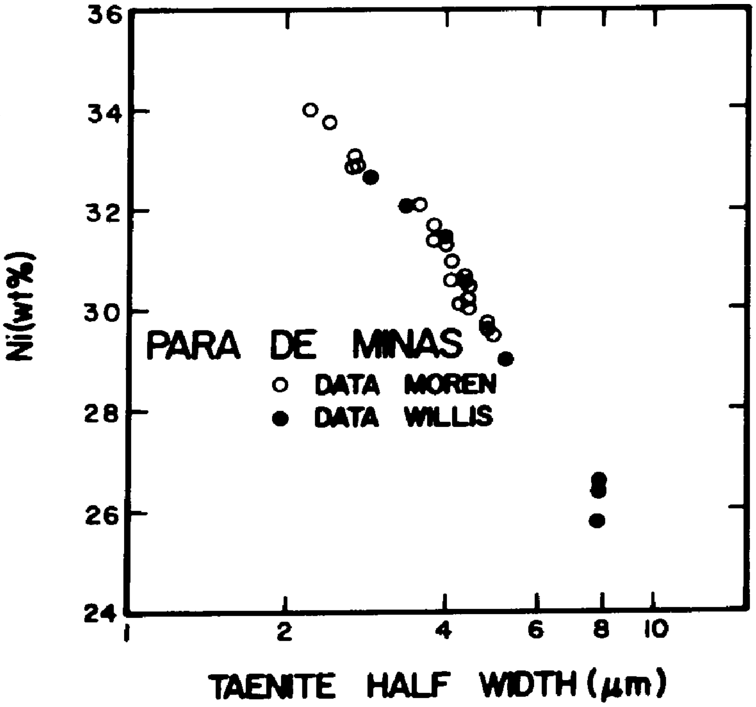

Figure 31. Comparison of measured central taenite nickel and taenite half width values for the same meteorite in two independent studies.

RESULTS

6.1 MODIFIED WOOD METHOD

The calculated cooling rate curves for the ternary form of the Wood method are shown in Figures 32 a-ℓ for the 12 meteorites studied. Measured data from this study for 8 meteorites and data from Willis[13] for 6 meteorites are plotted on these Figures. Also shown in some of the Figures are calculated undercooling curves. The effect of undercooling explains the transverse nature of the data across the cooling rate curves which are generated assuming no undercooling. These undercooling curves should not be taken to imply that suddenly at some set undercooling all the nucleation commenced for a given meteorite. There exists a range of possible undercoolings. This can be seen in the undercooling curves for Muonionalusta, Figure 32f where portions of the measured data are fit with a 180°C undercooling curve and other data are fit with a 160°C undercooling curve.

Table XVI lists the meteorite cooling rates obtained from the cooling rate curves of Figures 32a-ℓ. The calculated taenite half width where undercooling

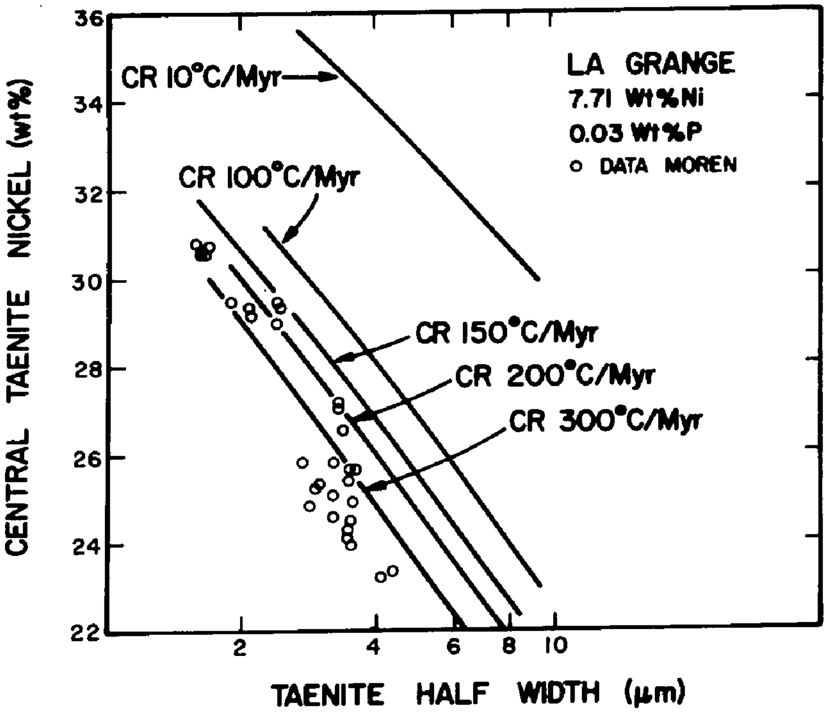

Figure 32. (a) Cooling rate curves for La Grange.

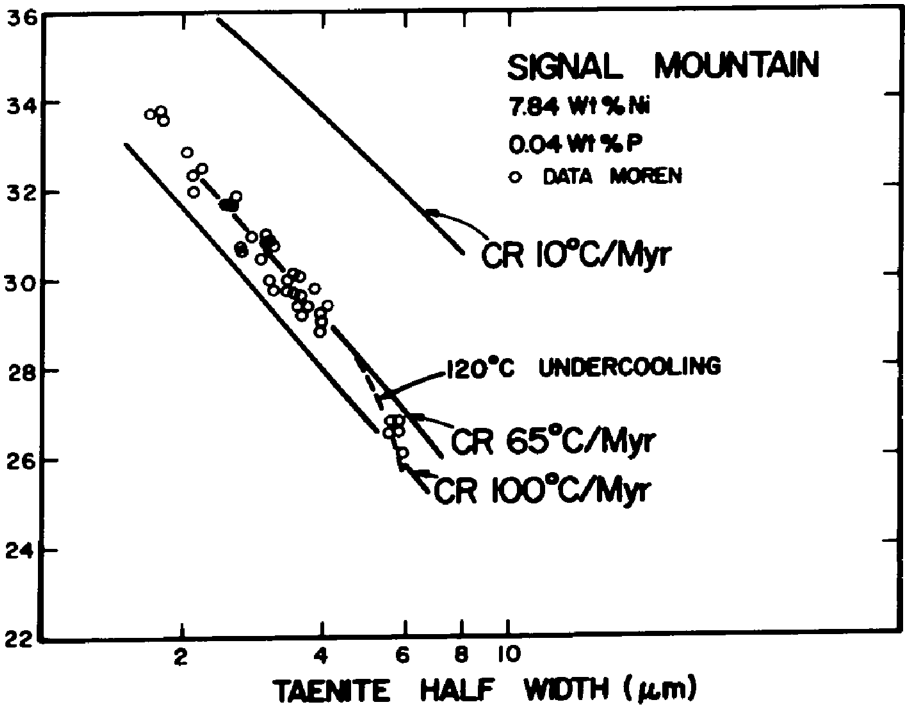

Figure 32. (b) Cooling rate curves for Signal Mountain.

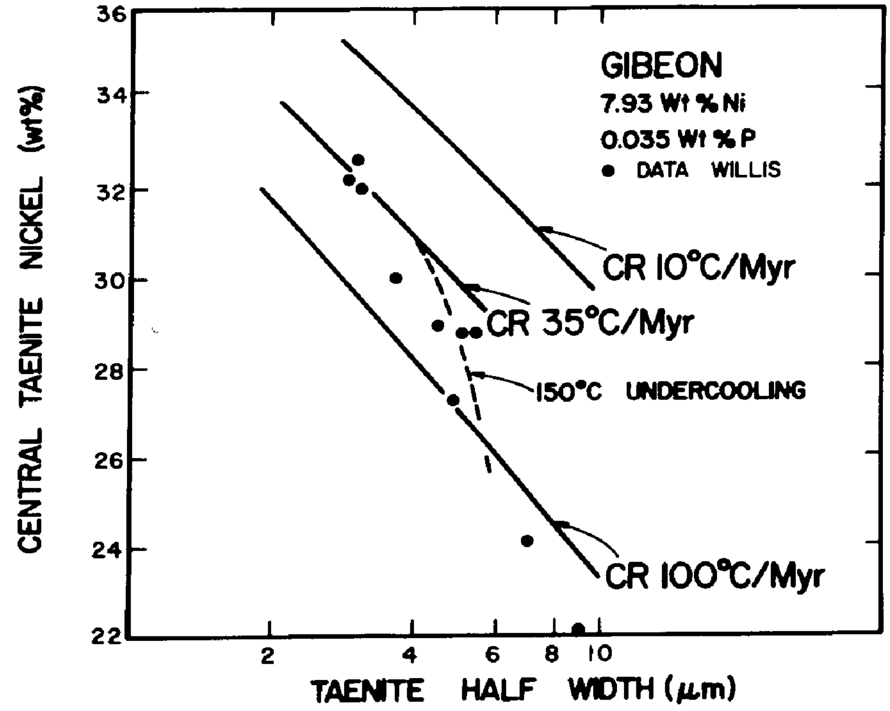

Figure 32. (c) Cooling rate curves for Gibeon.

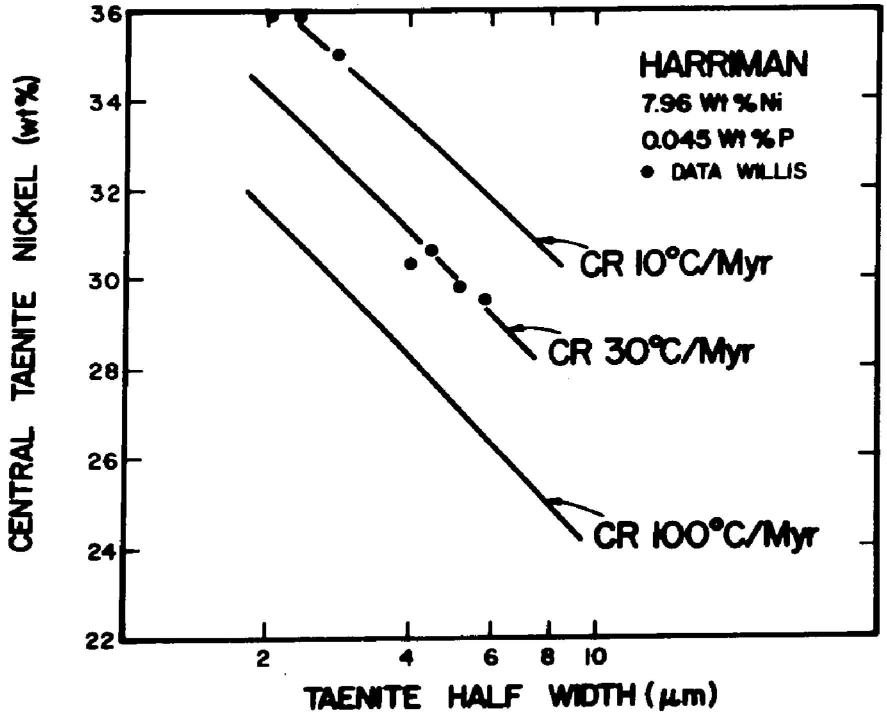

Figure 32. (d) Cooling rate curves for Harriman.

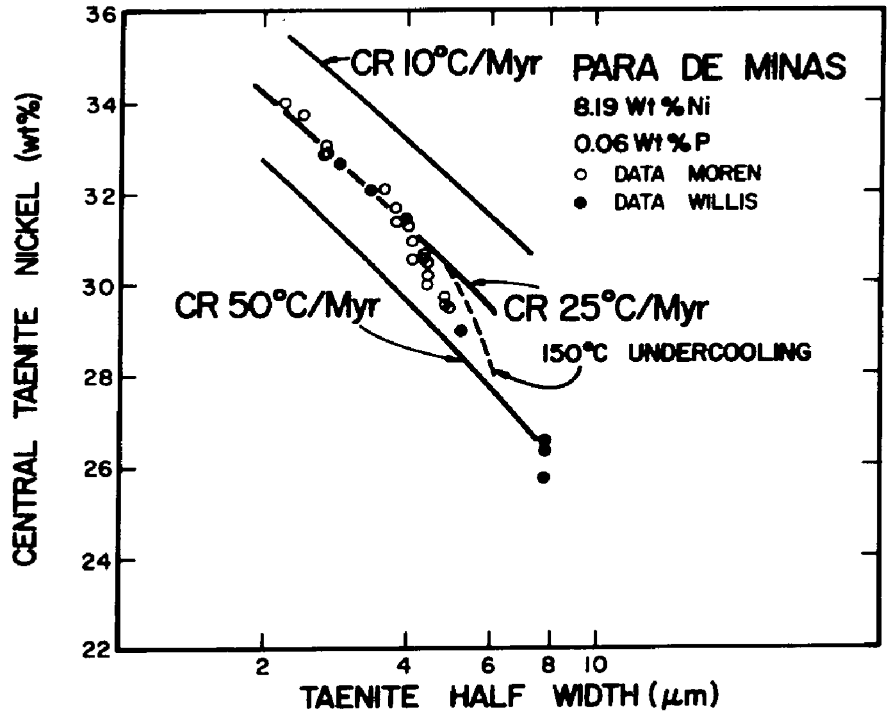

Figure 32. (e) Cooling rate curves for Para de Minas.

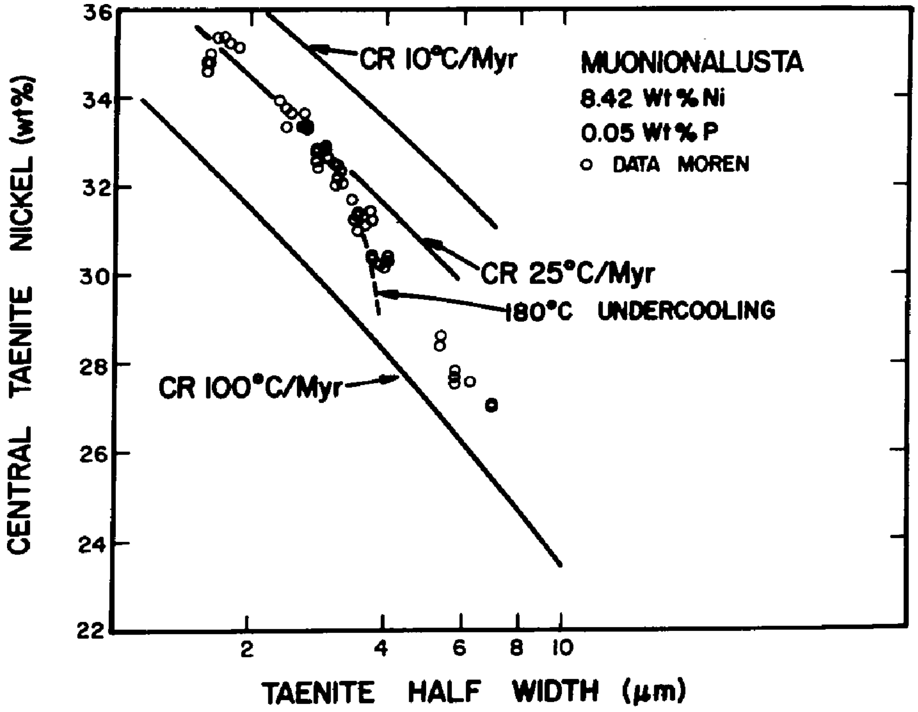

Figure 32. (f) Cooling rate curves for Muonionalusta.

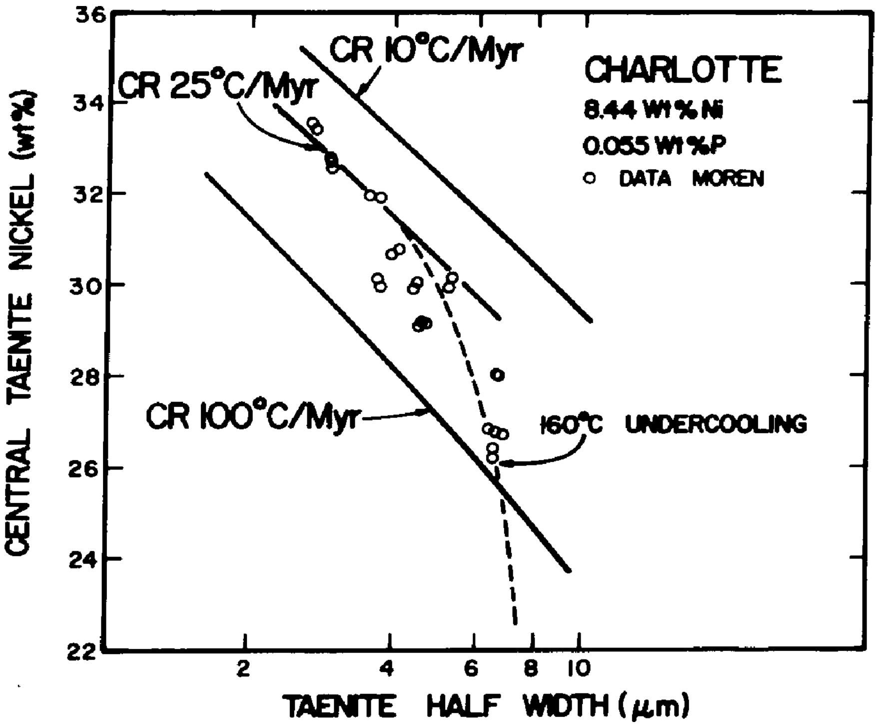

Figure 32. (g) Cooling rate curves for Charlotte.

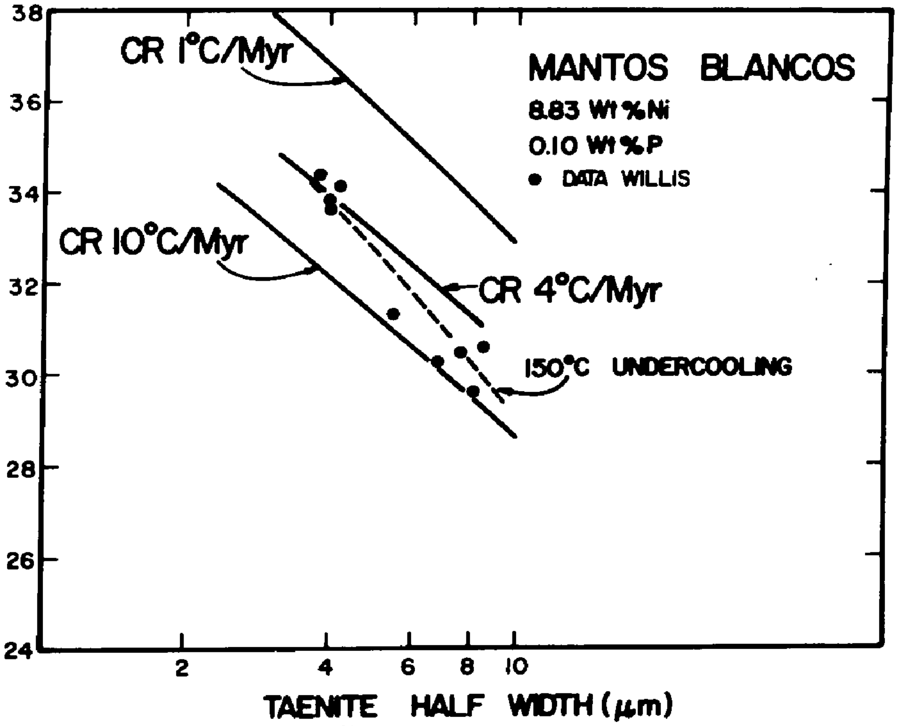

Figure 32. (h) Cooling rate curves for Mantos Blancos.

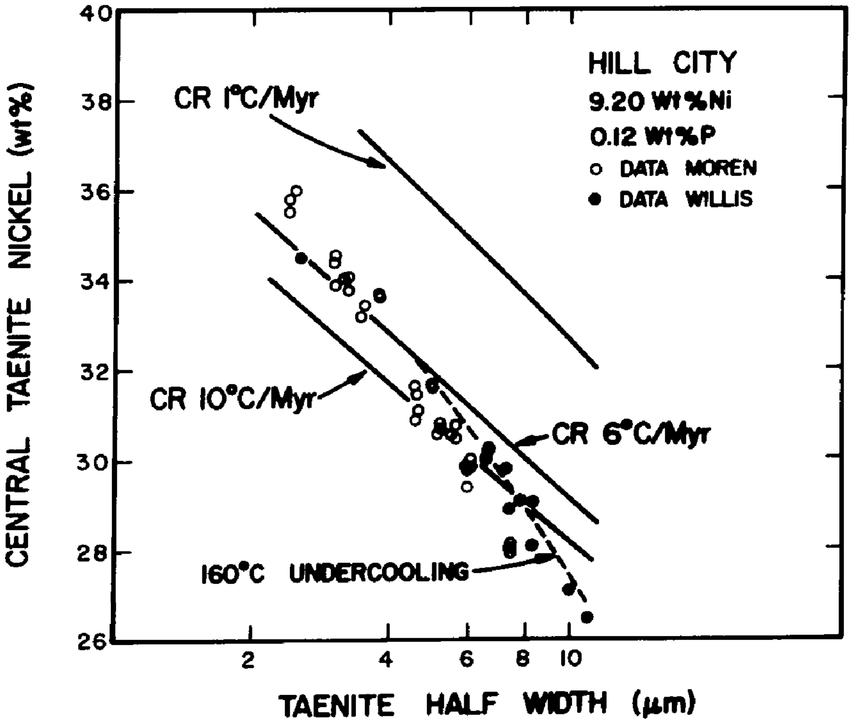

Figure 32. (i) Cooling rate curves for Hill City.

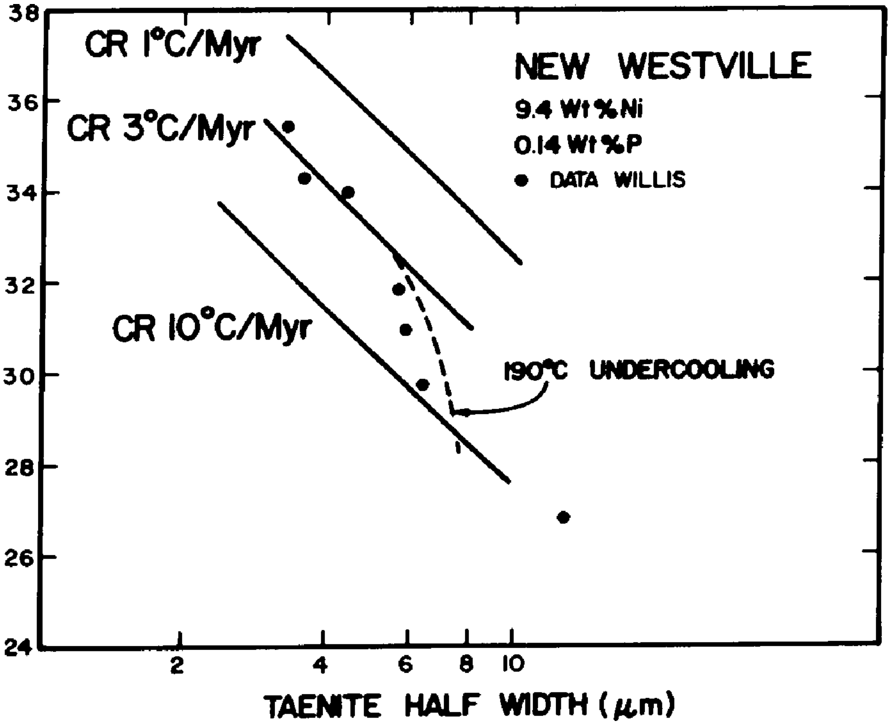

Figure 32. (j) Cooling rate curves for New Westville.

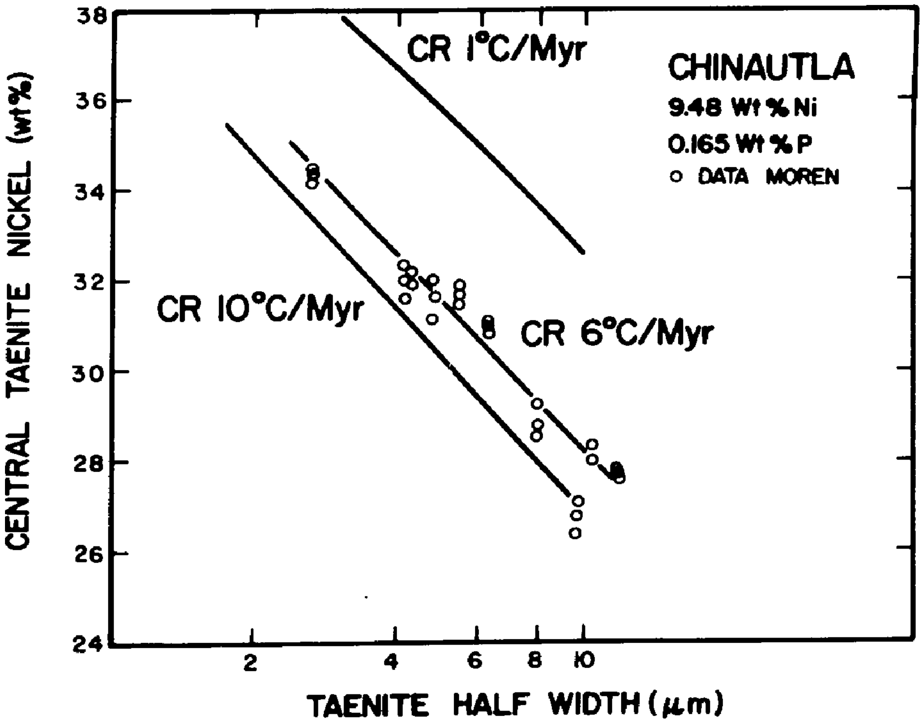

Figure 32. (k) Cooling rate curves for Chinautla.

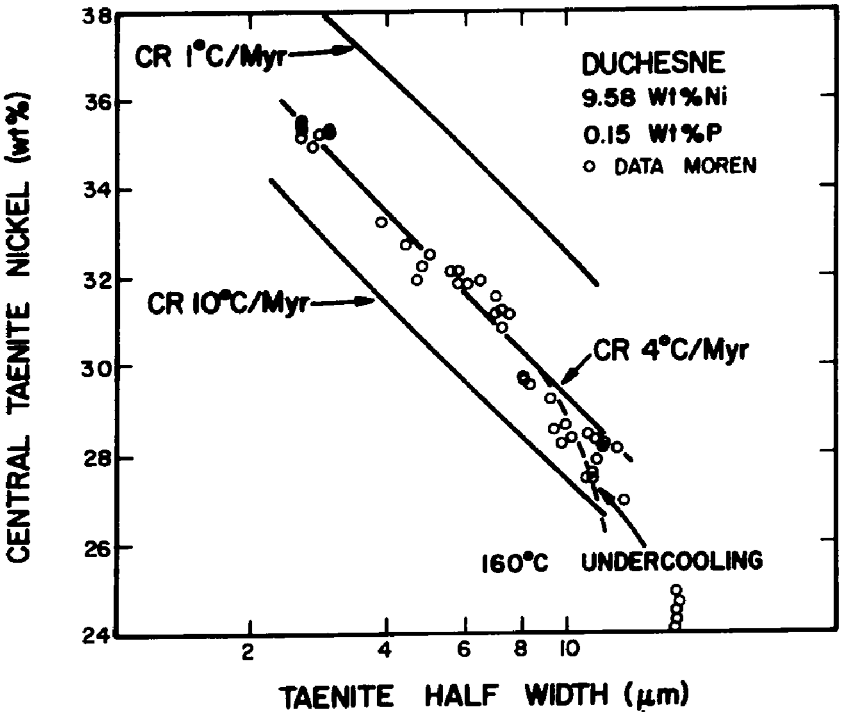

Figure 32. (ℓ) Cooling rate curves for Duchesne.

TABLE XVI

COOLING RATE RESULTS

Meteorite	Ni (wt%)	Cooling Rate ($^{o}C/10^{6}$ yrs.)	Undercooling (^{o}C)	Half Widths For Undercooling Effects (μm)
La Grange	7.71	150-300	-	-
Signal Mountain	7.84	65	120	4.5
Gibeon	7.93	35	150	4
Harriman	7.96	10-30	-	-
Para de Minas	8.19	25	∿160	4-5
Muonionalusta	8.42	25	∿180	3-4
Charlotte	8.44	25	∿160	4
Mantos Blancos	8.83	4	150	3-4
Hill City	9.20	6	160	4-5
New Westville	9.40	3	190	5-6
Chinautla	9.48	6	-	-
Duchesne	9.58	4	∿160	>8

effects appear to be significant are listed for each meteorite. The maximum amount of undercooling determined for several meteorites are also given. For La Grange (Figure 32a) and Harriman (Figure 32d) only a range of cooling rates are determined because of a spread in the data. In general cooling rates decrease with increasing bulk nickel content for the group IVA iron meteorites. Undercooling of up to 190°C are observed.

6.2 TAENITE GRADIENT MATCHING

The results for the taenite gradient matching technique are shown in Figures 33a-f. Both calculated and measured nickel concentration profiles in taenite are shown. The kamacite/taenite interface location does not necessarily correspond to x = 0 on the distance scale, but is in general within ± 1 μm of x = 0. The taenite gradient matching technique was applied to four meteorites, Signal Mountain, Para de Minas, Muonionalusta, and Duchesne, whose bulk nickel and phosphorus contents span most of the range for the group IVA. The cooling rates determined by the Wood method were used in the simulations. In order to determine the field length, L, the measured nickel

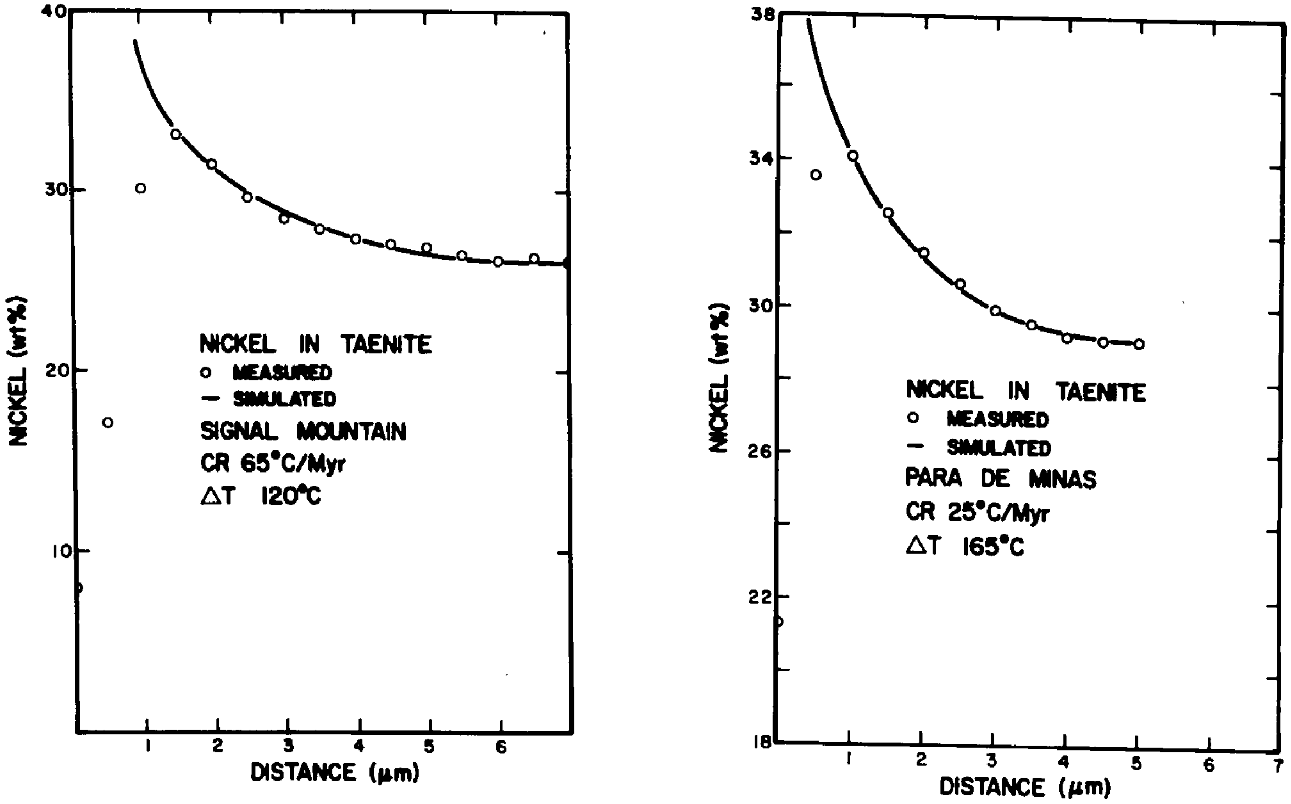

Figure 33. (a) Measured and simulated taenite nickel profile for Signal Mountain. (b) Measured and simulated taenite nickel profile for Para de Minas.

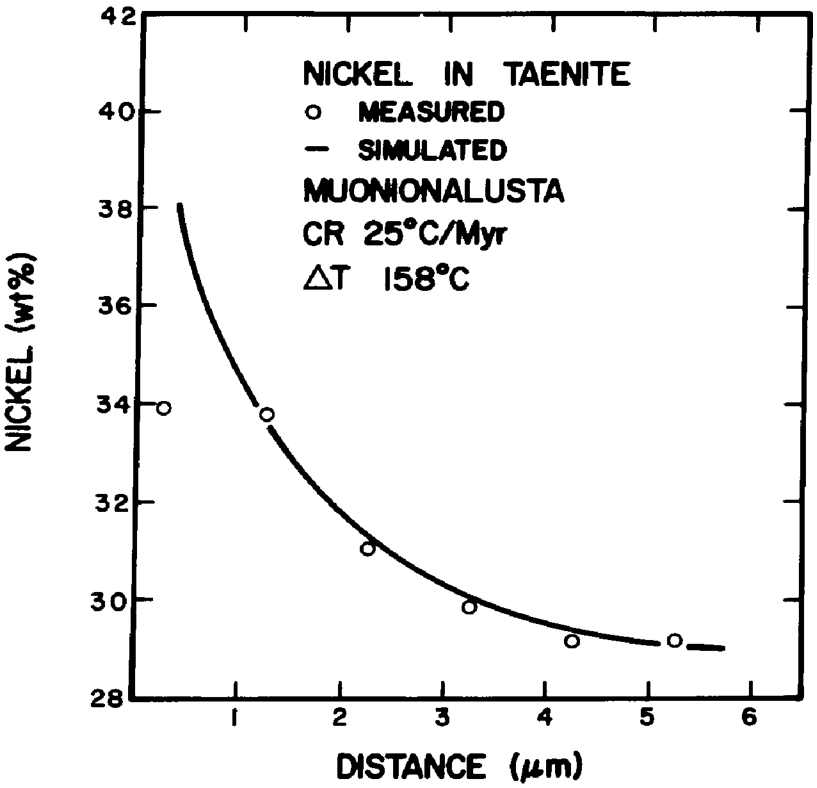

Figure 33. (c) Measured and simulated taenite nickel profile for Muonionalusta.

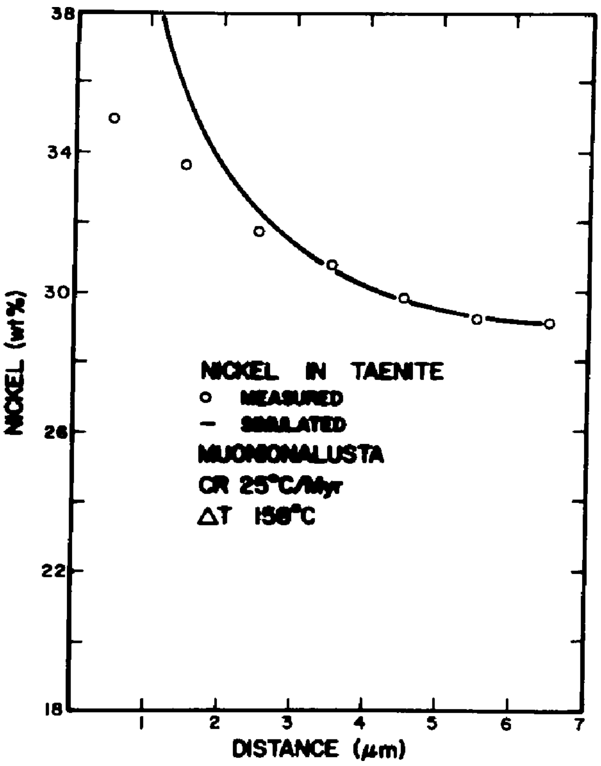

Figure 33. (d) Measured and simulated taenite nickel profile for Muonionalusta.

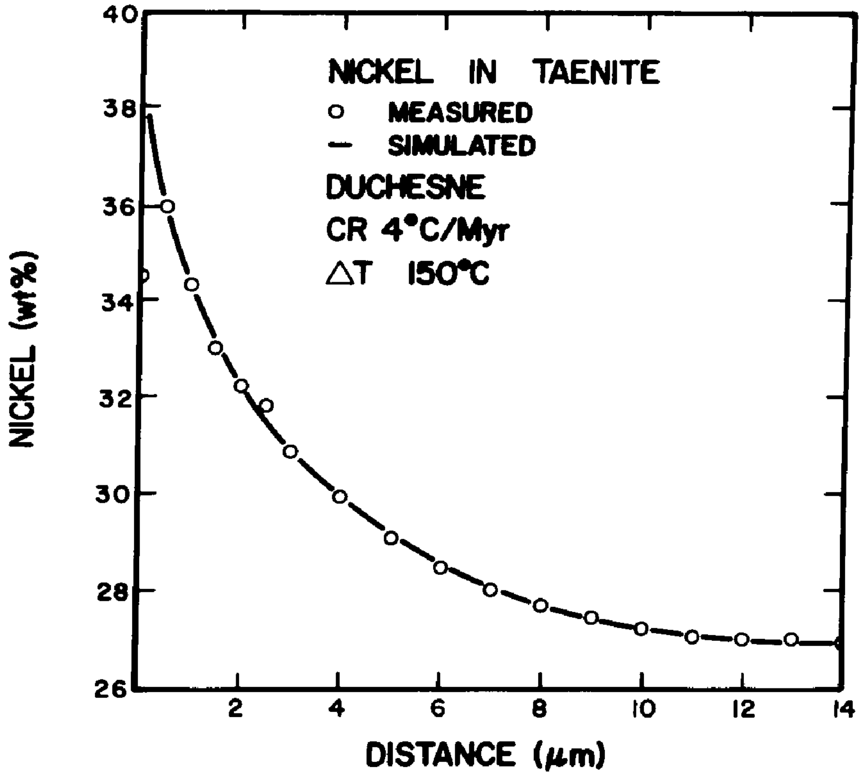

Figure 33. (e) Measured and simulated taenite nickel profile for Duchesne.

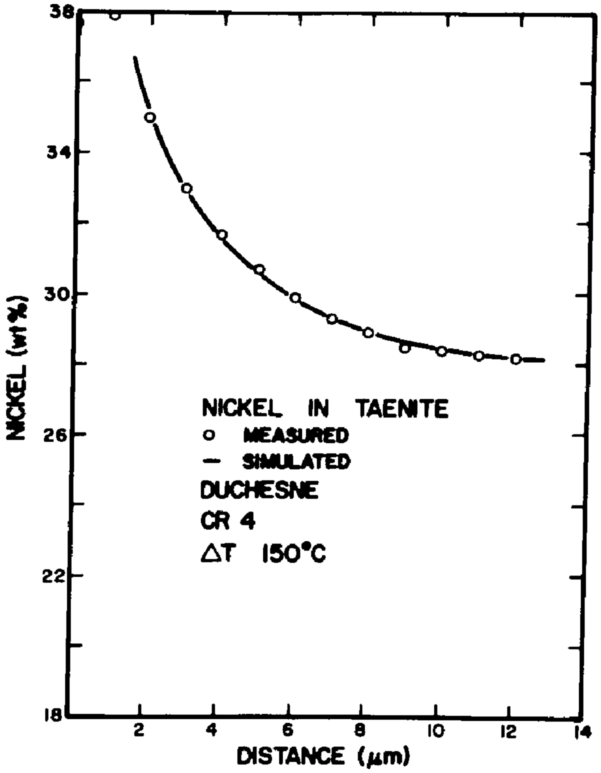

Figure 33. (f) Measured and simulated taenite nickel profile for Duchesne.

concentration profile across the kamacite and taenite phases was plotted. The area under the nickel concentration curve was measured graphically. The field length was determined when the graphically measured area and field equalled the original mass or area given by BULKN*L. Calculated and measured profiles agree closely as shown in Figures 33a-f. The measured amounts of undercooling, $\Delta T(^{o}C)$, are summarized in Table XVII. Also listed in Table XVII are the bulk compositions, the cooling rate, the graphically determined field length values and the field length values used for each simulation. The measured amounts of undercooling range from 120-165°C. The reasons for the differences between the measured field length values and the ones used in the simulations will be discussed in the next chapter.

TABLE XVII

TAENITE GRADIENT MATCHING RESULTS

Meteorite	Ni (wt%)	P (wt%)	CR ($^{o}C/10^{6}$ yrs.)	Undercooling (^{o}C)	Computed L (μm)	Simulation L (μm)
Signal Mountain	7.84	.04	65	120	225	185
Para de Minas	8.19	.06	25	165	125	132
Muonionalusta	8.42	.05	25	158	152	119
Muonionalusta	8.42	.05	25	158	169	119
Duchesne	9.58	.15	4	150	154	145
Duchesne	9.58	.15	4	150	157	130

DISCUSSION

The modified Wood method has been applied to 12 group IVA iron meteorites. A variation in cooling rates was observed for these meteorites. The cooling rate is inversely related to the bulk nickel content. The taenite gradient matching procedure shows that the cooling rate determined using the Wood method can produce the measured taenite half width and nickel concentration profile for a measured field length by varying the amount of undercooling. A more detailed description of the gradient matching procedure will be given after an analysis of the uncertainties associated with the Wood method.

It is imperative to ascertain whether the resultant cooling rate variations across the group are real or can be explained by the uncertainties in measured data and input parameters. The implication of the results will be discussed in the last section in terms of previously proposed parent body models.

7.1 ERROR ANALYSIS

There are two separate sources of error in determining the cooling rates of the group IVA iron meteorites. The first involves the placement of the measured data on the central taenite nickel vs. taenite half width field, and the second involves the placement of the simulation based cooling rate curves on the same central taenite nickel vs. taenite half width field.

DATA PLACEMENT

Data placement involves two measurements; central taenite nickel concentrations measured using the ARL electron microprobe and taenite half widths measured using high magnification optical photographs.

NICKEL CONCENTRATION

Statistical variations in the x-ray counts during the microprobe analysis are a source of error for the measured nickel concentrations. It is assumed that three standard deviations, i.e., $\pm 3\sqrt{\bar{N}}$, where $\bar{N}$ is the average number of x-ray counts, are sufficient to describe the error in a nickel concentration measurement. Nickel contents are uncertain to ± 0.1 - 0.2 wt% corresponding to nickel concentrations of 7.4 and 33 wt% respectively. Calibration by standards and machine drift over long measurement times increases the measurement uncertainty. Based on an analysis of nickel concentration measurements taken in the same areas, the uncertainty in the nickel concentration values at the

2σ confidence interval is ± 0.3 wt% at the high nickel taenite centers. The uncertainty in the nickel concentration measurements in the α phase (Ni $\sim$ 7.3 wt%) is realistically ± 0.2 wt%.

The orientation of the taenite ribbon affects the measured Ni concentration value at the taenite center. The more the taenite and kamacite plates deviate from being normal to the polished surface, the greater the increase in the measured nickel content. This is due to the combined facts that the microprobe data come from a finite volume element and that the Ni content increases on approaching the γ/α interface. The orientation does not affect the uncertainty in the measurement; it gives a slightly higher concentration reading. The errors associated with plate orientation are minimized by analyzing samples that have less than a 15° deviation (see Table XIV).

A taenite ribbon sandwiched between kamacite plates having different thicknesses will also produce higher Ni concentration measurements. Unequally thick adjacent kamacite plates produce asymmetrical profiles in taenite and the nickel minimum will not be located at a taenite center. Non parallel taenite borders (Figure 30b) will produce erroneous absolute nickel concentration measurements. Such regions were avoided.

TAENITE HALF WIDTHS

Taenite bands, where Ni measurements had been taken, (see Figure 30a), were optically photographed at ∿ 1000X. A Bausch and Lomb stage micrometer with .01 mm divisions was photographed at the same magnification. A comparison between the photographed standard and the photographed taenite band was made using a straight edge marked in 50 divisions per inch. The taenite band widths could be measured within 0.5 division on the 50 division/inch scale. This corresponds to $\lesssim \pm$ 0.25 μm for the taenite band width, or $\lesssim \pm$ 0.13 μm for the taenite half width. The taenite half width measurements are affected by plate orientation. The taenite width measured from the photograph is not the true thickness of the taenite band if the taenite band is not normal to the photographed surface. The true taenite band width is given by:

$$\text{true width} = \text{measured width} * \cos\theta$$

where θ is the angle of deviation given in Table XIV.

DATA TREND

The uncertainties in the concentration measurements and the taenite half width measurements are random.

They are reflected in the data scatter on the cooling rate curves, Figures 32a-ℓ. Since a variation in cooling rates across the group IVA is indicated, uncertainties of ± .13 μm in the taenite half width and ± 0.3 wt% in the nickel concentration lead to uncertainties in the cooling rates that vary according to the meteorite. Two end members, Signal Mountain and Duchesne will be used to quantize these uncertainties in data measurements.

Signal Mountain: The uncertainties of ± 0.13 μm in the taenite half width and ± 0.3 wt% in the central taenite nickel concentration expand the data band on the plot of central taenite nickel vs. taenite half width shown in Figure 32b. The simulation based cooling rate curves that contain this expanded data band are 50°C/Myr on the slow cooling rate side and 100°C/Myr on the fast cooling rate side. The simulation based cooling rate curve through the center of this expanded data band remains at ∿ 65°C/Myr. The distance of separation between a sequence of cooling rate curves is not linear, but log-like, i.e. the separation between a 10°C/Myr cooling rate curve and a 20°C/Myr cooling rate curve is greater than the separation distance between an 80°C/Myr cooling rate curve and a

100°C/Myr cooling rate curve. This log-like behavior in cooling rate curve separation means that for fixed uncertainties in the data measurements there is less of a shift in cooling rate on the slow cooling rate side (-15°C/Myr in this example) and more of a shift in cooling rate on the fast cooling rate side (+ 35°C/Myr in this example).

Duchesne: The uncertainties of ± 0.13 μm in the taenite half width and ± 0.3 wt% in the central taenite nickel concentration expand the data band on the plot of central taenite nickel vs. taenite half width shown in Figure 32ℓ. The simulation based cooling rate curves that contain this expanded data band are 3°C/Myr on the slow cooling rate side and 7°C/Myr on the fast cooling rate side. The simulation based cooling rate curve through the center of this expanded data band remains at 4°C/Myr. Again, due to the log-like nature of the separation distance between cooling rate curves there is less of a shift on the slow cooling rate side (- 1°C/Myr in this example) and more of a shift on the fast cooling rate side (+ 3°C/Myr in this example).

When the approximately 65% increase on the fast cooling rate side and 25% decrease on the slow cooling rate side due to measurement uncertainties is applied to the remaining samples the result is a cooling rate spread for each meteorite. The cooling rate range for each meteorite that encompass the measured data plus measurement uncertainties is listed in Table XVIII. Even with the expanded range of cooling rates for each meteorite there is an observable variation in the cooling rates in going across the group as a whole.

COOLING RATE CURVE PLACEMENT

There are two contributing factors to the error in the placement of the simulation based cooling rate curves on the central taenite nickel vs. taenite half width field. The first is due to the numerical approximation technique. The second is due to the input parameters, which include bulk compositions, diffusion coefficients and the equilibrium phase diagram. These factors primarily affect the absolute value of the cooling rates. They can, however, cause an expansion or contraction of the separation between cooling rate curves. Consequently, the difference in cooling rates between two meteorites can increase or decrease. Each of these factors will be discussed separately.

NUMERICAL MODEL

The Crank-Nicholson finite difference technique

TABLE XVIII

COOLING RATE SPREAD DUE TO DATA MEASUREMENT UNCERTAINTY

Meteorite	CR This Study ($^{o}C/10^{6}$ yrs.)	CR Range To Enclose Measurement Uncertainty ($^{o}C/10^{6}$ yrs.)
La Grange	150-300	>110
Signal Mountain	65	50-100
Gibeon	35	26-57
Harriman	10-30	8-50
Para de Minas	25	20-40
Muonionalusta	25	20-40
Charlotte	25	20-40
Mantos Blancos	4	3-6
Hill City	6	5-10
New Westville	3	2-5
Chinautla	6	5-10
Duchesne	4	3-7

allows second order correct analogs of the concentration derivatives. Round off errors are difficult to calculate for the specific application and are overridden by input parameter uncertainties.

One of the good features of this technique is that the number of grid points remains fixed. This avoids the necessity of adding grid points through linear interpolation, a technique required by other numerical approximation schemes. The interface shift and repositioning of internal grid points is built into the mathematical model. This avoids the necessity of an interpolation technique to reposition the grid points.

The errors associated with the numerical technique are minimal and affect each growth simulation in the same manner.

INPUT PARAMETERS

It is impossible to accurately analyze all the possible combinations of input parameter variations. Since the research objective is not only to determine the absolute cooling rates, but to determine if there is a significant and consistent cooling rate variation across the group, the following procedures were adopted. An analysis was performed on the input parameters that produced the most significant shifting of the simulation based cooling rate curves. An analysis was also performed on the input parameters that have been the subject of disagreement among researchers. These input parameters are: (1) the bulk compositions, (2) the solubility of Ni in α, and (3) the diffusivity of Ni in α. The analysis consisted of observing the magnitude and direction of the shift in the simulation based cooling rate curves on plots of central taenite nickel vs. taenite half width as these input parameters were varied.

BULK COMPOSITIONS

In a purely binary model, a shift in the cooling rate curves is due to a change in the bulk composition. Bulk composition changes greatly affect the position of the cooling rate curves in a ternary system also. This is obvious by observing the shift in the position of the 10°C/Myr cooling rate curve between Figures 32b and 32ℓ. The primary concern here, however, is how bulk composition uncertainties affect the cooling rate curves for an individual meteorite.

It was shown in Figure 5 that a roughly linear relationship exists between log-P and log-Ni. Two parallel lines were drawn on Figure 5 to enclose a majority of the log-P vs. log-Ni data. These lines established reasonable P and Ni limits. Assuming the bulk nickel content for a meteorite (Table XIII) is correct phosphorus limits are defined by the parallel lines. Conversely, assuming the bulk phosphorus content for a meteorite (Table XIII) is correct nickel limits are defined by the parallel lines. Nickel and phosphorus limiting values determined in this manner were input to the simulation model. This procedure was used for three meteorites, Signal Mountain, Para de Minas and Duchesne. Table XIX lists the bulk compositions for the three meteorites, the bulk composition changes, and the cooling rate shifts due to the composition changes.

Bulk composition uncertainties more strongly affect the cooling rates for the low Ni, low P group IVA members. An increase in the bulk nickel content increases the observed cooling rate. However, increasing the bulk P content decreases the observed cooling rate. In going across the group IVA from the low Ni, low P end to the high Ni, high P end, the effects of increased phosphorus outweight the effects of the

TABLE XIX

EFFECTS DUE TO BULK COMPOSITION VARIATIONS FOR THREE METEORITES

Affected Element	Ni (wt%)	P (wt%)	Result
			Signal Mountain
None	7.84	.04	CR 65°C/Myr
Ni increase	8.29	.04	Faster Cooling ∿ +3°C/Myr
P decrease	7.84	.024	Faster Cooling ∿ +10°C/Myr
			Para de Minas
None	8.19	.06	CR 25°C/Myr
Ni decrease	7.69	.06	Slower Cooling ∿ -2°C/Myr
Ni increase	8.69	.06	Faster Cooling ∿ +1°C/Myr
P decrease	8.19	.035	Faster Cooling ∿ +8°C/Myr
			Duchesne
None	9.58	0.15	CR 4°C/Myr
Ni decrease	9.07	0.15	Slightly Faster Cooling <+1°C/Myr
P increase	9.58	0.24	No Observable Shift

increased nickel, i.e. the cooling rate curves shift to slower absolute cooling rates as is indicated in a comparison of Figures 32b and 32ℓ.

All of the parameters discussed to this point are peculiar to a given meteorite; measured data of central taenite nickel and taenite half width and simulation input of bulk nickel and phosphorus contents. Only these parameters provide a distinction in the cooling rates determined for each meteorite.

Two meteorites can have the same cooling rate in two cases: (1) both meteorites produce the same measured data of central taenite nickel and taenite half width, and have the same bulk compositions, (2) the meteorites produce different measured data and have different bulk compositions. That case (1) yields identical cooling rates is obvious. Identical cooling rates from case (2) is not obvious. Figure 34 shows three sets of central taenite nickel vs. taenite half width data. From lower left to upper right the bulk nickel and bulk phosphorus contents increase for the meteorites displayed. The cooling rates of these three meteorites could be the same if the cooling rate curves generated through the simulation model shifted in the same manner as the data. What actually occurs is an

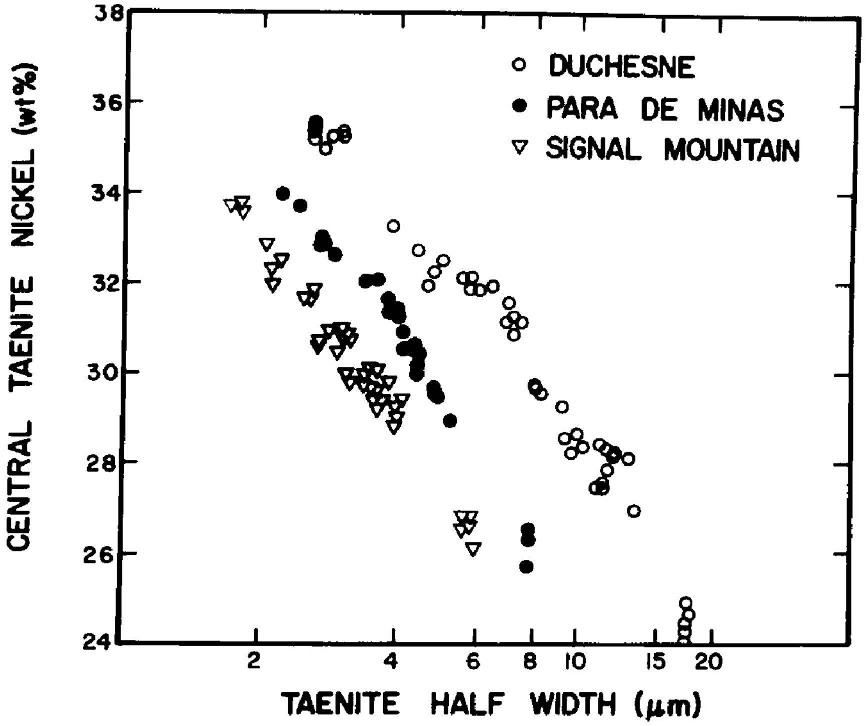

Figure 34. Comparison of measured data for three group IVA meteorites.

opposite effect. As the bulk nickel and bulk phosphorus are increased the cooling rate curves are shifted so as to produce slower cooling rates (see Figures 32b and 32ℓ.

In summary the data for meteorites of sufficiently different bulk compositions do not overlap. In addition the bulk composition changes produce cooling rate curves that further increase the difference in cooling rates between different meteorites.

PHASE DIAGRAM

Altering the applicable phase diagram in the simulation model produces a shift in the cooling rate curves. The greatest shifts in cooling rates are due to changes in the nickel solubility in α. In order to investigate these effects the nickel solubility limits in α were changed. Figure 35 shows a set of new nickel solubility limits. The curves for ALN and AUN both go through the experimental points at higher temperatures. The peaks in these curves occur at $T = 450^{\circ}C$. The maximum nickel solubility is $\sim$ 7.33 wt% in the ALN curve and $\sim$ 7.93 wt% in the AUN curve. These new nickel solubility limits produce simulated kamacite profiles quite different from those shown in Figures 16 and 17. The new simulated curves are higher in nickel content.

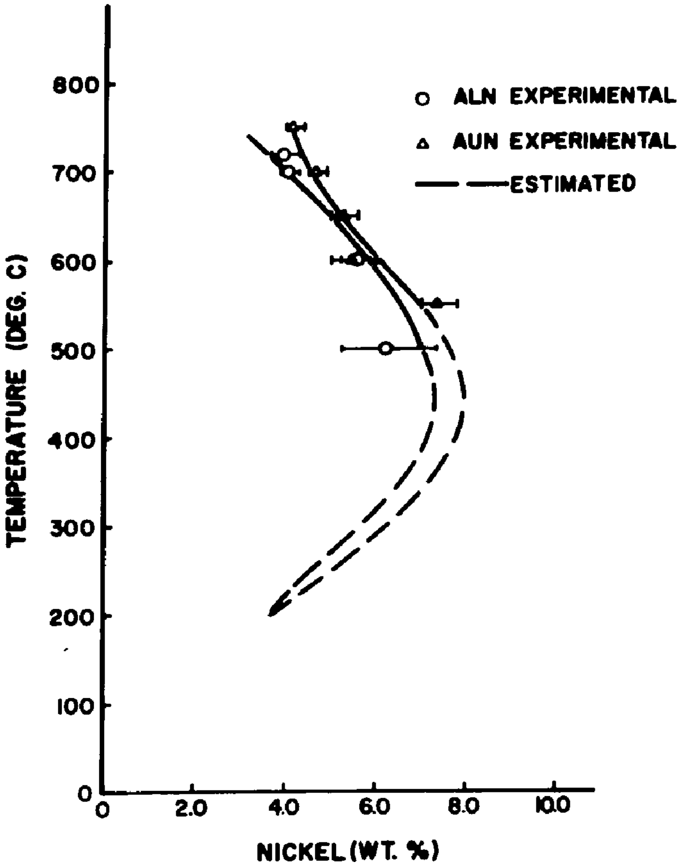

Figure 35. Modified nickel solubility limits for ALN and AUN, α- phase.

These new solubility limits were used in generating a series of cooling rate curves for the meteorites Signal Mountain and Duchesne, two end members of the group IVA. The resultant cooling rate curve shifts are seen in Figures 36a,b. In both cases the cooling rate curve shift is in the same direction, resulting in slower cooling. The cooling rate shift is from 65°C/Myr to 50°C/Myr for the low nickel, low phosphorus meteorite Signal Mountain. There is less than a 1°C/Myr cooling rate shift for the high nickel, high phosphorus meteorite Duchesne. The separation between two simulation based cooling rate curves has diminished. All of the data for the meteorite Signal Mountain including measurement uncertainties lies within the cooling rate range 30 - 80°C/Myr. All of the data for the meteorite Duchesne including measurement uncertainties lies within the cooling rate range 2 - 6°C/Myr.

Changing the nickel solubility limits in the α phase as described effectively reduces the overall cooling rate variation across the group IVA meteorites. It does not produce similar cooling rates for all the group IVA meteorites.

DIFFUSION COEFFICIENTS

The major coefficients of phosphorus, D11M, D11P

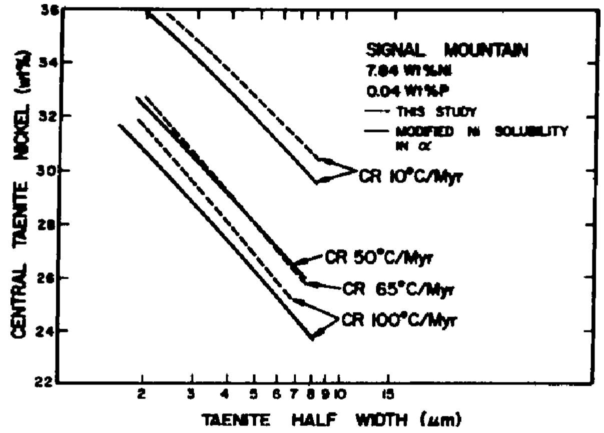

Figure 36. (a) Cooling rate curve shifts due to modified nickel solubilities in the α-phase for the low Ni, low P meteorite Signal Mountain.

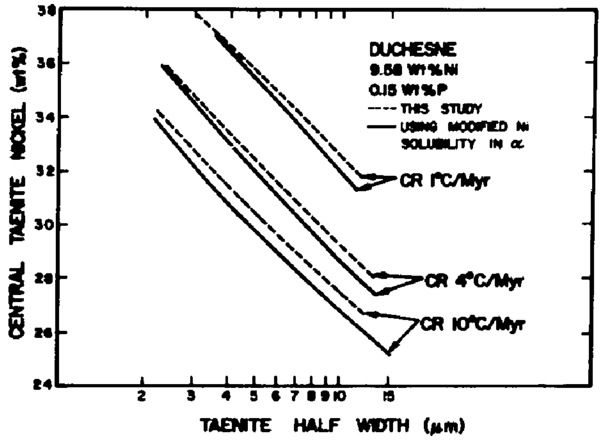

Figure 36. (b) Cooling rate curve shifts due to modified nickel solubilities in the α-phase for the high Ni, high P meteorite Duchesne.

have little effect on the simulation results because the time increment, Δt, is initially set so that the phosphorus concentration profiles are flat in both phases. The major coefficient of nickel in α produces the most serious cooling rate curve shifts. This coefficient, D22P, has been a central issue in most cooling rate studies. Wood[18] assumed $\tilde{D}_\alpha$ to be infinite in his binary simulations. Willis[13] used the values from Hirano et al.[60] for $\tilde{D}_\alpha$, shown in Figure 24, in his binary simulations. Willis and Wasson[55] used the $\tilde{D}_\alpha$ values of Hirano et al.[60] plus a factor that accounted for phosphorus effects in their pseudo binary simulations. Goldstein and Short[17] used the $\tilde{D}_\alpha$ values from Borg and Lai,[35] shown in Figure 24, in their binary simulations.

If the $\tilde{D}_\alpha$ values from Hirano et al.[60] are substituted for those of Borg and Lai[35] in this simulation model, a cooling rate curve shift is observed. The shift results in slower cooling rates at the low nickel, low phosphorus end, and negligibly faster cooling rates at the high nickel, high phosphorus end.

To observe the maximum cooling rate curve shifting that contracts the cooling rate variation across the group the simulations were performed using the modified

Ni solubilities shown in Figure 35 and the $\tilde{D}_\alpha$ values of Hirano et al.[60] Figures 37a,b show the resulting cooling rate curve shifts for Signal Mountain and Duchesne. For Signal Mountain there is a large cooling rate curve shift as well as a decrease in the separation between cooling rate curves. For Duchesne there is very little of a shifting effect, but a slight rotation of the cooling rate curves is indicated. On these new curves all of the data for the meteorite Signal Mountain including measurement uncertainties lies within the cooling rate range 20 - 45°C/Myr. All of the data for the meteorite Duchesne including measurement uncertainties lies within the cooling rate range 3 - 7°C/Myr. Although the cooling rate variation across the group has decreased, there is still a significant and measureable difference in cooling rates between group IVA end members.

SUMMARY WOOD METHOD ANALYSIS

The central issue in this analysis is the determination of the range of absolute cooling rates for a given meteorite and whether there is a significant variation in the absolute cooling rates across the group IVA iron meteorites. The simulation model used in this research produces the greatest variation in

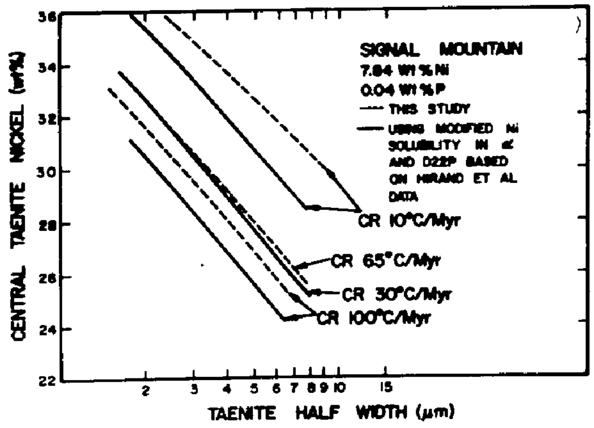

Figure 37. (a) Cooling rate curve shifts due to modified nickel solubilities in the α-phase and increased values of D22P for the low Ni, low P meteorite Signal Mountain.

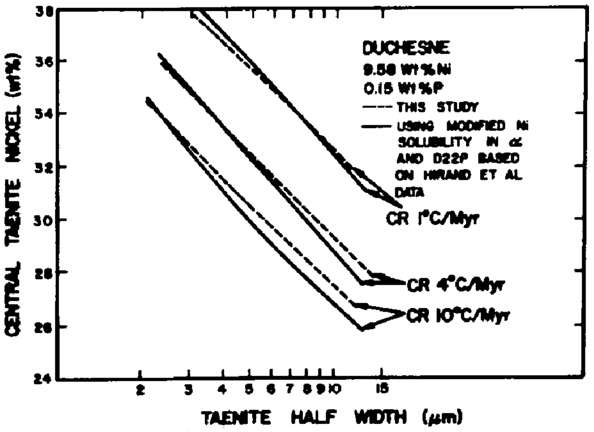

Figure 37. (b) Cooling rate curve shifts due to modified nickel solubilities in the α-phase and increased values of D22P for the high Ni, high P meteorite Duchesne.

cooling rates across the group IVA, and sets a reasonable if not absolute upper bound to the absolute cooling rate of a given meteorite (see Table XVIII). The previously described input variations produce lower absolute cooling rates and less of a cooling rate variation across the group.

The simulation model incorporating the phase diagram and nickel diffusivity in α that results in the least variation in cooling rates across the group IVA also produces a reasonable lower bound on the absolute cooling rates. Table XX lists the cooling rate bounds that enclose all the measured data plus measurement uncertainties for the simulations using the modified Ni solubility in α and Ni diffusion in α. Combining these results with those in Table XVIII produces an extended range of possible absolute cooling rates for a given meteorite. Table XXI lists the entire cooling rate range for each meteorite. The results shown in Table XXI indicate that there is a range of absolute cooling rates for an individual meteorite depending on the choice of input parameters. Under the worst circumstances of applying one model to one end member group and a second model to the other end member group there still exists a significant

TABLE XX

COOLING RATE SPREAD DUE TO INCREASED NICKEL SOLUBILITY LIMITS IN α AND INCREASED D22P VALUES

Spread also reflects data measurement uncertainties

Meteorite	CR Range (°C/Myr)
La Grange	Not Calculated
Signal Mountain	20-45
Gibeon	15-35
Harriman	7-25
Para de Minas	10-20
Muonionalusta	12-35
Charlotte	10-25
Mantos Blancos	2-6
Hill City	3-8
New Westville	2-5
Chinautla	3-10
Duchesne	3-7

TABLE XXI

MAXIMUM SPREAD IN COOLING RATES

Meteorite	Maximum Spread (°C/Myr)	Spread This Study (°C/Myr)
La Grange	50-300	>110
Signal Mountain	20-100	50-100
Gibeon	15-57	26-57
Harriman	7-50	8-50
Para de Minas	10-40	20-40
Muonionalusta	12-40	20-40
Charlotte	10-40	20-40
Mantos Blancos	2-6	3-6
Hill City	3-10	5-10
New Westville	2-5	2-5
Chinautla	3-10	5-10
Duchesne	3-7	3-7

variation in cooling rate across the group IVA iron meteorites. This cooling rate variation across the group is real and cannot be accounted for by uncertainties in the applicable phase diagram and diffusion coefficients. The input variables used in this research are believed to be the best values available from the current research literature. The extreme cooling rate range for a given meteorite shown in Table XXI is too large. The cooling rate ranges determined in this study are given in the last column of Table XXI.

7.2 TAENITE GRADIENT MATCHING

This technique is used to verify the cooling rates determined through the Wood method. In using this technique a determination of the field length is necessary. As described earlier the area under a nickel concentration profile across the γ and α phase is conserved to the original area in the system, BULKN*L. A faster means of producing the same results, i.e. the proper L value, is as follows. On a nickel concentration profile draw in a line at the bulk nickel level. A portion of the nickel profile in γ will lie above this line while the entire nickel profile in α will lie below the line. The surplus area on the γ side above the bulk nickel line must be matched by the depletion region on the α side. An uncertainty in the microprobe data can lead to variations in the L value. When the original attempts were made to produce the corresponding half width for a measured L value by only adjusting the undercooling, ΔT, it was found that several problems existed:

(1) The measured field length was so large it resulted in a half width too large to be matched even with no undercooling.

(2) The taenite half width could be matched but the necessary amount of undercooling produced nickel concentration profiles different than those measured.

The source of these problems lies in the inability to accurately measure the field length, L, due to the uncertainty in the nickel concentration values in α. With an estimated error of ± 0.2 wt% nickel in the α phase there are a wide range of field length values that conserve the orignal mass in the system. As an example the meteorite Signal Mountain will be used. The measured L value was 225 μm with a corresponding half width of ∿ 6 μm (see Table XVII and Figure 33a). A simulation with a CR of 65°C/Myr, $L = 225$ μm, and no undercooling resulted in a taenite half width

> 6.6 μm. Undercooling will only increase the taenite half width. A closer look at the measured Ni concentration profile showed that approximately 23.5 μm from the taenite center the nickel concentration in α became fairly constant at ∿ 7.35 wt%. This means that in the remaining 201.5 μm the nickel deficient area corresponded to (7.84 - 7.35) (201.5) μm wt% or 98.735 μm wt%. If the nickel concentration measurements were only off by 0.2 wt% that same area could be conserved in only 143.1 μm which would yield a field length of ∿ 166.6 μm. With that much latitude in field length values a large number of cooling rates with undercoolings can result in the proper residual taenite half width and taenite nickel concentration profile. The conclusion drawn from Figures 33a-f is that the cooling rates determined using the modified Wood method can, with various undercoolings, produce the measured taenite half widths and taenite nickel concentration profiles when using a field length value within the range of experimental uncertainty. This profile match may not be unique. However, for a fixed cooling rate it is a unique combination of field length, L, and undercooling, ΔT, that produce a matched measured and simulated nickel profile in taenite. The technique will produce correct under-

cooling values.

7.3 IMPLICATIONS OF COOLING RATE VARIATIONS

The 12 meteorites analyzed in this research represent about one-third of the group IVA iron meteorites. This group of 12 meteorites is representative of the entire group IVA since their bulk nickel and phosphorus contents span nearly the entire range for the group IVA.

The group IVA iron meteorites analyzed reveal a variation in cooling rates that is inversely correlated with nickel content. This trend is fairly uniform and has been predicted by other types of cooling rate analyses.[17,37]

Due to this correlation between cooling rate and bulk nickel content it is unlikely that the group IVA iron meteorites had their origins in more than one parent body. Scott and Wasson[26] favor a single parent body due to the discrete clustering of trace element contents that define the meteorites as the group IVA. Willis[13] and Willis and Wasson[55] have also proposed a single parent body for the group IVA iron meteorites with formation in a metallic core. Willis and Wasson[55] performed a cooling rate analysis on 6 group IVA iron meteorites based on a binary system that includes phosphorus effects on the Ni solubility in α and on $\tilde{D}_\alpha$. They conclude that there is no significant variation in cooling rates for the meteorites studied. The input variables used by Willis and Wasson[55] and their modeling technique has been criticized by Moren and Goldstein[66] who have shown that a cooling rate variation does exist across the group IVA iron meteorites.

It would be difficult to produce the observed fractionation patterns (Figures 2-5) and the observed relationship between cooling rate and bulk nickel content if there were several parent bodies for the group IVA iron meteorites. A single parent body is more probable. However, the variation in cooling rates that exists across the group IVA iron meteorites analyzed, greater than a factor of 10, is not consistent with a core origin. A more reasonable hypothesis would be that during the kamacite nucleation and growth period the group IVA iron meteorites were buried at various depths in an asteroidal sized body. Simplistically there could have been gravitational segregation. The more dense material (higher in Ni content) would have been buried at greater depths and would have undergone slower cooling.

In an analysis of the cooling rates and thermal histories of several iron meteorite groups, Fricker et al.[67] developed several parent body models. One of these models consisted of a uniform chondritic body with an initial temperature distribution of 1500°C, just under the bulk melting temperature. The second was a fractionated model in which radioactive heat sources were concentrated toward the surface. The initial temperature distribution was 1500°C. Using either of these two models the variation in cooling rates calculated for the group IVA iron meteorites can be accommodated in a parent body that was ∿ 100-150 km in radius, assuming that the slowest cooling occurred at the parent body center.[67] The distribution of meteorites would be from the center to very near the surface.

7.4 SUMMARY

There is a significant cooling rate variation across the group IVA iron meteorites analyzed in in this research. The cooling rates are inversely correlated with the nickel content. The variation in cooling rates (greater than a factor of 10) argues against a core model for the formation of the

Widmanstatten structure. The uniformity of the relationship between cooling rates and nickel content and the discrete trace element clusterings argues for a single parent body. The meteorites could have been distributed throughout an asteroidal sized parent body 100 - 150 km in radius.

7.5 CONCLUDING REMARKS

In this research it has been determined that a ternary model is a viable approach in simulating phase growth that is diffusion controlled. Planar, spherical or cylindrical geometries can be employed as well as isothermal or non-isothermal processes. A ternary model is essential when third element effects are significant.

The Crank-Nicholson finite difference technique which incorporates a variable grid space transformation allows the simulation to cover the large time periods necessary to produce the Widmanstatten structure. This technique eliminates the use of linear interpolation to shift the grid points or create additional ones. The use of tie line shifting permits the necessary mass balances for both nickel and phosphorus in addition to providing equal interface movement.

The modified Wood method is particularly suited to an analysis of cooling rates for iron meteorites. This method allows one to distinguish between regions on the CR curves where there are undercooling effects and regions where there are no undercooling effects. In addition, undercooling limits can be determined if there is sufficient measured data.

The large but systematic variation of cooling rates across the group IVA meteorites analyzed in this research argues against Widmanstatten formation in a single metallic core. A distribution of iron meteorites throughout a single asteroidal sized parent body is favored.

REFERENCES

1. G. J. H. McCall: Meteorites and Their Origins. David and Charles (Holdings) Limited, Newton Abbot (1973).
2. E. A. Goldberg, A. Uchiyama, and H. Brown: The Distribution of Nickel, Cobalt, Gallium, Palladium, and Gold in Iron Meteorites. Geochim. Cosmochim. Acta 2 (1951) pp. 1-25.
3. J. F. Lovering, W. Nichiporuk, A. Chodos, and H. Brown: The Distribution of Gallium, Germanium, Cobalt, Chromium, and Copper in Iron and Stony-Iron Meteorites in Relation to Nickel Content and Structure. Geochim. Cosmochim. Acta 11 (1957) pp. 263-278.
4. J. T. Wasson: The Chemical Classification of Iron Meteorites: I. A Study of Iron Meteorites with Low Concentrations of Gallium and Germanium. Geochim. Cosmochim. Acta 31 (1967) pp. 161-180.
5. J. T. Wasson and J. Kimberlin: The Chemical Classification of Iron Meteorites II. Irons and Pallasites with Germainium Concentrations between 8 and 100 ppm. Geochim. Cosmochim. Acta 31 (1967) pp. 2065-2093.

6. J. T. Wasson: The Chemical Classification of Iron Meteorites-III. Hexahedrites and Other Irons with Germanium Concentrations Between 80 and 200 ppm. Geochim. Cosmochim. Acta 33 (1969) pp. 859-876.

7. J. T. Wasson: The Chemical Classification of Iron Meteorites IV. Irons with Ge Concentrations Greater than 190 ppm and Other Meteorites Associated with Group I. Icarus 12 (1970) pp. 407-423.

8. J. T. Wasson and R. Schaudy: The Chemical Classification of Iron Meteorites-V. Groups IIIC and IIID and Other Irons with Germanium Concentrations Between 1 and 25 ppm. Icarus 14 (1971) pp. 59-70.

9. R. Schaudy, J. T. Wasson, and V. F. Buchwald: The Chemical Classification of Iron Meteorites.VI. A Reinvestigation of Irons with Ge Concentrations Lower than 1 ppm. Icarus 17 (1972) pp. 174-192.

10. E. R. D. Scott, J. T. Wasson, and V. F. Buchwald: The Chemical Classification of Iron Meteorites-VII. A Reinvestigation of Irons with Ge Concentrations Between 25 and 80 ppm. Geochim. Cosmochim. Acta 37 (1973) pp. 1957-1983.

11. V. F. Buchwald: Handbook of Iron Meteorites. University of California Press, Los Angeles (1975).

12. J. T. Wasson: Meteorites. Springer-Verlag, New York (1974).

13. J. Willis: The Cooling Rates of the Group IVA Iron Meteorites. M.S. Thesis, University of California, Los Angeles (1977).

14. E. R. D. Scott: Chemical Fractionation in Iron Meteorites and its Interpretation. Geochim. Cosmochim. Acta 36 (1972) pp. 1205-1236.

15. W. R. Kelley and J. W. Larimer: Chemical Fractionation in Meteorites-VIII. Iron Meteorites and the Cosmochemical History of the Metal Phase. Geochim. Cosmochim. Acta 41 (1977) pp. 93-111.

16. J. I. Goldstein and R. E. Ogilvie: The Growth of the Widmanstätten Pattern in Metallic Meteorites. Geochim. Cosmochim. Acta 29 (1965) pp. 893-920.

17. J. I. Goldstein and J. M. Short: Cooling Rates of 27 Iron and Stony-Iron Meteorites. Geochim. Cosmochim. Acta 31 (1967) pp. 1001-1023.

18. J. A. Wood: The Cooling Rates and Parent Planets of Several Iron Meteorites. Icarus 3 (1964) pp. 429-459.

19. J. I. Goldstein and A. S. Doan, Jr.: The Effect of Phosphorus on the Formation of the Widmanstätten Pattern in Iron Meteorites. Geochim. Cosmochim.

Acta 36 (1972) pp. 51-69.

20. E. Randich and J. I. Goldstein: Non-Isothermal Finite Diffusion-Controlled Growth in Ternary Systems. Met. Trans. A 6A (1975) pp. 1553-1560.

21. A. S. Doan, Jr. and J. I. Goldstein: The Formation of Phosphides in Iron Meteorites. Meteorite Research (1967) pp. 763-779.

22. S. B. J. Reed: Phosphorus in Meteoritic Nickel-Iron. Meteorite Research. D. Reidel Publ. Co., Dordrecht Holland (1969) pp. 749-762.

23. A. S. Doan, Jr. and J. I. Goldstein: The Ternary Phase Diagram, Fe-Ni-P. Met. Trans. 1 (1970) pp. 1759-1767.

24. T. R. Heyward and J. I. Goldstein: Ternary Diffusion in the α and γ Phases of the Fe-Ni-P System. Met. Trans. 4 (1973) pp. 2335-2342.

25. E. R. D. Scott and J. T. Wasson: Chemical Classification of Iron Meteorites-VIII. Groups IC, IIE, IIIF, and 97 Other Irons. Geochim. Cosmochim. Acta 40 (1976) pp. 103-115.

26. E. R. D. Scott and J. T. Wasson: Classification and Properties of Iron Meteorites. Rev. Geophys. Space Phys. 13 (1975) pp. 527-546.

27. A. Brezina: Die Meteoriteasammlung des k.k. mineralogischen Hofkabinettes in Wien. Jahrb. k.k. Geol. Reichsanstalt. 35 (1885) pp. 151-276.

28. J. I. Goldstein: The Classification of Iron Meteorites. Meteorite Research (1969) pp. 721-737.

29. B. Mason: Meteorites. John Wiley & Sons, Inc. New York (1962).

30. J. I. Goldstein and H. J. Axon: The Widmanstätten Figure in Iron Meteorites. Naturwissenschaften 60 (1973) pp. 313-321.

31. S. O. Agrell, J. V. P. Long and R. E. Ogilvie: Nickel Content of Kamacite Near the Interface with Taenite in Iron Meteorites. Nature 198 (1963) pp. 749-750.

32. T. B. Massalski, F. R. Park and L. F. Vassamillet: Speculations about Plessite. Geochim. Cosmochim. Acta 30 (1966) pp. 649-662.

33. J. A. Wood: Chondrites: Their Metallic Minerals, Thermal Histories, and Parent Bodies. Icarus 6 (1967) pp. 1-49.

34. J. I. Goldstein and R. E. Ogilvie: A Re-evaluation of the Fe-rich Portion of the Fe-Ni System. Trans. Met. Soc. 233 (1965) pp. 2083-2087.

35. R. J. Borg and D. Y. F. Lai: The Diffusion of Gold, Nickel, and Cobalt in Alpha Iron: A Study of the Effect of Ferromagnetism Upon Diffusion. Acta. Met. 11 (1963) pp. 861-866.

36. J. M. Short and J. I. Goldstein: Rapid Methods of Determining Cooling Rates of Iron and Stony Iron Meteorites. Science 156 No. 3771 (1967) pp. 59-61.

37. J. I. Goldstein and J. M. Short: The Iron Meteorites, Their Thermal History and Parent Bodies. Geochim. Cosmochim. Acta 31 (1967) pp. 1733-1770.

38. T. B. Massalski: Researches on Meteorites. John Wiley & Sons, New York (1962).

39. J. M. Short and C. A. Anderson: Electron Microprobe Analysis of the Widmanstätten Structure of Nine Iron Meteorites. J. Geophys. Res. 70 (1965) pp. 3745-3759.

40. S. J. B. Reed: Electron-probe Microanalysis of the Metallic Phases in Iron Meteorites. Geochim. Cosmochim. Acta 29 (1965) pp. 535-549.

41. A. E. Ringwood and L. Kaufman: The Influence of High Pressure on Transformation Equilibria in Iron Meteorites. Geochim. Cosmochim. Acta 26 (1962) pp. 999-1009.

42. W. Jost: Diffusion in Solids, Liquids, Gases. Academic Press N. Y. (1960).

43. J. S. Kirkaldy: Diffusion in Multicomponent Metallic Systems II. Solutions for Two-Phase Systems with Applications to Transformations in Steels. Can. J. Phys. 36 (1958) pp. 907-916.

44. J. S. Kirkaldy: Diffusion in Multicomponent Metallic Systems III. The Motion of Planar Phase Interfaces. Can J. Phys. 36 (1958) pp. 917-925.

45. D. E. Coates: Diffusion-Controlled Precipitate Growth in Ternary Systems I. Met. Trans. 3 (1972) pp. 1203-1212.

46. D. E. Coates: Diffusion Controlled Precipitate Growth in Ternary Systems II, Met. Trans. 4 (1973) pp. 1077-1086.

47. A. E. Moren, E. Randich and J. I. Goldstein: Diffusion Controlled Phase Growth in the Ternary System Fe-Ni-Co. Computer Simulation for Materials Application (Nuclear Metallurgy). eds. R. J. Arsenault, J. R. Beeler, and J. A. Simmons 20 Part 1 (1976) pp. 221-232.

48. S. Widge and J. I. Goldstein: Redetermination of the Fe-rich Portion of the Fe-Ni-Co Phase Diagram. Met. Trans. 8A (1977) pp. 309-315.

49. E. Randich: Non-Isothermal Diffusion Controlled Phase Growth in Ternary Systems and its Application to Iron Meteorites. Ph.D. Dissertation, Department of Metallurgy and Materials Science, Lehigh University (1975).

50. E. Randich and J. I. Goldstein: Cooling Rates of the Hexahedrites. (In press) Geochim. Cosmochim. Acta (1978).

51. H. Fujita and L. J. Gosting: An Exact Solution of the Equations for Free Diffusion in Three-component Systems with Interacting Flows, and its Use in Evaluation of the Diffusion Coefficients. J. Am. Chem. Soc. 78 (1956) pp. 1099-1106.

52. W. D. Murray and F. Landis: Numerical and Machine Solutions of Transient Heat-Conduction Problems Involving Melting or Freezing. Part I - Method of Analysis and Sample Solutions. Trans. ASME 81 (1959) pp. 106-112.

53. R. A. Tanzilli and R. W. Heckel: Numerical Solutions to the Finite, Diffusion-Controlled, Two Phase, Moving Interface Problem (with Planar, Cylindrical, and Spherical Interfaces). Trans. TMS-AIME 242 (1968) pp. 2313-2321.

54. D. U. Von Rosenberg: Methods for the Numerical Solution of Partial Differential Equations. Am. Elsevier Publ. Co., New York (1969).

55. J. Willis and J. T. Wasson: Cooling Rates of Group IVA Iron Meteorites. Submitted to Earth Planet Sci. Let. (July 1977).

56. R. Castaing, P. Deschamps and J. Philibert: X-ray Optics and Microanalysis. Hermann, Paris, France (1966) pp. 594-602.

57. R. S. Clarke, Jr.: Schreibersite Growth and Its Influence on the Metallography of Coarse Structural Iron Meteorites. Ph.D. Dissertation, The George Washington University (1976).

58. P. L. Gruzin and V. V. Minal: Radiometric Study of Phosphorus Diffusion in Iron. FIZ metal. Metalloved. 16 (1963) pp. 551-556.

59. J. I. Goldstein, R. E. Hanneman and R. E. Ogilvie: Diffusion in the Fe-Ni System at 1 Atm and 40 Kbar Pressure. Trans. AIME. 233 (1965) pp. 812-820.

60. K. Hirano, M. Cohen, B. L. Averback: Diffusion of Nickel into Iron. Acta Met. 9 (1961) pp. 440-445.

61. C. B. Moore, C. F. Lewis and D. Nava: Superior Analysis of Iron Meteorites. Meteorite Research (1967) pp. 738-748.

62. L. Fletcher: On the Meteorites which have been found in the Desert of Atacoma and its Neighborhood. Min. Mag. 8 (1889) pp. 223-264.

63. ZAF - 6H, Tracor Northern Inc., Middleton, Wisconsin (1976).

64. J. W. Colby: MAGIC IV - A Computer Program for Quantitative Electron Microprobe Analysis. Unpublished. Bell Telephone Laboratories, Allentown, Pennsylvania.

65. J. I. Goldstein and H. Yakowitz: Practical Scanning Electron Microscopy - Electron and Ion Microprobe Analysis. Plenum Press, New York (1975).

66. A. E. Moren and J. I. Goldstein: Cooling Rate Variations of Group IVA Iron Meteorites. Submitted to Earth Planet. Sci. Lett. (December 1977).

67. P. E. Fricker, J. I. Goldstein and A. L. Summers: Cooling Rates and Thermal Histories of Iron and Stony-iron Meteorites. Geochim. Cosmochim. Acta 34 (1970) pp. 475-491.

APPENDIX I

ALGORITHM FOR BI-TRIDIAGONAL MATRIX[54]

The equations are of the general form

$$a_i^{(1)} u_{i-1} + a_i^{(2)} v_{i-1} + b_i^{(1)} u_i + b_i^{(2)} v_i + c_i^{(1)} u_{i+1} + c_i^{(2)} v_{i+1} = d_i^{(1)}$$

and

$$a_i^{(3)} u_{i-1} + a_i^{(4)} v_{i-1} + b_i^{(3)} u_i + b_i^{(4)} v_i + c_i^{(3)} u_{i+1} + c_i^{(4)} v_{i+1} = d_i^{(2)}$$

$$\text{for } 1 \le i \le R$$

$$\text{with } a_1^{(m)} = c_R^{(m)} = 0 \qquad \text{for } 1 \le m \le 4$$

The algorithm is as follows:

First compute

$$\beta_i^{(1)} = b_i^{(1)} - a_i^{(1)} \lambda_{i-1}^{(1)} - a_i^{(2)} \lambda_{i-1}^{(3)}$$

$$\beta_i^{(2)} = b_i^{(2)} - a_i^{(1)} \lambda_{i-1}^{(2)} - a_i^{(2)} \lambda_{i-1}^{(4)}$$

$$\beta_i^{(3)} = b_i^{(3)} - a_i^{(3)} \lambda_{i-1}^{(1)} - a_i^{(4)} \lambda_{i-1}^{(3)}$$

$$\beta_i^{(4)} = b_i^{(4)} - a_i^{(3)} \lambda_{i-1}^{(2)} - a_i^{(4)} \lambda_{i-1}^{(4)}$$

$$\text{with } \beta_1^{(m)} = b_1^{(m)} \qquad \text{for } 1 \le m \le 4$$

and

$$\delta_i^{(1)} = d_i^{(1)} - a_i^{(1)}\gamma_{i-1}^{(1)} - a_i^{(2)}\gamma_{i-1}^{(2)}$$

$$\delta_i^{(2)} = d_i^{(2)} - a_i^{(3)}\gamma_{i-1}^{(1)} - a_i^{(4)}\gamma_{i-1}^{(2)}$$

with $\delta_1^{(1)} = d_1^{(1)}$ and $\delta_1^{(2)} = d_1^{(2)}$

and $\mu_i = \beta_i^{(1)}\beta_i^{(4)} - \beta_i^{(2)}\beta_i^{(3)}$

The $\beta_i^{(m)}$, $\delta_i^{(m)}$, and μ_i are computed to aid in the computation of the following functions and need not be stored after the computation of

$$\lambda_i^{(1)} = (\beta_i^{(4)}c_i^{(1)} - \beta_i^{(2)}c_i^{(3)})/\mu_i$$

$$\lambda_i^{(2)} = (\beta_i^{(4)}c_i^{(2)} - \beta_i^{(2)}c_i^{(4)})/\mu_i$$

$$\lambda_i^{(3)} = (\beta_i^{(1)}c_i^{(3)} - \beta_i^{(3)}c_i^{(1)})/\mu_i$$

$$\lambda_i^{(4)} = (\beta_i^{(1)}c_i^{(4)} - \beta_i^{(3)}c_i^{(2)})/\mu_i$$

and

$$\gamma_i^{(1)} = (\beta_i^{(4)}\delta_i^{(1)} - \beta_i^{(2)}\delta_i^{(2)})/\mu_i$$

$$\gamma_i^{(2)} = (\beta_i^{(1)}\delta_i^{(2)} - \beta_i^{(3)}\delta_i^{(1)})/\mu_i$$

The values of $\lambda_i^{(m)}$ and $\gamma_i^{(m)}$ must be stored, as they are used in the back solution. This is

$$u_R = \gamma_R^{(1)}$$

$$v_R = \gamma_R^{(2)}$$

and

$$u_i = \gamma_i^{(1)} - \lambda_i^{(1)} u_{i+1} - \lambda_i^{(2)} v_{i+1}$$

$$v_i = \gamma_i^{(2)} - \lambda_i^{(3)} u_{i+1} - \lambda_i^{(4)} v_{i+1}$$

$$\text{for } (R - 1) \geq i \geq 1$$

VITA

Arthur E. Moren is the eldest son of Robert E. and Helen C. Moren. He was awarded a Bachelor of Science Degree in Physics from Wheeling College in May 1968. From June 1968 to May 1971 he served in the U.S. Army. He was awarded the Master of Science Degree in Physics in June 1973 from Lehigh University. Since June 1974, he has pursued the Doctor of Philosophy Degree in Physics at Lehigh University.

Mr. Moren is a member of Alpha Sigma Nu, Sigma Xi, the American Physical Society, and is a joint member of ASM-AIME.